universität wien

MASTERARBEIT / MASTER'S THESIS

Titel der Masterarbeit / Title of the Master's Thesis

„Analysis of black carbon observations during A-LIFE with focus on source regions"

verfasst von / submitted by

Nina Maherndl, BSc

angestrebter akademischer Grad / in partial fulfilment of the requirements for the degree of

Master of Science (MSc)

Wien, 2021 / Vienna, 2021

Studienkennzahl lt. Studienblatt / degree programme code as it appears on the student record sheet:	UA 066 876
Studienrichtung lt. Studienblatt / degree programme as it appears on the student record sheet:	Masterstudium Physik
Betreut von / Supervisor:	Univ. Prof. Dr. Bernadett Weinzierl

Abstract

During the A-LIFE (Absorbing aerosol layers in a changing climate: aging, lifetime and dynamics) project, aircraft measurements were conducted to observe mixtures of absorbing aerosol with the goal of investigating their properties. The most absorbing particle type in the atmosphere is black carbon (BC), which was observed in high mass concentrations in 2017 over the eastern Mediterranean (up to 717 ng/m^3) during A-LIFE using a Single Particle Soot Photometer (SP2). This leads to the question of where the observed BC originated from since BC can be lifted to high altitudes and transported over long distances.

Median vertical profiles of SP2 measured BC mass concentrations show a decrease with increasing altitude from 223 ng/m^3 to 12 ng/m^3 with a slight increase at altitudes above 10 km to 14 ng/m^3. BC coated fractions were observed to be higher over central Europe than over Cyprus, both staying constant with increasing altitudes with only a slight increase at altitudes above 9 km. Over Crete the coated fraction increased rapidly above 9 km and made up close to a quarter at altitudes of 11 km.

In order to gain insight on the geographical source regions of the observed BC, 12-day backward trajectory calculations using FLEXPART were made to simulate BC mass concentrations along the A-LIFE flight routes. The highest mass concentrations stem from the region western Middle East (including Syria, Lebanon, Jordan and Israel) with a mean mass of 71 ng/m^3, whereas local concentration from Crete and Cyprus were low over the respective region (mean: 0.3 and 3.4 ng/m^3). BC of European origin was generally observed in lower altitudes (below 2 km), whereas African/Asian BC had higher mass concentrations and was present at higher altitudes. A shift from European to African/Asian sources with increasing altitude was especially visible over central Europe. At altitudes above 4 km there was a shift from European to African (especially Moroccan, Algerian and Tunisian) BC over Crete as well. On the other hand, over Cyprus a shift from predominately W Middle Eastern to Moroccan, Algerian and Tunisian origin occurred in the same altitude range. Over Crete and Cyprus, locally emitted BC emissions only occurred at altitudes below 2 km in low concentrations. This indicates that BC detected at higher altitudes was transported from further distances. Taking a closer look at mixtures of BC with dust aerosol showed that BC concentrations in polluted Arabian dust layers (mean: 311 ng/m^3) were generally higher than in polluted Saharan (mean: 138 ng/m^3) dust layers. Regarding the dominant source regions, BC in polluted Saharan dust stems mainly from the eastern Egypt including the Nile Delta, Tunisia and Algeria, whereas BC in polluted Arabian dust layers is of dominant W Middle Eastern origin.

Kurzfassung

Während des A-LIFE (Absorbing aerosol layers in a changing climate: aging, lifetime and dynamics) Projekts wurden Flugzeugmessungen zur Beobachtung von Mischungen aus absorbierendem Aerosol durchgeführt, um ihre Eigenschaften zu erforschen. Schwarzer Kohlenstoff (kurz BC vom Englischen "black carbon") bezeichnet die Aerosolpartikel-Subgruppe mit der stärksten Absorption. Im Rahmen von A-LIFE wurden 2017 hohe Konzentrationen von BC (bis zu 717 ng/m^3) über dem östlichen Mittelmeerraum mittels Single Particle Soot Photometer (SP2) gemessen. Das wirft die Frage nach dem Ursprung des detektierten BC auf, da BC in große Höhen und über weite Strecken transportiert werden kann.

Median-Vertikalprofile der mittels SP2 gemessenen BC Massenkonzentrationen zeigen eine Abnahme mit zunehmender Höhe von 223 ng/m^3 zu 12 ng/m^3 mit leichtem Anstieg auf 14 ng/m^3 über 10 km Höhe. Der Anteil an beschichtetem BC war höher über Zentraleuropa als über Zypern, wobei er mit zunehmender Höhe konstant blieb und nur in Höhen über 9 km leicht zunahm. Es konnte festgestellt werden, dass der Anteil an beschichtetem BC über Kreta in einer Höhe über 9 km stark stieg und in 11 km fast ein Viertel ausmachte.

Um die geographischen Ursprungsregionen des gemessenen BC zu bestimmen, wurden mit FLEXPART Trajektorie Berechnungen, die zwölf Tage in der Zeit zurückgehen, BC Massenkonzentrationen entlang den A-LIFE Flugrouten simuliert. Die höchsten Konzentrationen stammten von der Region westlicher Mittlerer Osten (inklusive Syrien, Libanon, Jordanien und Israel) mit einer mittleren Massenkonzentration von 71 ng/m^3, wohingegen lokale Konzentrationen von Kreta bzw. Zypern über der jeweiligen Region niedrig waren (im Mittel: 0,3 ng/m^3 und 3,4 ng/m^3). Europäischer BC wurde in niedrigeren Höhen beobachtet und Afrikanischer / Asiatischer BC in größeren Höhen und in höheren Massenkonzentrationen. Eine Verschiebung von hauptsächlich Europäischen zu Afrikanisch/Asiatischen BC mit zunehmender Höhe war besonders über Zentraleuropa sichtbar. In einer Höhe von über 4 km konnte ebenfalls über Kreta eine Verschiebung von Europäischen zu Afrikanischen BC (hauptsächlich von Marokko, Algerien und Tunesien) festgestellt werden. Über Zypern gab es in der gleichen Höhe eine Verschiebung von Mittlerer Osten zu Afrikanischen BC Ursprung. Hieraus, sowie aus der Beobachtung, dass lokaler BC von Kreta bzw. Zypern nur in Höhen niedriger 2 km in nennbaren Massenkonzentrationen auftrat, lässt sich schließen, dass BC in größeren Höhen weitere Strecken transportiert wurde. Bei näherer Betrachtung von Mischungen von BC und Staubaerosol kann festgestellt werden, dass BC Massenkonzentrationen in verschmutzten Arabischen Staub höher sind (im Mittel: 311 ng/m^3), als in verschmutzen Saharastaub (im Mittel 138 ng/m^3). Bezüglich der dominanten Herkunft Regionen stammt BC in verschmutzen Saharastaubschichten hauptsächlich aus Ost-Ägypten inklusive dem Nildelta sowie Tunesien und Algerien und BC in verschmutzen Arabischen Staubschichten großteils aus dem westlichen Mittleren Osten.

Contents

1. Introduction

Black carbon aerosol (BC) is a key component of the Earth's climate system, heating the atmosphere via direct and indirect radiation effects. BC particles are emitted into the atmosphere mainly through combustion processes, predominately of anthropogenic (e.g. fossil fuel combustion) but also natural sources (e.g. wildfires) (Bond et al. 2013). According to the IPCC, reducing BC could be one of the "easier" ways to slow down global warming as it has much smaller lifetimes in the atmosphere than greenhouse gases such as carbon dioxide. Yet there are still high uncertainties on quantitative estimates of the effect of BC on climate. IPCC estimates of BC radiative forcing, a measure for the amount of warming a component causes in the atmosphere, as well as their uncertainties, are increasing since 1995 (IPCC 2013).

Comparing BC concentrations calculated by climate models to BC measurements shows that BC is overestimated in the higher levels of the troposphere by models (Schwarz et al. 2013). Additional field measurements of BC are needed to improve the accuracy of the climate impact of BC in models. In recent years, aircraft field measurements began to offer a way to measure aerosol particles directly in the atmosphere. This thesis is based on observational data of one such aircraft field experiment: the A-LIFE campaign. A-LIFE stands for *Absorbing aerosol layers in a changing climate: aging, lifetime and dynamics* and was funded by the European Research Council (ERC). The campaign was conducted in 2017 in the eastern Mediterranean region near Cyprus with the DLR Falcon research aircraft. Its overall goal is to investigate properties of absorbing aerosol layers (in particular mineral dust and BC mixtures) (Weinzierl et al. 2020). This work focuses on BC, especially in regards to the geographical source regions of BC observed during A-LIFE. The further sections of this chapter give an introduction to the term 'aerosol', a more detailed explanation of BC, its sources, evolution, transport in the atmosphere and climate impact. At the end of this chapter, the thesis questions and the outline of the following work is given.

1.1. Aerosol

The term *aerosol* describes a suspension of liquid or solid particles in a gas. An aerosol is therefore a two-component system consisting of aerosol particles and a carrier gas (Hinds 2012).

Atmospheric aerosol refers to all aerosols that exist in the Earth's atmosphere. The vast majority of aerosol particles can be separated into four different size modes: the *Nucleation mode* (particles with a diameter smaller than 10 nm), the *Aitken mode* (10 to 100 nm), the *Accumulation mode* (100 to 1000 nm) and the *Coarse mode* (bigger than 1 μm). Besides particle size, aerosols can be further distinguished by other physical properties, such as shape, number concentration per volume, mass concentration per volume or chemical composition. Another way to classify aerosols is by origin. Atmospheric aerosol originates from a vast number of either natural or anthropogenic sources, with natural aerosol making up over 85% of the atmospheric aerosol mass (Hinds 2012)

Atmospheric aerosol plays a key role in the Earth's climate systems, for example via its impact on the radiation budget, both directly and indirectly. Aerosols scatter and absorb solar radiation in the atmosphere leading to a cooling of the atmosphere if light scattering dominates light absorption or a warming if it is the other way around. This is commonly referred to as *direct effect* of aerosol on the global radiation budget. In addition, aerosol particles act as cloud condensation seeds upon which liquid particles form. They therefore affect cloud formation and cause an *indirect effect* on the Earth's climate system (IPCC 2013).

Radiative forcing measures the change in the atmosphere's radiation budget in watts per square meter when a parameter, such as e.g. the concentration of aerosols or atmospheric gases, is changed. A positive radiative forcing means a 'gain' of atmospheric energy and therefore leads to a warming effect. A negative radiative forcing on the other hand, describes a 'loss' of atmospheric energy and a cooling effect follows (Shine 2000). In sum atmospheric aerosol has a negative radiative forcing, but certain aerosol components such as BC have a large positive radiative forcing due to light absorption. It must be mentioned though that there are still high uncertainties in quantitative estimates of aerosol radiative forcing (IPCC 2013). BC and its effects on climate will be talked about in more detail in the coming sections of this chapter due to its critical role in this thesis.

1.2. Black carbon

Black carbon (BC) is a sub-type of aerosol with unique physical properties. It is therefore distinct from other carbon containing atmospheric aerosol as well as other light absorbing aerosol. A variety of different definitions for BC exist. Most commonly the following definition proposed in (Bond et al. 2013) is used:

- BC has is a strong absorber of visible light (mass absorption cross section of at least 5 m^2/g at 550 nm) (Bond & Bergstrom 2006)
- BC is refractory with a vaporization temperature of around 4000 K (Schwarz et al. 2006)
- BC has an aggregate morphology (Medalia & Iieckman 1969)

- BC is insoluble in water as well as most organic solvents (Fung 1990)

In this work the term BC will be used to refer to atmospheric aerosol with the above properties in the context of no specific measurement device and is hence used to describe (FLEXPART) model output. Here the distinction to the term *refractory black carbon (rBC)* must be made. rBC will be used to describe BC measured specifically by a *Single Particle Soot Photometer (SP2)* by laser-induced incandescence. Other measuring instruments use slightly different definitions of BC and therefore will have slightly different results (Petzold et al. 2013).

Other carbon containing aerosol is often summed up under the broad term *Organic Aerosol (OA)*. OA is used to refer to carbon-containing compounds which also contain hydrogen and often oxygen. All BC sources also emit OA particles directly (primary OA), but also emit gases that can undergo gas-to-particle formation in the atmosphere forming secondary OA particles. Another frequently used term is *Organic Carbon (OC)* which refers only to the carbon mass of OA (Bond et al. 2013).

BC and OA are not the only aerosol sub-types that absorb visible light. Dust particles, which mainly originate from deserts and make up a large percentage of natural atmospheric aerosol mass, are also light absorbers, although weaker than BC (Bond et al. 2013).

BC concentrations in the atmosphere are strongly variable depending on location. They range from less than 1 ng/m^3 over very remote regions(Schwarz et al. 2013) to almost 100 $\mu g/m^3$ in highly polluted regions (Singh et al. 2018). BC is mainly found in the Aitken and in the Accumulation mode with its size depending on age as well as source (Schwarz et al. 2008).

1.2.1. Sources and evolution of black carbon

The majority of atmospheric BC aerosol originates from combustion processes, mainly from traffic (road traffic, aviation, shipping, etc.), industry or biomass burning (e.g. wildfires), when there is insufficient oxygen to convert fossil or biogenic fuel into carbon dioxide and water (AMAP 2015). All mentioned sources are located at the Earth' surface, with the exception of air traffic. Only aircraft emissions insert BC directly into the free troposphere. Figure 1.1 shows an overview of different BC sources as well as its impact on the climate system, which is described in detail later in this chapter.

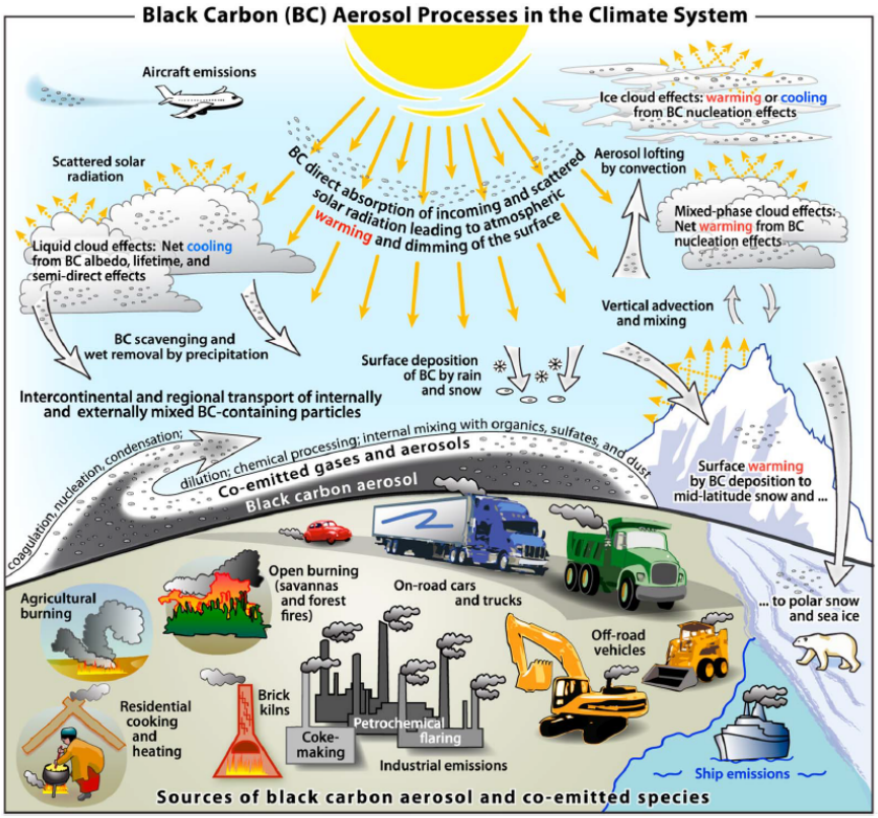

Figure 1.1.: Emission sources of black carbon particles and their role in Earth's climate system (from Bond et al. (2013)).

Emission rates of BC strongly depend on the geographical region. In the northern hemisphere BC originating from on-road and off-road traffic, industrial coal combustion and residential solid fuel burning (biofuel cooking, biofuel heating and coal) dominates, whereas in the southern hemisphere open burning of forests as well as grasses and woodlands have the largest contribution to BC emissions. An estimate of total global BC emission for the year 2000 is 7500 Gg/yr with an uncertainty of range of 2000 to 29 000 Gg/yr. 4800 Gg/yr of this estimate originate from energy-related burning, whereas 2800 Gg/yr are from biomass burning. BC emission rates for different sources are changing quickly as greater energy consumption, especially in east Asian countries, lead to an increase in emissions, but cleaner fuels and technologies decrease emissions (Bond et al. 2013).

North America and western Europe had the highest BC emissions up until the 1950s. Nowadays developing countries in the tropics and east Asian countries are the most dominant BC source regions. Regional hot spots are located in the Indo-Gangetic plains in South Asia, eastern China, most of Southeast Asia, regions of Africa between sub-Sahara and South Africa, Mexico, Central America, Brazil and Peru (Ramanathan & Carmichael 2008).

Figure 1.2 shows BC emission estimates in Gg/yr for the year 2000 by region and source. Especially relevant for this thesis are Middle Eastern emissions, which make up only a small percentage of global emissions and originate mainly from diesel engines but also European emissions, which are mainly from diesel engines and biofuel heating and African emissions, which make up a large part of global emissions and are predominantly from open burning (Bond et al. 2013). It must be noted that from Africa only emissions from Northern Africa are taken into account in the model BC mass calculations in this work, which have much lower emission rates but are closer to the measurement site than sub-Saharan and South African emissions (Ramanathan & Carmichael 2008).

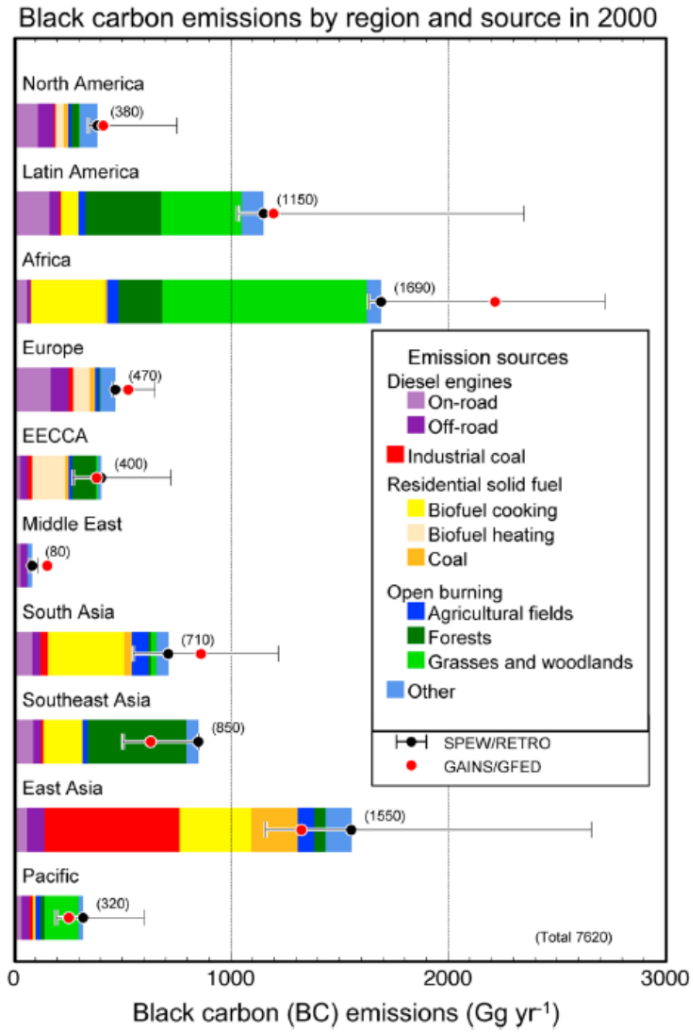

Figure 1.2.: BC emission rates in Gg/yr by region and major source categories in each region for the year 2000 (from Bond et al. (2013)).

BC particles are emitted as small spherical graphitic particles with a diameter of tens of nano meters. They then coagulate to form fractal structures of hundreds of spherical particles within a short time after emission (Adachi et al. 2007). The size of BC particles is dependent on its source as BC particles freshly emitted from fossil fuel combustion range

in size from about 30 nm to 150 nm (Petzold et al. 1999). BC particles originating from biomass burning on the other hand are often larger (Schwarz et al. 2008). The time gone since BC particles have been suspended in the atmosphere also has a large impact on particle size. During aging volatile compounds can condense on the BC particles, giving them a coating. These coatings can change the structure of the aerosol particles from a fractal shape to a more compact one, which makes the particles better cloud condensation or ice nuclei (Zhang et al. 2008). Mahrt et al. (2018) found that BC particles containing pores with diameters of 2-50 nm nucleate ice at cirrus cloud temperature (below 235 K) well. Since the coatings are acquired during aging of BC particles, knowledge of the so called *BC mixing state* can give information on their history.

1.2.2. Transport of black carbon in the atmosphere

The time period, atmospheric aerosol particles stay airborne before they are removed by precipitation (wet deposition) or gravitational settling (dry deposition) is commonly called *lifetime*. Lifetimes of aerosol particles depend on particle size as small particles coagulate and large particles undergo gravitational settling, but also on altitude as stratospheric aerosol has far higher lifetimes than aerosol in the free troposphere (Jaenicke 1980). Within a week, aerosol particles are transported around the world due to fast long-range transport. (e.g. Ramanathan & Feng (2009)) BC has an average atmospheric lifetime of about a week (Bond et al. 2013) and therefore is not only found at its source regions, but also in very remote locations, albeit in low concentrations. Different processes like aging and wet and dry deposition change the distribution of BC aerosol, which affects radiative forcing of the BC aerosol population (AMAP 2015).

Vertical transport of BC can occur via several different meteorological processes such as thunderstorms or low-pressure systems. During biomass combustion, the released heat induces pyro-convection, lifting the emitted BC from the surface into the free troposphere (Peterson et al. 2012). The altitude in which BC is lifted has impact on its atmospheric lifetime as atmospheric BC aerosol is removed quicker in lower altitudes due to precipitation. In remote regions BC mass concentrations therefore typically reach their maximum in the free troposphere, whereas in polluted regions (where BC emission rates are very high) BC mass concentrations generally decrease with increasing height (Bond et al. 2013).

1.2.3. Climate impact of black carbon

BC has the highest light absorption per unit mass of any atmospheric aerosol that occur in significant quantities. It therefore plays a key role in the Earth's energy budget. There are still high uncertainties on estimates of the effect of BC on climate as can be seen in Figure 1.3. One reason for this is the fact that it is difficult to quantify BC emission due to the vast number of different sources (Bond et al. 2013). For example, IPCC estimates of radiative forcing by anthropogenic BC as well as their uncertainties are increasing since

1995 when radiative forcing of anthropogenic BC was estimated to be +0.10 W/m^2 with an uncertainty range of +0.03 to +0.30. In 2007 the respective values are +0.20 [+0.05; +0.35] W/m^2 and in 2013 +0.40 [+0.05; +0.80] W/m^2 (IPCC 2013). According to the fifth assessment report of the IPCC, total BC radiative forcing (anthropogenic and natural) is estimated to be +0.640 W/m^2 with an uncertainty range of +0.250 to +1.09 (IPCC 2013).

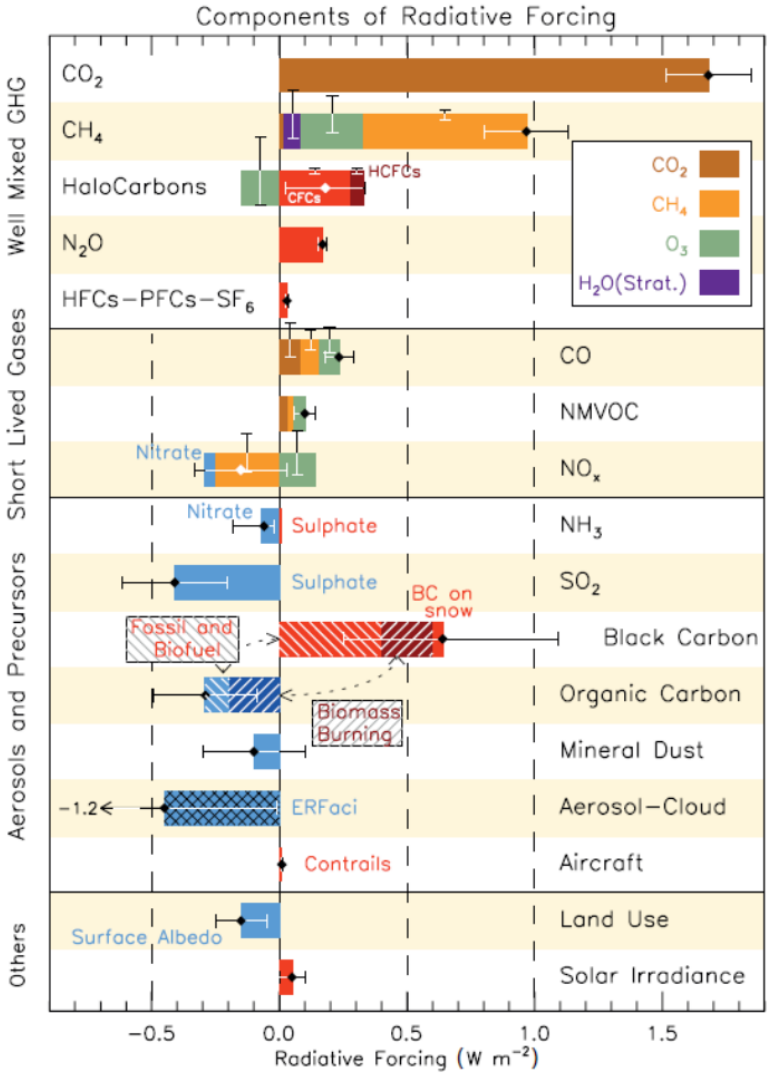

Figure 1.3.: Radiative forcing in W/m^2 for different components of the Earth's atmosphere such as greenhouse gases and aerosols (from IPCC (2013)).

BC affects the climate both directly via light absorption in the atmosphere and indirectly via interactions with clouds. When deposited on a bright surface, it also leads to a reduction in albedo (the ability to reflect light) due to its black color. Lower albedo, meaning less light reflection, generally leads to a warming effect (IPCC 2013). According to a model study by Koch et al. (2011), the reduction in albedo due to BC caused a 20% reduction of snow/ice covering in the Arctic and 20% of warming in the Arctic over the past century. As mentioned in the beginning of this chapter, BC causes a net warming effect on climate, other

than most atmospheric aerosol particles, which have a cooling effect. Metrics commonly used to quantify the relative and absolute contributions of emissions of certain aerosols or gases to climate change are the Global Warming Potential (GWP) and the Global Temperature change Potential (GTP). GWP is the radiative forcing over a chosen time period relative to the same mass of CO_2. A positive GWP means a warming and a negative GWP a cooling effect on climate. Given by the definition, CO_2 has a GWP of 1. GTP gives the ratio of change in global mean surface temperature at a chosen time point caused by the aerosol or gas to that of CO_2. Uncertainties for GWP and GTP for BC are large with a range of 90%. About 65% of the effect BC has on climate is due to interaction with radiation, 20% of which stemming from the albedo effect. GWP and GTP values for a time period of 20 years are(IPCC 2013):

$$\mathrm{GWP}_{BC,\ total} = 3200\ (270\ \text{to}\ 6200) \tag{1.1}$$

$$\mathrm{GWP}_{BC,\ radiation} = 2900 \pm 1500 \tag{1.2}$$

$$\mathrm{GTP}_{BC,\ total} = 920\ (95\ \text{to}\ 2400) \tag{1.3}$$

As a comparison, total GWP for 20 years for OC is -160 (-60 to -320) (IPCC 2013).

1.3. Questions and outline

This work aims to study BC observed during the A-LIFE field experiment with a focus on its source regions using both measurement and model data. Atmospheric BC aerosol is still insufficiently described as was mentioned previously in this chapter. Global atmospheric absorption by BC aerosol is underestimated by models when compared to remote sensing measurements. BC interactions with other aerosol are not described sufficiently and there are still high uncertainties in BC distribution and emission factors from fossil fuel combustion and biomass burning (Bond et al. 2013). In order to better understand aerosol layers containing BC the following questions will be addressed:

1. What is the vertical distribution of rBC mass concentration and coated rBC particle fraction?
2. What are the rBC mass concentrations in polluted Saharan and Arabian dust layers?
3. What are the geographical source regions of rBC measured during A-LIFE?

These questions will be answered based on refractory black carbon (rBC) data measured during A-LIFE by a Single Particle Soot Photometer (SP2) as well as BC mass concentration data modelled by the offline Lagrangian transport and dispersion model FLEXPART.

The next chapter (chapter 2) summarizes the theoretical background of rBC measurements as well as BC transport to understand the results of this thesis. The focus is on microphysical properties of aerosol particles such as size distribution and mixing state and optical properties of aerosol particles (light scattering, absorption, emission and incandescence). Then, chapter 3 gives an overview of the A-LIFE campaign including a description of the inlet of the airplane used during A-LIFE, the DLR Falcon, and the A-LIFE flight sequence classification. Further, a description of the SP2 as well as the data analysis methods used, are given. Results of the measurement as well as the modelled data are shown in chapter 4 and discussed with a focus on BC source region in chapter 5. Lastly, chapter 6 gives a summary of the obtained results and the following main conclusions.

1.4. Use of external data and software routines

The realisation of this study required the collaboration with several persons who provided results achieved outside this work. The A-LIFE rBC data was collected via SP2 before the start of this work and pre-processed SP2 data was provided by Katharina Heimerl (UNIVIE, now at VU Amsterdam). The evaluation of the rBC measurements in terms of vertical distribution as well as flight region and the separation of A-LIFE flights into different flight regions were a major part of this thesis. FLEXPART trajectory calculations were provided by Petra Seibert (UNIVIE, BOKU) and Anne Tipka (UNIVIE). The evaluation of the FLEXPART performance during A-LIFE in terms of BC model data and the definition of BC source regions on the basis of CAMS emission data and FLEXPART trajectory calculations were part of this study. Meteorological data (wind direction, speed) was provided by the DLR.

2. Theoretical background

As was described in the introduction, atmospheric aerosols play a key role in the Earth's climate system. They are a crucial part in many atmospheric processes and change the Earth's radiation budget by scattering and absorbing of solar radiation. Whether aerosol particles have a positive or negative radiative forcing (and therefore lead to a warming or cooling of the surrounding atmosphere) and whether or not they act as effective cloud or ice nuclei depends on different aerosol properties, such as size, shape and chemical composition. It is therefore important to be able to measure different aerosol parameters in order to deduce e.g. their role on climate. Many different measurement principles based on the interaction of aerosol particles with light exist. They are commonly called *optical measurement methods* and are subdivided in *scattering* and *extinction* techniques based on their working principle. The Single Particle Soot Photometer (SP2) is an example for a scattering technique and, playing an important role in this thesis work, is described later in the methods section (chapter 3).

This chapter will focus on the theoretical background needed to understand this thesis work. First microphysical properties of aerosol particles, namely aerosol size distributions and aerosol mixing state will be described. Then the following optical properties of aerosol particles will be discussed: light scattering, light absorption and light emission by aerosol particles as well as incandescence will be explained further. The theory behind microphysical and optical aerosol properties will be explained based on standard works such as Hinds (2012), Seinfeld & Pandis (2006) and Bohren & Huffman (2004). At the end of the chapter long range transport in the atmosphere will be talked about due to its key role in the interpretation of this works results.

2.1. Microphysical properties of aerosol particles

Aerosol particles are usually defined by certain properties such as their particle size (often given by some type of equivalent diameter), total number concentration per volume, mass concentration per volume, particle shape, chemical composition, aerosol mixing state. The size distributions of atmospheric aerosol were already mentioned in the introduction (chapter 1) but will be further explained below. As will the aerosol mixing state due to its importance to the understanding of this work's results.

2.1.1. Aerosol size distributions

The size of atmospheric aerosol particles as well as the particle number and therefore the particle mass concentration play a key role in their optical properties as well as their ability to act as cloud condensation or ice nuclei as e.g. Motos et al. (2019) have shown for the case of BC. Particle size distributions of atmospheric aerosol usually follow a lognormal distribution with a peak and a long tail towards bigger particle diameters. It is not entirely clear, why that is the case, but according to studies (e.g. Brown & Wohletz (1995)) an originally monodisperse distribution can turn into a lognormal distribution due to coagulation and breakup processes. The four modes introduced earlier (Nucleation mode: particles with a diameter smaller than 10 nm; Aitken mode: 10 to 100 nm; Accumulation mode: 100 to 1000 nm; Coarse mode: bigger than 1 μm) can generally all be described by a lognormal distribution leading to a superposition of up to four lognormal distributions for atmospheric polydisperse aerosol populations (in most cases).

For lognormally distributed aerosol particles the so called *count median diameter* CMD describes the median size of the particles, whereas the *geometric standard deviation* GSD stands for the variability of particle size found in the aerosol. Equation 2.1 gives dN, the part of the total number concentration N_0 that falls into the infinitesimal interval $d\ln d$ particles with diameter d.

$$\frac{dN}{d\ln d} = \frac{N_0}{\sqrt{2\pi}\ln GSD} \cdot e^{-\frac{(\ln d - \ln CMD)^2}{(\sqrt{2}\ln GSD)^2}} \tag{2.1}$$

The count median diameter CMD can easily be converted to the surface and the volume or mass median diameter via the Hatch-Choate conversion (Hatch & Choate 1908). Equation 2.2 shows the conversion from count to mass median diameter MMD.

$$MMD = CMD \cdot e^{3(\ln GSD)^2} \tag{2.2}$$

Analogous to the number size distribution given in equation 2.1, the mass size distribution of aerosol particles can be written as follows with M_0 being the total mass concentration.

$$\frac{dM}{d\ln d} = \frac{M_0}{\sqrt{2\pi}\ln GSD} \cdot e^{-\frac{(\ln d - \ln MMD)^2}{(\sqrt{2}\ln GSD)^2}} = \frac{dN}{d\ln d} \cdot \frac{\pi d^3 \rho}{6} \tag{2.3}$$

Here ρ is the density of the aerosol particles.

2.1.2. Aerosol mixing state

There are two (idealised) types of aerosol mixing state: *external* and *internal mixing*. Aerosol populations that consist of two or more different types of aerosol particles, such as dust and soot particles are called externally mixed. Internal mixing, on the other hand, refers to aerosol populations whose individual particles are made up of different compounds. Internal mixing occurs due to coagulation, condensation and coalescence processes as well as chemical reactions on the particle surfaces. Internal mixing can be further subdivided into

internally homogeneously mixed and *internally heterogeneously mixed* particle population with the first referring to particles consisting of soluble and the second to particles consisting of insoluble components. All different (sub-)types of aerosol mixing state are shown in figure 2.1, albeit in an idealised and stylized way.

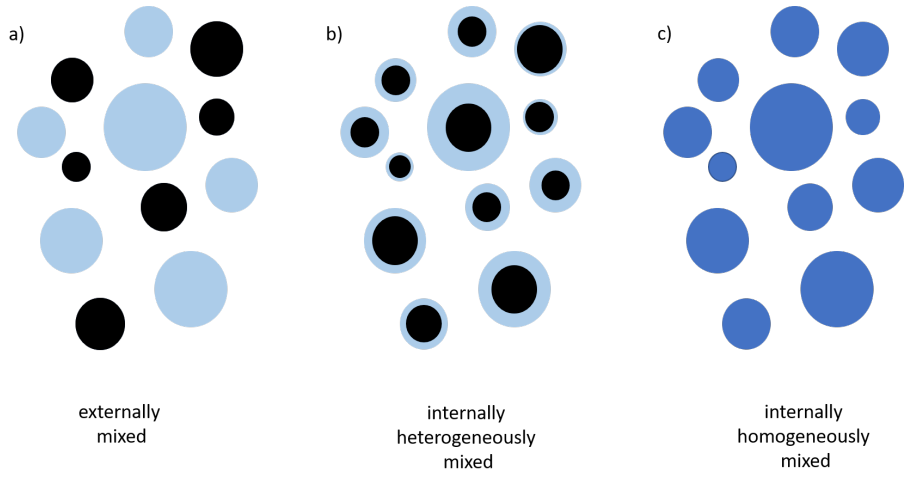

Figure 2.1.: Idealised mixing states of aerosol populations consisting of different chemical compounds: (a) externally mixed aerosol, (b) internally heterogeneously mixed aerosol and (c) internally homogeneously mixed aerosol. Figure adapted from Bond & Bergstrom (2006).

BC aerosol can consist of internally heterogeneously mixed particles with a BC center coated with different materials. The coating thickness influences the ability of particles to activate to cloud droplets. Motos et al. (2019), for example have shown, that BC particles with thick coatings have similar activation behaviour to BC-free particles whereas BC particles without coatings are unable to activate to fog droplets. The internal mixing of BC also affects its radiative forcing by focusing incident solar radiation to the BC core which leads to an increase in absorption (Bond & Bergstrom 2006). In addition, the mixing state of BC influences its atmospheric lifetime by nucleation scavenging as Lund et al. (2017) have shown.

2.2. Optical properties of aerosol particles

Aerosol particles interact with solar radiation in the Earth's atmosphere. The term *Excitation* describes the oscillatory motion that electric charges in a particle are put in, after being hit with a beam of light. These excited electric charges may either re-emit (the same) energy in all direction and therefore *scatter* light, or they may convert part of the energy into e.g. thermal energy and therefore *absorb* light. Both concepts, light scattering and light absorption, are further described in the following section.

Not only do aerosol particles interact with external sources of light, but they also act as a light source themselves. This is due to the fact that all bodies of matter with temperatures above 0 K emit thermal radiation. The physics behind light *emission*, especially *incandescence*, a crucial working mechanism of the SP2, are shortly explained later in this chapter.

2.2.1. Light scattering and light absorption

Optical properties of the way aerosol particles scatter and absorb light depends on particle morphology as well the complex refractive index m.

$$m = n + i \cdot k \tag{2.4}$$

For non-absorbing materials, $k = 0$ and the refractive index m becomes real. m is not only depended on material but also on the wavelength λ of the incident light. In the case of atmospheric aerosol mainly scattering of visible light, which has a wavelength λ between 400 and 700 nm, is of interest, though the general physical principle of light scattering holds for electromagnetic radiation of any wavelength. The scattering depends on the ratio of particle diameter d to the wavelength λ of the incident light. In order to simplify certain equations describing light-scattering the ratio is multiplied by the factor π. The resulting dimensionless parameter is called the *size parameter* x:

$$x = \frac{\pi d}{\lambda} \tag{2.5}$$

There are three different scattering regimes depending on the ratio of particle diameter to wavelength of incident light and therefore the size of x. For $x << 1$, that is particles much smaller than the wavelength λ, the optical regime is called *Rayleigh regime*. If aerosol particles are much larger than the wavelength λ, $x >> 1$ holds and they fall into the so called *geometric regime*. In the so called *Mie regime* particle sizes are of the same magnitude as the wavelength λ. In the Rayleigh as well as the geometric regime scattering equations can be simplified, while this is not the case for the Mie regime. Mie theory provides a complete formal solution of the Maxwell equations, for the scattering of infinite electromagnetic plane waves from homogeneous, spherical particles (Mie 1908).

The so called *scattering cross section* C_{sca} is a measure for the ability of an aerosol particle to scatter light and is a function of wavelength λ, refractive index m and particle diameter d. The *absorption cross section* C_{abs} quantifies its ability to absorb light and also depends on λ, m and d. Both parameters have the dimensions of an area and can be calculated by the ratio of *incident irradiance* I_0 (which is given in $\mathrm{W/m^2}$) and the rate of energy W_{sca} or W_{abs} that is scattered or absorbed by the particle. If light scattered in a certain solid angle is of interest (as is often the case in measuring devices) C_{sca} must be integrated over this solid angle as C_{sca} refers to light scattered in all directions.

$$C_{sca} = \frac{W_{sca}}{I_0} \tag{2.6}$$

$$C_{abs} = \frac{W_{abs}}{I_0} \tag{2.7}$$

The sum of scattering and absorption cross section C_{sca} and C_{abs} is the *extinction cross section* C_{ext}.

$$C_{ext} = C_{sca} + C_{abs} \tag{2.8}$$

The *scattering efficiency* Q_{sca}, the *absorption efficiency* Q_{abs} and the *extinction efficiency* Q_{ext} are dimensionless parameters which can be derived by the ratio of scattering, absorption and extinction cross section C_{sca}, C_{abs} and C_{ext} and the geometric cross section of the particle, respectively. They are measures for the efficiency with which a particle scatters, absorbs or extinguishes light.

$$Q_{sca} = \frac{C_{sca}}{C_{geometric}} \tag{2.9}$$

$$Q_{abs} = \frac{C_{abs}}{C_{geometric}} \tag{2.10}$$

$$Q_{ext} = \frac{C_{ext}}{C_{geometric}} \tag{2.11}$$

As can be easily seen from the equations above, Q_{ext} is the sum of Q_{sca} and Q_{abs}.

$$Q_{ext} = Q_{sca} + Q_{abs} \tag{2.12}$$

It is often of interest to relate scattered to absorbed light due to the different effects of light scattering and light absorption on e.g. the Earth's climate. The ratio of scattering cross section C_{sca} to extinction cross section C_{ext} or scattering efficiency Q_{sca} to extinction efficiency C_{ext} is commonly called *Single Scattering Albedo* SSA.

$$SSA = \frac{C_{sca}}{C_{ext}} = \frac{Q_{sca}}{Q_{ext}} = \frac{Q_{sca}}{Q_{sca} + Q_{abs}} \tag{2.13}$$

Aerosols typically have a heating effect on the surrounding atmosphere if their Single Scattering Albedo SSA is smaller than the surface albedo. If, the other way around, SSA is bigger than surface albedo, they typically contribute to cooling. As was mentioned in the introduction (chapter 1), BC contributes to warming due to its black color that is to say its SSA is almost always smaller than the albedo of the surface below.

Optical instruments using scattering techniques detect light that is scattered by an aerosol particle. The light is provided by a known source (usually a laser) and its wavelength λ is therefore known. As mentioned above, the scattering cross section is defined for light scattering in all directions. In most optical measurement devices only a certain solid angle of light scattering can be detected, since e.g. the direction where the laser sits can't be covered by the detector. The light source in the SP2 is a laser with a wavelength of 1064 nm. The laser beam is reflected by mirrors and therefore comes from both sides. The scattering detector in the SP2 covers a cone at an angle of 15-75° forward and 105-165° backward relative to the direction of the laser beam. (Laborde et al. 2012a)

2.2.2. Emission and incandescence

Aerosol particles, like all bodies of matter with a temperature above 0 K, emit thermal radiation and therefore act as sources of electromagnetic radiation. If particles are in thermal equilibrium with their surroundings, they usually emit the same amount of thermal radiation as they absorb from their surroundings. Black bodies emit thermal radiation with a spectral irradiance B given by Planck's law.

$$B(\lambda, T) = \frac{2\pi hc^2}{\lambda^5} \cdot \frac{1}{e^{hc/k_B \lambda T} - 1} \tag{2.14}$$

The spectral irradiance B is the maximum possible energy that is emitted per solid angle at a certain wavelength λ and therefore depends only on the temperature T of a body of matter. In equation 2.14 h is Planck's constant, c the speed of light in vacuum and k_B refers to Boltzmann's constant. The total emissive power of a black body P (a body that absorbs all incident radiation and re-emits radiation according to Planck's law) can be calculated by integrating equation 2.14 over all wavelengths.

$$P(T) = \sigma T^4 \tag{2.15}$$

Here σ is the Stefan-Boltzmann constant.

True black bodies do not exist in the real world and to calculate the real emission the ideal black body emission must be multiplied by the so called *emissivity* ϵ, which depends on wavelength but also particle size (Moteki & Kondo 2007).

The boiling point of a particle is given by the temperature at which it evaporates and depends on the material it is composed of. BC has a boiling point of around 4000 K and therefore emits visible light when being vaporized according to Planck's law. The emission of radiation at visible wavelengths is commonly referred to as *incandescence*. The measurement principle of the SP2 is based on incandescence of refractory BC and is briefly described later, in the methods chapter (chapter 3). A more detailed theoretical explanation can be found in Laborde et al. (2012b) for example.

Figure 2.2 shows Planck Curves for temperatures between 2000 and 5000 K as well as the bandwidths of the broadband and narrowband detectors of the SP2. The maximum of the curves shifts to smaller wavelengths λ for higher temperatures, commonly referred to as *Wien's displacement law*.

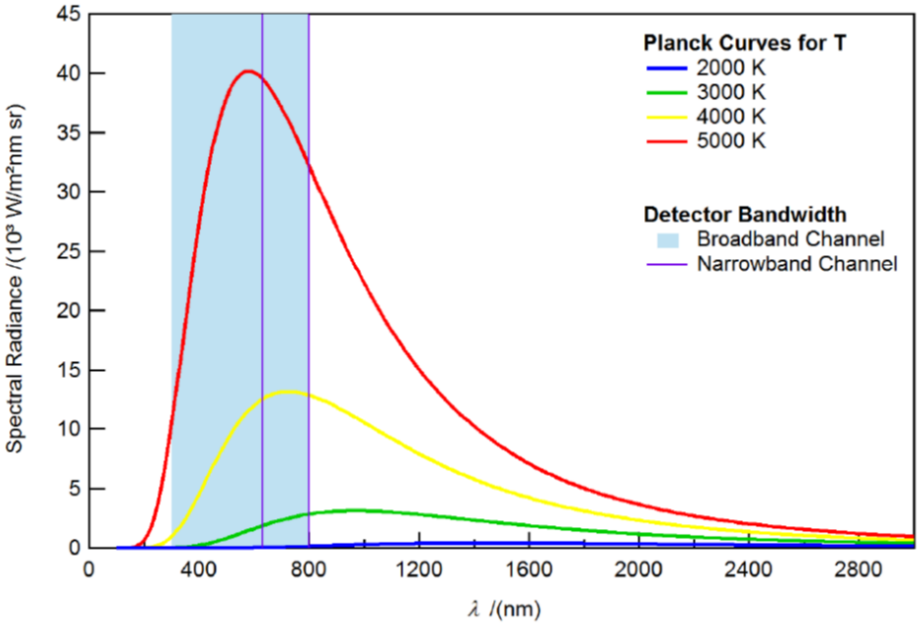

Figure 2.2.: Spectral radiance as a function of wavelength λ for different temperatures including the bandwidth of the broadband incandescence detector (shaded blue area) and the bandwidth of the narrowband detector (vertical violet lines) of the SP2 (from Heimerl (2018)).

2.3. Aerosol transport processes in the atmosphere

All BC sources with the exception of air traffic are located on the surface of the Earth. Most BC observed at altitudes further away from the ground must therefore have been transported there via vertical transport. BC also undergoes horizontal transport and is found in remote locations far away from its source regions. This section deals with vertical and horizontal transport mechanisms to provide a better understanding of this works results. The descriptions here follow works such as Holton (2004) and Roede (2011) where more detailed explanations can be found.

2.3.1. Vertical transport

Whether or not an air parcel is lifted in the atmosphere depends on the so called *atmospheric stability*. It is assumed here that the atmosphere is in hydrostatic equilibrium meaning that the gravity force per unit mass is equal to the pressure gradient force. It is further assumed that air parcels rise/sink adiabatically so that no heat exchange between parcel and surrounding air occurs. This leads to the introduction of the *potential temperature* θ,

the temperature of an air parcel if it would be adiabatically compressed to a pressure p_0 of 1 atmosphere (1013.25 hPa):

$$\theta = T \left(\frac{p_0}{p}\right)^{\gamma} \tag{2.16}$$

Here γ is calculated from the degrees of freedom of air molecules and is 0.286 for air. θ is conserved in adiabatic processes and its gradient $\frac{\partial\theta}{\partial z}$ is a measure of the static stability of the atmosphere. If $\frac{\partial\theta}{\partial z} > 0$, the atmosphere is statically stable and the air parcel is less buoyant than the surrounding air when being displaced adiabatically. This means that vertical motion does not occur on its own. If $\frac{\partial\theta}{\partial z} < 0$, the atmosphere is statically instable and the air parcel rises/sinks further when it is adiabatically displaced. Statically neutral means $\frac{\partial\theta}{\partial z} = 0$. If conditions are statically stable, vertical motion can still occur via other processes such as dynamic instabilities, vertical wind shear or air being forced to rise due to mountains etc.

Instability of the atmosphere often occurs due to radiative heating of the ground. This leads to a warming of the lowest layer of air and further to vertical motion air masses. As long as the temperature of an air parcel is higher than the temperature of the surrounding air, it rises adiabatically. This process is called *convection*. A special form of convection is *pyro-convection* where vertical transport is induced through heat released by e.g. biomass burning.

When the temperature of a rising air parcel reaches the dew point, water starts to condense and clouds start to form. This releases latent heat which further supports the ascent of the air parcel. Depending on atmospheric conditions, the ascent stops at altitudes in the lower troposphere resulting in cumulus or stratocumulus clouds or reaches heights up to the tropopause, or even overshooting into the stratosphere resulting in thunderstorms (cumulonimbus with overshooting tops). BC released through biomass burning can be transported to high altitudes via thunderstorms, as for example Huntrieser et al. (2016) have shown. Another type of vertical motion is found in warm conveyor belts (Eckhardt et al. 2004), where BC can be lifted efficiently as e.g. is described in Park et al. (2005).

Vertical mixing of air masses takes minutes to hours in the boundary layer (lowest part of the atmosphere that is directly influenced by contact with the Earth's surface), days to weeks in the free troposphere and about one to two years for troposphere-stratosphere mixing.

2.3.2. Horizontal transport

Figure 2.3 show a sketch of the global scale atmospheric circulation systems. This represents the average conditions, which will be talked about in this section.

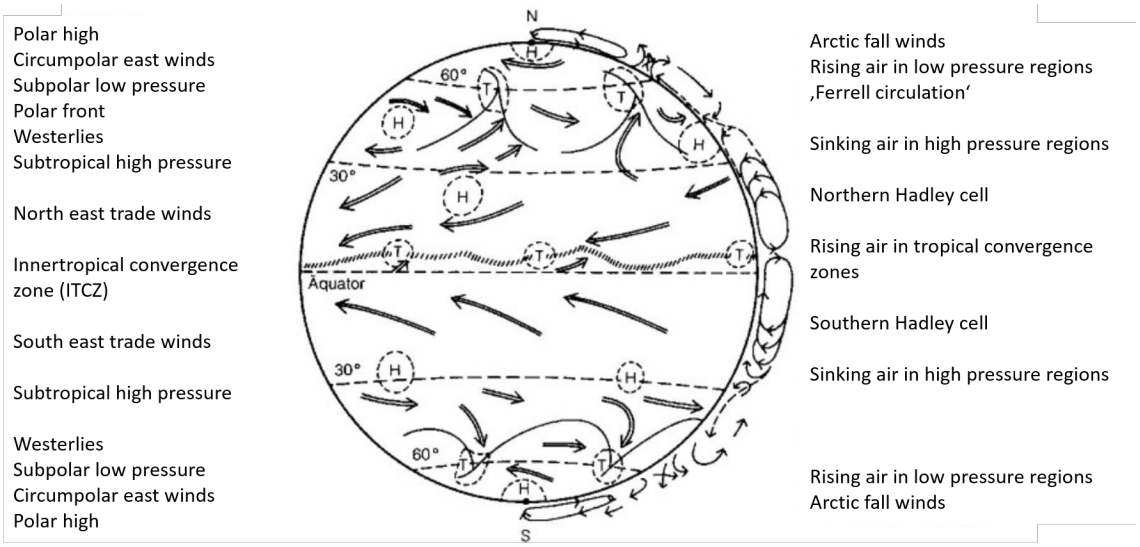

Figure 2.3.: Schematic overview of global circulation systems. On the left side, the most important surface winds are listed; on the right side, meridional circulation patterns can be seen. See text for further explanations (adapted from Roede (2011)).

In latitudes up to about 30 to 35 degrees north and south of the equator the trade winds make up the dominant wind system. They are north-easterly / south-easterly winds in the northern / southern hemisphere and originate from humid air masses that rise at the region of highest solar radiation. Near the surface the air masses flowing towards the equator are directed towards the West due to the Coriolis force. This zone is called *inner tropical convergence zone* (ITCZ). The surface air pressure inside the ITCZ is low and rises with an increase in latitude. The rising air masses at the equator are driven pole-wards at high altitudes and sink back towards the surface in the subtropics creating the so called *Hadley-circulation*.

Further away from the equator in latitudes 30 to 35 degree north / south there's a region of doldrums and high surface pressure. Then, in 35 to about 70 degrees latitude, western winds, the so called *westerlies*, dominate. The westerlies are much less stable and uniform than the trade winds and are influenced by fronts, cyclones (low pressure systems) and anti-cyclones (high-pressure systems). Driven by the temperature gradient between the equator and the poles, the westerlies can be described as thermal winds, although the resulting circulation patterns can only be explained by the varying pressure systems. In the mid-latitudes there is no equivalent to the Hadley circulation. Looking at the average air circulation, air travels pole-wards at low altitudes, where it rises and drifts back towards the sub tropes at high altitudes. This is often referred to as the *Ferrel-circulation*.

Near the poles, at the polar front where cold air and warm air masses meet, the surface air pressure is low and rises towards the poles. Easterly winds circle the poles, offshoots of the westerlies can sometimes reach up to these high latitudes, though.

Aerosol particles, once they are emitted into the air, get carried around the world by these circulation systems. It takes a few days to weeks for air masses to mix along the circles of latitude, and one to two months along the circles of longitude. It must be noted though that as soon as these circulation systems include precipitation removal of aerosols via wet deposition occurs.

3. Methods

At the beginning of this chapter an overview of the A-LIFE campaign is given including an introduction to the classification of the flights into 'flight sequences'. Then the Single Particle Soot Photometer (SP2), which was used during A-LIFE to measure refractory Black Carbon (rBC) will be described. In the 'Data Analysis' section of this chapter the processing of SP2 rBC data will be explained briefly, as will the FLEXPART backward trajectory calculations whose input are CAMS emission data. At the end, the separation of A-LIFE flights into four distinct geographical regions for further analysis, will be introduced.

3.1. A-LIFE campaign overview

As mentioned in the introduction, A-LIFE stands for 'Absorbing aerosol layers in a changing climate: aging, lifetime and dynamics'. The A-LIFE project was funded by European Research Council (ERC) under the European Union's Horizon 2020 research and innovation program, started in October 2015 and has a project duration of six years. The overall aim is to investigate the properties of absorbing aerosol with a focus on mixtures of mineral dust and black carbon. In particular, A-LIFE aims to characterize aging and mixing of absorbing aerosol layers during their lifetimes, assess the contribution of single aerosol components (especially BC and mineral dust) to radiative forcing, implement complex particle morphologies in estimates of radiative forcing and investigate potential links between aerosol layer composition, lifetime and particle removal (A-LIFE webpage 2017).

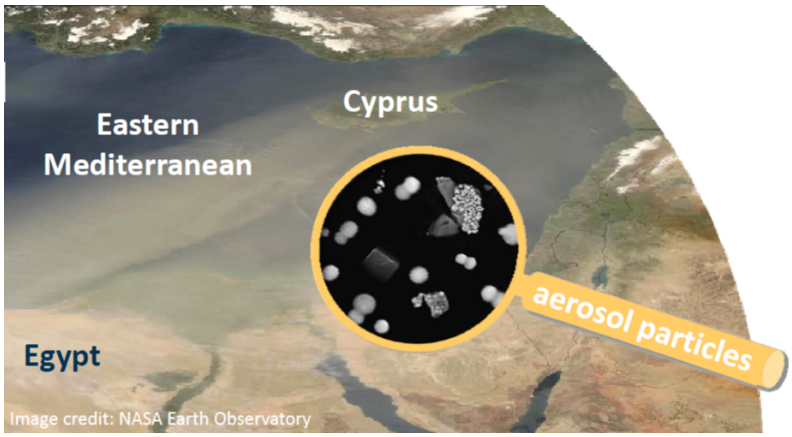

Figure 3.1.: Map of the Eastern Mediterranean including Cyprus and a stylistic close up of aerosol in dust layers (figure by Bernadett Weinzierl (UNIVIE) (A-LIFE webpage 2017), satellite image from NASA Earth Observatory).

To achieve these goals a large amount of data was collected during an aircraft field campaign which took place in Cyprus between 3rd and 30th of April 2017. A total of 22 flights (including two test and four transit flights) were conducted with the DLR research aircraft Falcon 20-E5 (D-CMET) measuring the entire atmospheric column from the ground up to 12-13 km altitude. A list of all flights including date, take-off and landing time and airport and a short description of each objective is given in the appendix in B.1 (A-LIFE webpage 2017) (Weinzierl et al. 2020).

During this measurement campaign, aerosol and meteorological data was collected with in-situ and remote sensing instruments integrated on the DLR Falcon as well as ground-based in-situ and remote sensing instruments. Measurement devices were both mounted under the wings of the DLR Falcon as well as inside the aircraft cabin behind an isokinetic inlet (diameters Dp < 2.5 μm). They include condensation particle counters with different cut-off diameters, optical particle counters, a nephelometer, absorption photometer, a cloud condensation counter, a single particle soot photometer, impactors as well as cloud and aerosol spectrometer. This allowed for example the means to gather information on size distribution of the observed aerosol and determine its optical properties (scattering and absorption coefficient as well as refractive index). In general aerosol ranging from 4 nm to 930 μm was measured. Of particular interest to this thesis is the Single Particle Soot Photometer (SP2), which is described in greater detail later in this chapter. With the SP2 rBC mass and mixing state were measured. The ground-based instruments, such as sun photometers, lidar and a trace gas monitor were located at the Paphos airport site (were the DLR Falcon was based at) and Limassol. (A-LIFE webpage 2017) (Weinzierl et al. 2020)

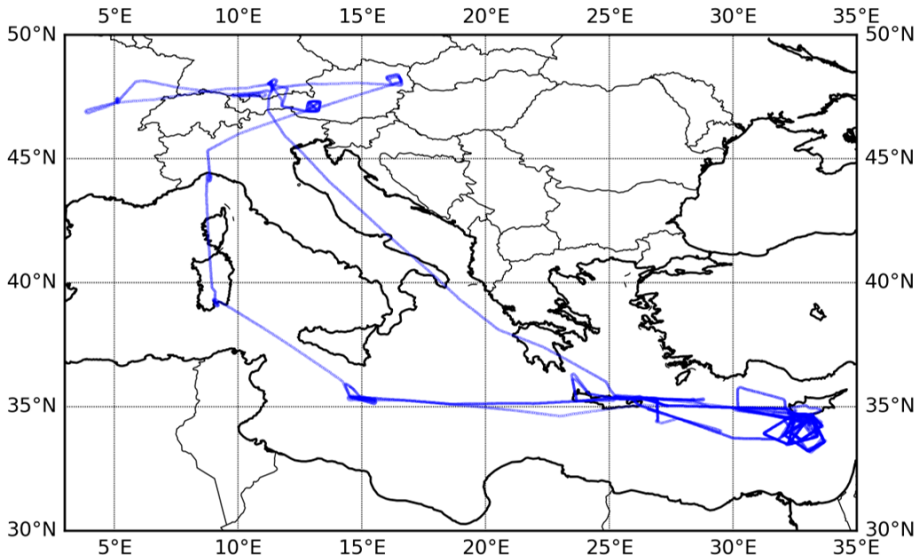

Figure 3.2.: Map of all A-LIFE flight paths (figure provided by Josef Gasteiger (UNVIE).

3.1.1. Flight sequences

A variety of different aerosol types from different source regions were measured during each mission flight. In order to determine parameters for certain aerosol types, averaging periods, called *sequences* were defined. The data gathered during each flight was therefore separated into time periods where the Falcon flew at constant altitude outside of clouds. Each sequence was classified according to the aerosol classification scheme described below. In total 262 A-LIFE sequences were defined (Weinzierl et al. 2020).

There are in total 12 different aerosol sub-classes plus a *Mediterranean background* class. In general, sequences are divided into *mineral dust* and *other aerosol* when enhanced aerosol concentrations were measured. Sequences are classified as mineral dust if there are high number concentrations of particles with diameters D_p larger than 800 nm $N_{Dp>800\ \mathrm{nm}}$ and more than 30% of the aerosol mass is dust according to FLEXPART calculations. Further mineral dust is separated into *Saharan* and *Arabian dust* according to the FLEXPART predominant origin. Sequences that do not fall into the category mineral dust are distinguished by their coarse mode number concentration $N_{Dp>800\ \mathrm{nm}}$ into *Mixtures with enhanced coarse mode number concentrations* and *Mixtures with low coarse mode contribution*. Further, there is a pollution criterion based on the ratio of the coarse mode number concentration $N_{Dp>800\ \mathrm{nm}}$ to the rBC mass concentration M_{rBC}. Sequences are classified as *clean* if M_{rBC} is low compared to $N_{Dp>800\ \mathrm{nm}}$. If M_{rBC} is very high compared to $N_{Dp>800\ \mathrm{nm}}$, the sequence is classified as *polluted*. In between, sequences are classified as *moderately polluted*. Whether or not a sequence falls into the Mediterranean background category is decided by the Extinction coefficient σ_{ext}. A detailed description of the classification scheme including quantitative limits of the different parameters for the different classes and explanations why the limits were chosen can be found in Weinzierl et. al. (2021, in prep.).

In this thesis BC source regions according to FLEXPART are determined for all 12 aerosol sequence classes with a special focus on mineral dust sequences.

3.2. Measurement of rBC with the SP2

During A-LIFE refractory black carbon (rBC) was measured by a Single Particle Soot Photometer (SP2). The SP2 was installed inside the DLR Falcon aircraft cabin and connected to an isokinetic inlet. As mentioned in chapter 1 BC is used to refer to light-absorbing carbonaceous substances in atmospheric aerosol in the context of no specific measurement method whereas rBC describes BC measured specifically by the SP2 (Petzold et al. 2013). The SP2 can only observe rBC, as the measuring instrument works by laser-induced incandescence and therefore is only able to measure the part of black carbon that strongly absorbs light and has a boiling point temperature around 4000 K (Schwarz et al. 2006).

3.2.1. Description

The SP2 is a commercially available instrument produced by 'Droplet Measurement Technologies'. It operates as followed: aerosol particles are aerodynamically carried into to the centre of a Gaussian shaped laser beam, which has about four times the width of the aerosol particle beam. Particles containing BC are heated up by the laser due to light absorption. During this process they lose their non-refractory coatings. Once the BC core reaches vaporization temperature it incandesces. The peak intensity of the thermal emission is measured by the SP2 which is used indirectly to quantify rBC mass. In addition, light that is elastically scattered by the aerosol particles is detected by an avalanche photo diode (APD). From this measurement the optical particle size of non or weakly absorbing aerosol particles can be determined. In combination with the rBC mass as well as information on the position of the particle in the laser beam (measured by a two-element APD) the mixing state of rBC can be quantified (Laborde et al. 2012a).

Figure 3.3 shows the open SP2 instrument giving a view on its components. It contains two Photomultiplier tubes (PMTs) with different optical filters and two light scattering detectors. Thermal radiation emitted by incandescence of the aerosol particles is detected by the PMTs, whereas the light scattering detectors are used for optical particle sizing. The four detectors are located in the measurement chamber which is mounted moveable in the middle of a black optical block. The black optical block also contains a laser crystal (Nd:YAG) and mirrors. The sampled air is sucked into the measurement chamber through the inlet at the top.

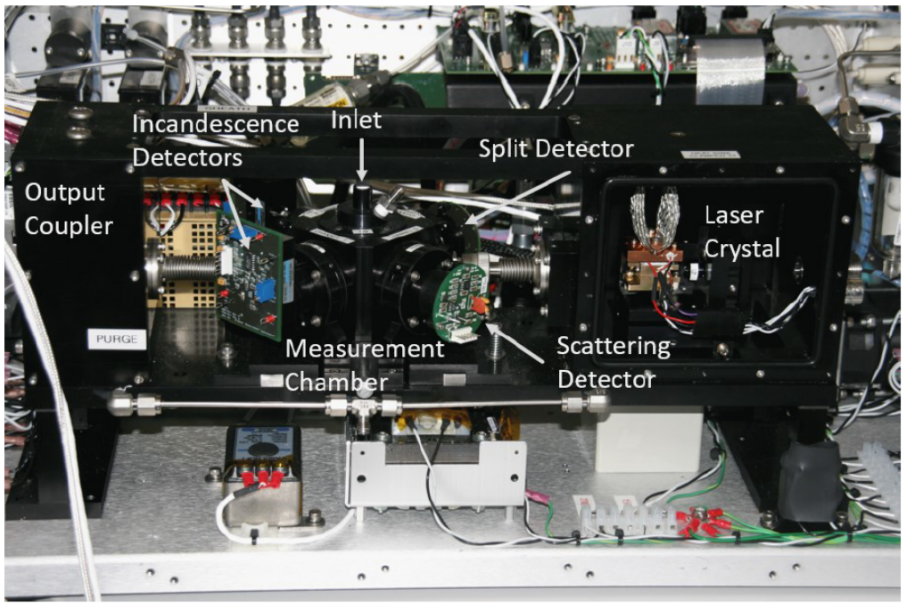

Figure 3.3.: Image of the SP2 with open housing showcasing its components. The optical block can be seen in the front containing the measurement chamber in its middle and the YAG laser crystal in the right (from Heimerl (2018)).

3.3. Data analysis

In this thesis both observational rBC data and modelled BC data were used to answer the questions stated in the beginning. A summary of the different data is included in the appendix in B.2. In the following sections, an overview of the data analysis methods is given. First, a brief explanation of the SP2 rBC data processing is given, as pre-processed data was kindly provided by Katharina Heimerl. Then, the offline Lagrangian transport and dispersion model FLEXPART as well as the separation into different BC source regions will be described. At the end of the chapter, the separation of A-LIFE flight paths into four flight regions for latitude/longitude depended analysis will be depicted.

3.3.1. rBC data

This work uses pre-processed rBC data obtained during A-LIFE by the SP2. This chapter focuses on SP2 detector signals and the quantities, such as rBC mass concentration and coated fraction that can be derived from them.

As was already mentioned previously in this chapter (section 3.2.1) there are four optical detectors used to measure aerosol particles by the SP2. Table 3.1 describes the four detectors in detail. The response curve for each aerosol particle is recorded with 150 points per particle with a temporal resolution 0.4 μs switching between high and low gain for the incandescence detectors.

Table 3.1.: List of SP2 detectors and measured quantity adapted from Dahlkötter (2013). For A-LIFE the rBC mass was in the range 5 - 104 fg corresponding to an equivalent size range of 70 - 990 nm.

SP2 detector	**measured parameter**
PMT 1: broadband incandescence detector (BID)	mass of rBC core
PMT 2: narrowband incandescence detector (NID)	mass of rBC core
ADP 1 :light scattering detector (LSD)	optical size of rBC-free particles
ADP 2: position sensitive detector (PSD)	position of the particle in the laser beam

Optical filters (Schott KG5 filter and Schott KG5 plus RG630 filter) restrict the two PMTs to light between 300 and 800 nm and 630 to 800 nm, respectively. The PMTs are therefore referred to as broadband incandescence detector (BID) and narrowband incandescence detector (NID), based on the wavelength spectrum width they cover. Using detectors with two different wavelength spectra allows determining the color ratio (equation 3.1), which indicates the vaporisation temperature of the particles according to the black body theory

(described in chapter 2.2.2).

$$color\ ratio\ = \frac{signal\ of\ BID}{signal\ of\ NID} \tag{3.1}$$

The signal of the NID is amplified by hardware due to less incoming radiation. Figure 3.4 shows an example response signal for all four detectors to a coated rBC particle traversing the laser beam. The particle is heated up by absorbing laser light until it reaches vaporization temperature. During this process it emits thermal radiation reaching the peak intensity usually at vaporization temperature. The peak height is proportional to the mass of rBC components of the particle. When the particle begins to evaporate the signal decreases due to the shrinking particle size until no rBC is left. The rBC mass can then be calculated by applying the signal-to-mass relationship which is derived by calibration of the instrument. From the particle mass the mass equivalent diameter (meaning the diameter of a spherical particle of the same mass and material) D_{rBC} can be calculated assuming a void-free rBC material with a density of $\rho = 1800$ kg/m^3.

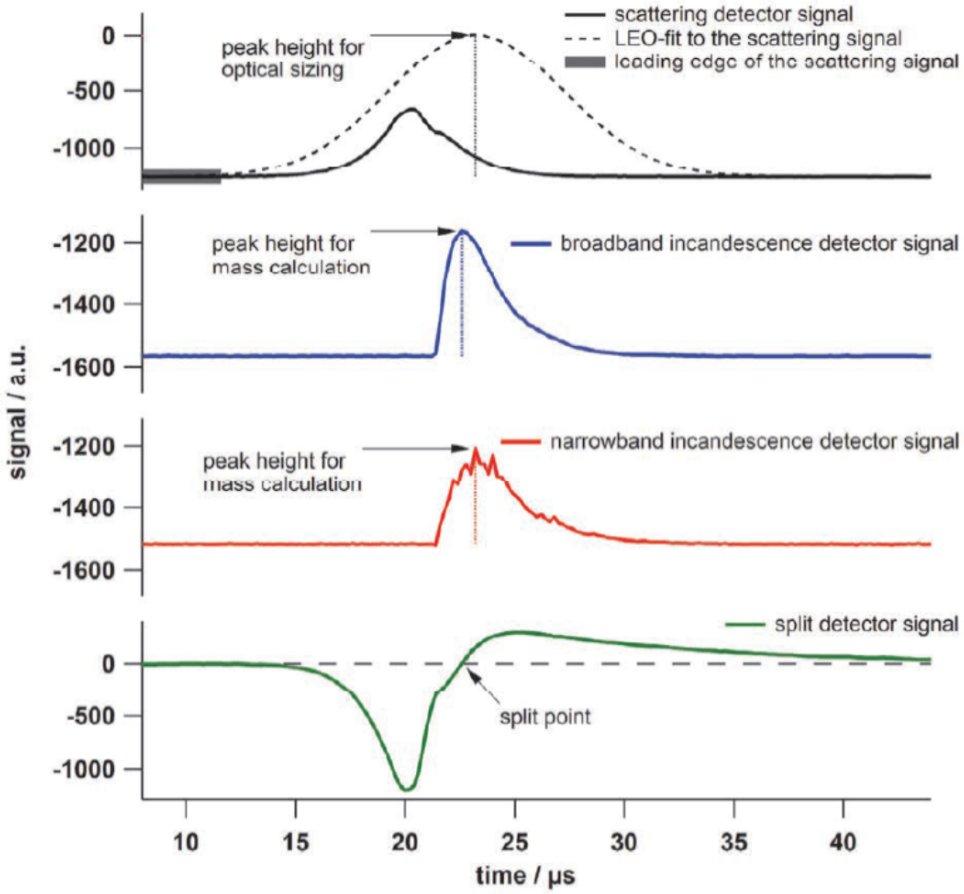

Figure 3.4.: Response signals of all four detectors of the SP2 for a coated rBC particle traversing the laser beam. See text for explanations. (Figure from Dahlkötter (2013) adapted from Heimerl (2011)).

A light scattering detector (LSD) is used in the SP2 for optical particle sizing. Particles that are non-absorbing and therefore do not contain rBC pass the laser-beam unaltered. They produce a Gaussian shaped signal. The signal peak is proportional to the scattering cross-section of the particle and only depends on the particle size and its refractive index. The LSD signal of particles that contain rBC is not proportional to the scattering cross-section of the (undisturbed) particles due to evaporation of the particles when passing through the laser. However, a second light scattering detector (PSD) makes it possible to determine the scattering cross-section of rBC containing particles as well by determining the position of the particles in the laser-beam at any time assuming constant particle velocity during the traverse of the laser. The point where the PSD signal crosses the zero line is called 'split point' and can be seen in figure 3.4. The scattering-cross section of the undisturbed particles is determined prior to evaporation by the LSD signal in the leading edge of the laser beam. This method is commonly referred to as 'leading-edge-only' fit, LEO-fit for short and was introduced by Gao et al. (2007). The LEO-fit method takes advantage of the Gaussian shape of the laser beam to fit a Gaussian function to the leading edge of the LSD signal. A Gaussian function is fully described by four parameters: the position of the peak, its height and width as well as the baseline. Therefore the peak height, which is proportional to the scattering cross-section of the undisturbed particle, can be determined if the other three parameters as well as at least one point of the function are known. The position of the peak is given by the PSD and the width depends on the laser beam as well as the speed of the particles. When measuring an aerosol population with both evaporating and non-evaporating particles at constant pressure within a short time period a constant peak width can be assumed. The baseline can be determined by the signal of the particles outside the laser beam (before and after traverse). The peak height that is either directly derived from the signal for non-absorbing particles, or calculated by LEO-fit for absorbing particles, is then converted by a look-up table which was calculated with the Bohren-Huffman Mie code (Bohren & Huffman 2004). For non-absorbing particles homogeneous spheres are assumed, whereas absorbing particles are treated as coated spheres.

The LEO-fit can be used to derive the coating thickness of individual rBC-containing particles by calculating the difference between the total radius of the particle (derived by LEO-fit) and the radius of the rBC core. Coating thickness values have an error range of 20 to 50 nm, with the upper limit resulting from to the assumption of spherical shapes as well as the assumed refractive index.

In order to attain good performance and reproducibility of measurements with the SP2, calibration and alignment procedures are needed. This can, for example, be seen in a study conducted by Laborde et al. (2012a), where six SP2s from different institutions were compared. Since for this work, pre-processed SP2 data was provided and the instrument setup and calibration were done prior, the alignment and calibration procedures will only be described briefly. More detailed descriptions can be found in Heimerl (2018) and Dahlkötter (2013).

The recommended SP2 adjustments (following Schwarz et al. (2010)) are: Aligning the laser to a TEM_{00} mode (Gaussian laser profile), aligning the mode aperture as well as aligning the detector block horizontally so that laser beam and aerosol jet are in optimal position. The LSD (Scattering detector) also needs to be aligned as does the two-element APD detector so that both show high and stable amplitudes with minimal noise. In order to ensure that the color ratio is independent from the laser intensity, the laser power must be adjusted. The color ratio is here used only as an indicator if the laser intensity is sufficient to heat the particle to complete evaporation, though. The SP2's internal flow measurement device must be calibrated for reliable calculation of measured concentrations. The relationship between particle mass and the incandescence detector signal is determined by calibration with a size-selected refractory black carbon material standard. For the calibration of the SP2 operated during A-LIFE, fullerene soot was used assuming an error of 10% in the calibration material mass. Taking other error sources (systematic error of the mobilization technique used to size-select the fullerene soot, detector noise, etc.) into account the maximum error range of the rBC mass concentration is between 20% and 30%. These are maximum ranges, though, with Laborde et al. (2012a) showing that the maximum deviation of the 6 SP2s that were compared was 15%, which was partly due to a misalignment of the laser of one instrument. Equations 3.2, 3.3, and 3.4 show the final A-LIFE calibration, where BBHG stands for broadband high gain, BBLG for broadband low gain and NBLG for narrowband low gain (the incandescence detector signals).

$$\mathrm{BBHG}_{mass} = 0.16 + 0.000172 \cdot \mathrm{BBHG}_{PeakHeight} \tag{3.2}$$

$$\mathrm{BBLG}_{mass} = 0.2 + 0.00160 \cdot \mathrm{BBLG}_{PeakHeight} + 7 \cdot 10^{-9} \cdot \mathrm{BBLG}^2_{PeakHeight} \tag{3.3}$$

$$\mathrm{NBLG}_{mass} = 0.23 + 0.0149 \cdot \mathrm{NBLG}_{PeakHeight} \tag{3.4}$$

The SP2 Toolkit by Martin Gysel of the Paul-Scherrer Institute, Villigen, Switzerland, with the addition of function for the use of aircraft data by Katharina Heimerl was used to evaluate the raw data. The data analysis tool runs on IGOR (Wavemetrics, Inc.). The rBC mass concentration data used in this thesis is corrected to STP conditions. The rBC measurement range of the SP2 used during A-LIFE is 70 to 990 nm mass equivalent diameter assuming a void-free density of 1.8 g/cm^3 with the data in this range being a composition of the three incandescence channels BBHG, BBLG and NBLG. A time-offset to the Falcon time period of 1s was applied to account for inlet line length. Further, the total accumulation mode rBC mass concentration was calculated via an extrapolation of the BBLG measurements in the size range 80-500 nm by a lognormal fit averaged over the whole flight (for explanation of size distributions see chapter 2.1.1). Each flight has its own correction factor for total accumulation mode rBC mass concentration with the mean

correction factor for all flights plus/minus its standard deviation being 1.272 ± 0.087. The accumulation mode corrected rBC mass concentration was used for further analysis in this thesis. In-cloud data were excluded from the analysis to avoid artefacts from inlet effects in clouds.

A qualitative measure for coating thickness, the so called *coated fraction* was also analysed for this work. The coated fraction is here defined as the fraction of particles with a coating that induces a higher delay time and should not be mistaken by the fraction of coated material on the particle. It is determined by the time delay between the position of the scattering and the incandescence signal maximum. rBC particles can be grouped in two categories, thickly coated and thinly coated or uncoated: rBC particles with a coating thickness of up to 40 nm show a delay time between 0 and 1.5 μs, while particles with a coating above 30 nm show delay times of more than 2 μs (Subramanian et al. (2010), Moteki & Kondo (2007), Heimerl (2018)). Example signals for thickly and thinly or uncoated rBC particles can be seen in Figure 3.5. In this work, the coated fraction for rBC particles in the size range of 175 to 250 nm is shown.

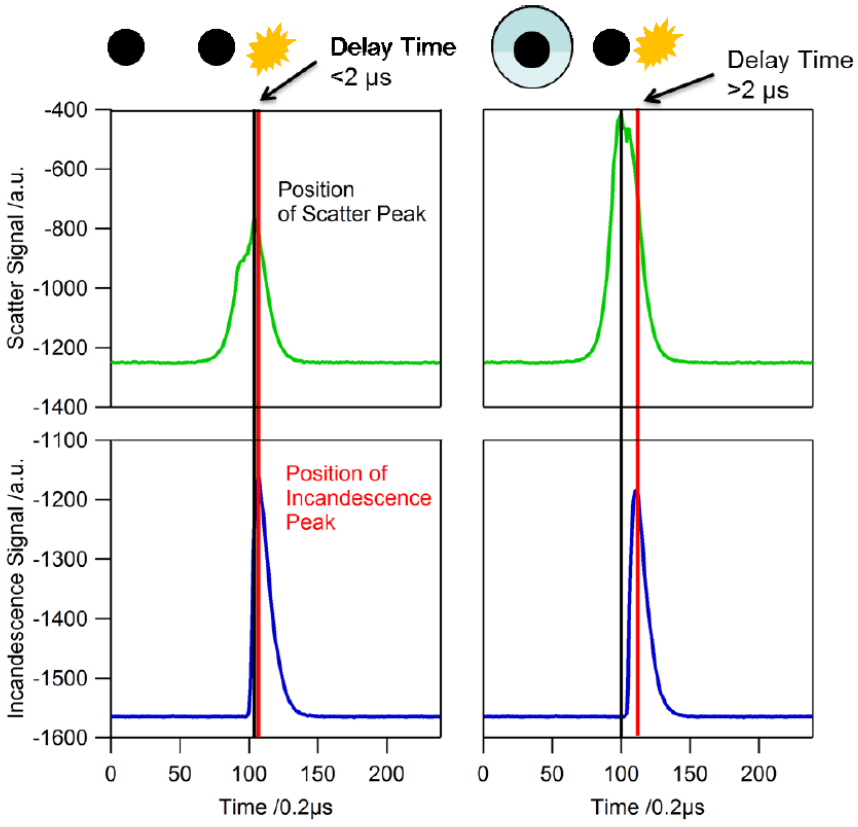

Figure 3.5.: Example scatter (green) and broadband incandescence (blue) signals of for an uncoated (left) and a thickly coated (right) rBC particle. the laser beam. The delay time is the difference of the peak scattering (black) and peak incandescence (red) signal. (Figure from Heimerl (2018)).

3.3.2. CAMS and FLEXPART

The offline Lagrangian transport and dispersion model FLEXPART ("FLEXible PARTicle dispersion model") version 8.2 was used to simulate aerosol mass concentrations along the A-LIFE flight routes as well as to classify aerosol source regions and types. These calculations were performed by Dr. Petra Seibert and Anne Tipka, MSc. FLEXPART is able to simulate transport and mixing of trace gases and aerosol. It does so by computing trajectories of notional particles that carry a certain mass each. The masses can change by various loss processes (Stohl et al. 2005). Of particular interest to this thesis are the simulated BC and mineral dust mass concentrations since BC was often measured in polluted dust layers.

The Falcon flight tracks were each divided into 1-minute intervals. Taking each interval as a starting point, 12-day backward trajectories were simulated considering mean wind transport and turbulent diffusion as well as particle loss processes including wet and dry deposition. Operational data from the European Centre for Medium-Range Weather Forecasts (ECMWF) were used as an input for meteorological data (time resolution: 3-hours, spatial resolution: 0.2° longitude and latitude). The output of the backward trajectory simulations are source-receptor sensitivity data, which were multiplied with emission data from the Copernicus Atmosphere Monitoring Service (CAMS) in order to calculate mass concentration for different aerosol types. The CAMS Emission data has a time resolution of 3-hours as well as a spatial resolution of 0.4° longitude and latitude. The domain for the aerosol emission input ranges from 25°W to 65°E longitude and 15°N to 65°N degrees latitude (Weinzierl et al. (2020), CAMS (n.d.)).

Black carbon and dust source regions

For black carbon and mineral dust, geographical source regions were defined in order to gain further information on their origin. Prior to this thesis dust was separated into four regions (Asia, Arabia, Eastern Sahara, and Western Sahara) and BC was only separated into European and African/Asian origin. Figure 3.6 shows the four dust regions, which were also used in the data analysis of this thesis.

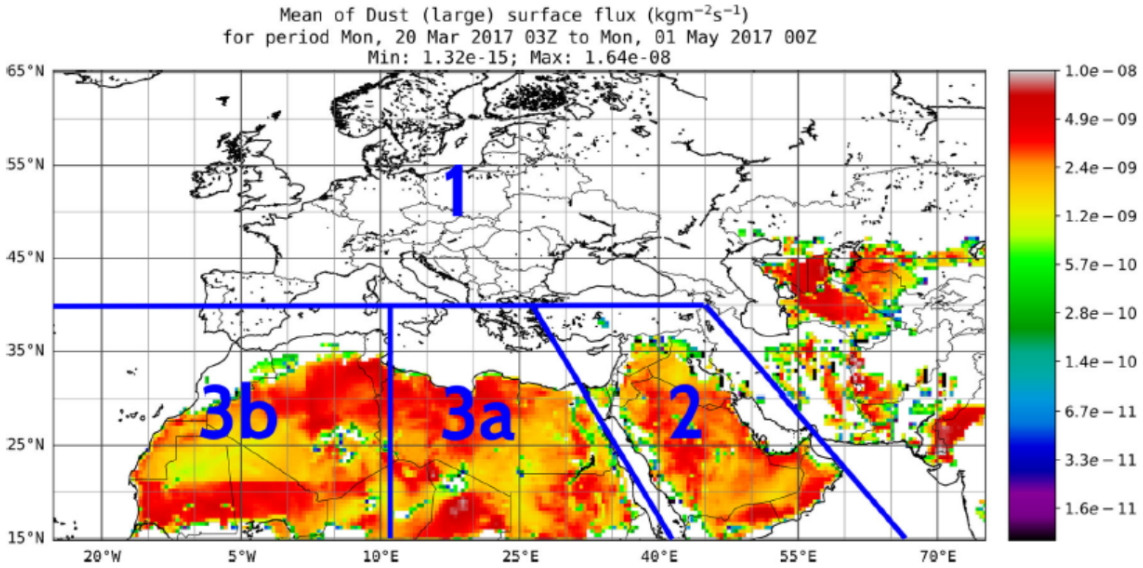

Figure 3.6.: Map of mean CAMS surface flux of dust for the period Monday 20th of March 03:00 UTC to Monday 1st of May 00:00 UTC 2017. The four dust source regions are separated by blue lines: 1 - Central Asia, 2 - Arabia, 3a - East Sahara, 3b - West Sahara. Figure from Weinzierl et al. (2020).

Since the goal of this work is to gain more detailed insight on BC origin, its source regions were further distinguished into twenty separate domains. The separation was done based on CAMS BC emission data focusing on regions with high BC emissions (figure 3.7) but also FLEXPART backward trajectories for the different flights (that were calculated earlier). Land and water were put into separate domains, but adding a few water grid points along the coastal regions to land since CAMS tends to attribute some emissions of e.g. coastal cities to water surfaces as can be seen in figure 3.7. Figure 3.8 shows the twenty BC source regions, which were named after the predominant countries / regions (Morocco, Tunisia + Algeria, Libya + W Egypt, E Egypt incl. Nile Delta, W Middle East, E Middle East, Turkey, North East Europe, South East Europe, North West Europe, South West Europe, Crete, Cyprus, North West Africa, North East Africa, Arabia, Other Land, Red Sea, Mediterranean Sea, Other Ocean). The Mediterranean coastal zone was divided into more separate regions because of the higher emissions there, but also because more trajectories reach these regions. The 'Other Land' category was not further distinguished due to the lack of trajectories going this far. The separation between North West and North East Africa is along the same longitude as the separation between the dust regions Western and Eastern Sahara.

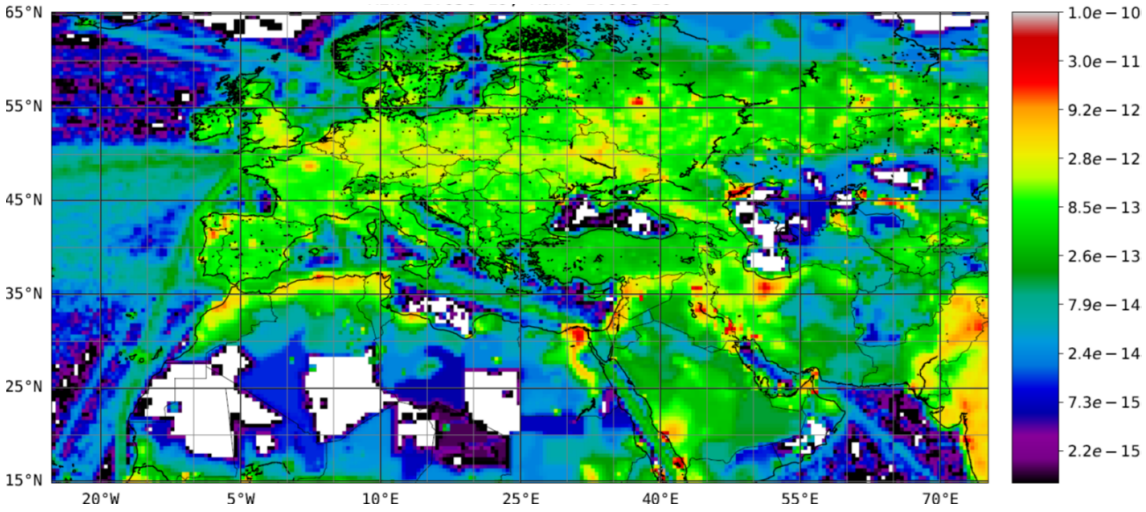

Figure 3.7.: Map of mean CAMS surface flux of black carbon (hydrophobic) in kilogram per square meter and second for the period Monday 20th of March 3 past midnight to Monday 1st of May midnight 2017. Figure adapted from Weinzierl et al. (2020).

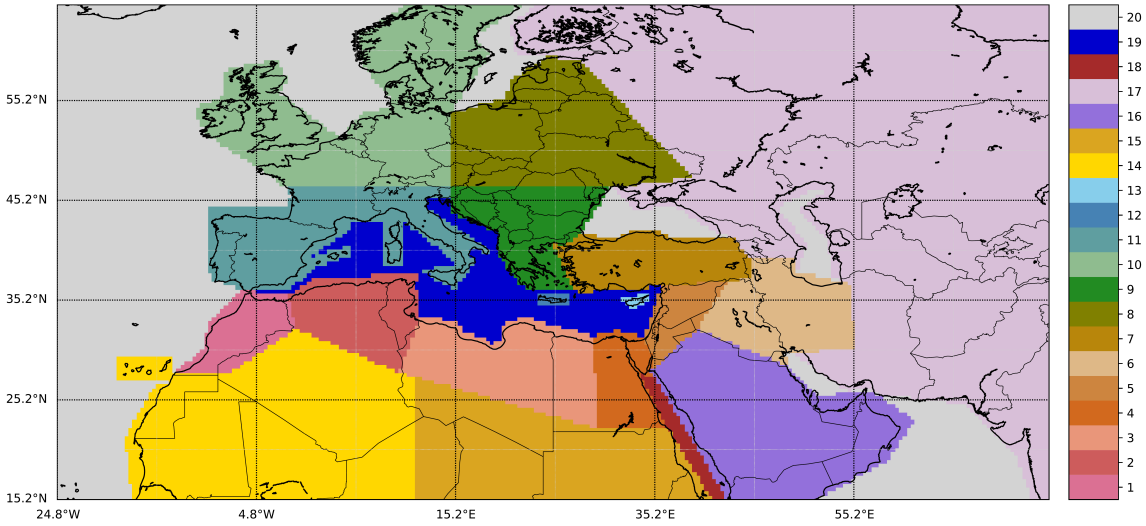

Figure 3.8.: Map showing the 20 defined BC source regions that were applied to the FLEXPART calculations: 1 - Morocco, 2 - Tunisia + Algeria, 3 - Libya + W Egypt, 4 - E- Egypt incl. Nile Delta, 5 - W Middle East, 6 - E Middle East, 7 - Turkey, 8 - North East Europe, 9 - South East Europe, 10 - North West Europe, 11 - South West Europe, 12 - Crete, 13 - Cyprus, 14 - North West Africa, 15 - North East Africa, 16 - Arabia, 17 - Other Land, 18 - Red Sea, 19 - Mediterranean Sea, 20 - Other Ocean.

Plotting the sum of the resulting BC mass concentrations calculated by FLEXPART against SP2 measured rBC mass concentrations shows good agreement between modelled and observational data. Figure 3.9 shows a scatter plot of the mass concentration in nanogram per cubic meter air of FLEXPART simulated BC vs. SP2 measured rBC as well as the 1:1 line. There is one data point for each minute of each flight (SP2 data is averaged),

cloud sequences are excluded. Individual FLEXPART simulated BC mass points scatter higher than the SP2 rBC mass. But as stated previously, rBC does not equal BC and rBC concentrations being slightly lower is expected.

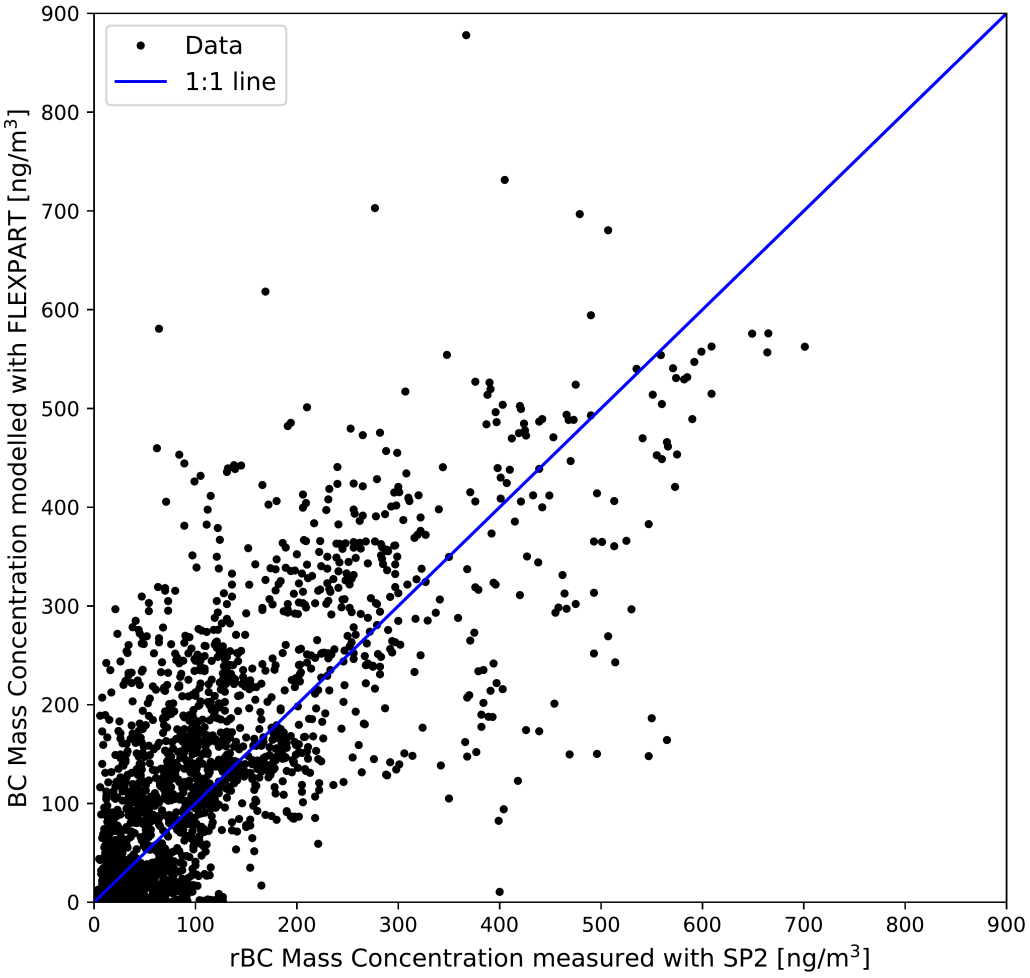

Figure 3.9.: Modelled FLEXPART BC mass concentration vs. observed SP2 rBC mass concentration. One data point per minute, data for all A-LIFE flights excluding cloud sequences. The 1:1 line is drawn in blue.

Figure 3.10 strengthens the statement above that the model data fits with the observational data. It shows a time series of an example flight (flight 20170406a) including the altitude of the Falcon as a solid blue line, the FLEXPART simulated BC concentration (sum of all source regions) as a dashed black line and the SP2 measurement data of rBC mass concentration (minute averages) as black triangle markers excluding cloud data. Model and observational data fit rather well with a few exceptions (for example at 06:00 UTC).

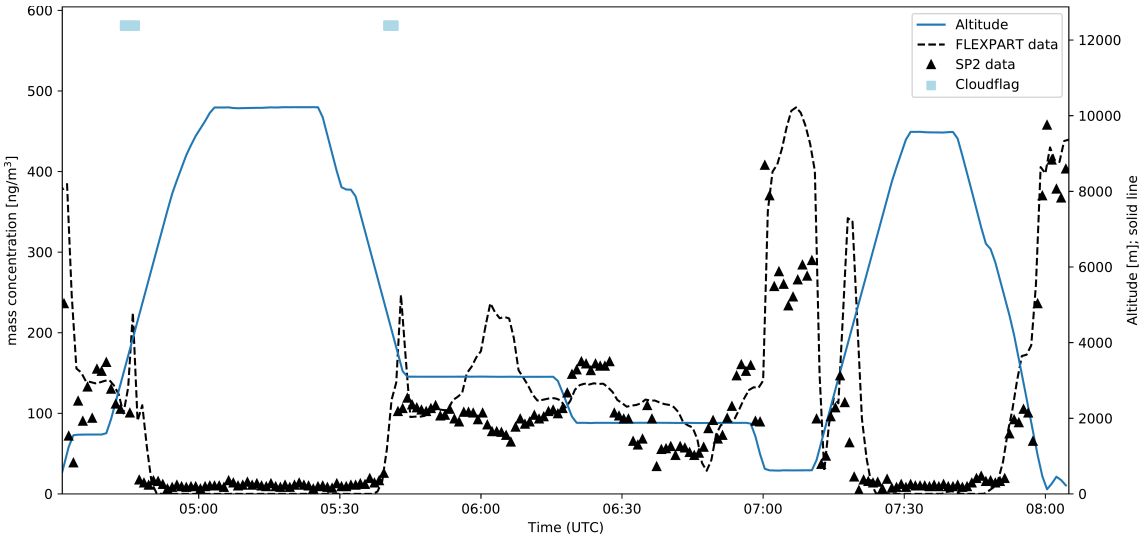

Figure 3.10.: Time series of BC concentrations from flight 20170406a: FLEXPART model BC concentrations (dashed line), SP2 measured rBC concentration (triangle markers), flight altitude (blue line).

3.3.3. Separation into different geographical flight regions

As described in the beginning of this chapter (see 3.1) a total of 22 flights were conducted mainly over the eastern Mediterranean with the Falcon during the A-LIFE field campaign. This includes two test flights over France, southern Germany, and Austria as well as transfer flights from Oberpfaffen to Paphos and back. The majority of the measurements took place in the vicinity of Crete and Cyprus, but there were also multiple flights over the Mediterranean Sea in the vicinity of Malta. In order to ascertain the typical BC composition with regards to source region for the geographical locations where flights took place and the time period of the field experiments, all flight paths were separated into four rectangular 'flight regions' for this thesis. They are *Central Europe*, *Malta and central Mediterranean*, *Crete and Aegean* and *Cyprus and Eastern Mediterranean* named after the predominant location of flights. In the further text the region names will be abbreviated to *Central Europe*, *Malta*, *Crete* and *Cyprus*. The flight regions were chosen to be rectangular (for simplicity) so that there are at least 20 FLEXPART simulated BC mass concentration data points per one degree latitude times one degree longitude for at least one grid point in each bordering row or column. Transfer flights were excluded. Figure 3.11 gives a visual explanation of the classification criteria.

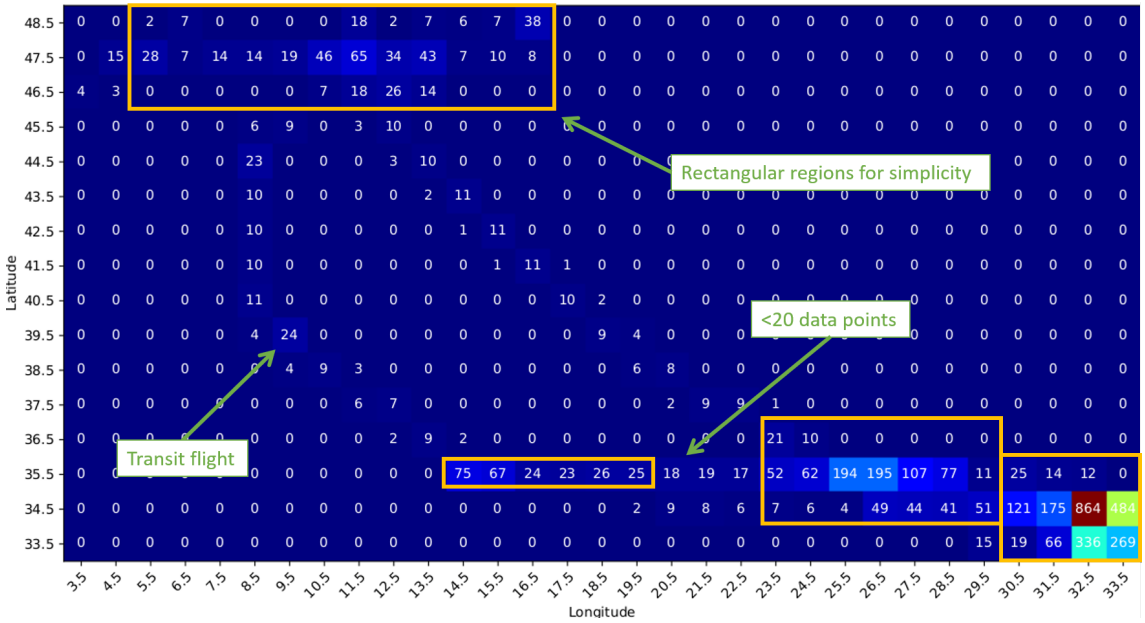

Figure 3.11.: Number of minute data points per 1 degree latitude x 1 degree longitude grid point of FLEXPART simulated BC data for all A-LIFE flights. Orange rectangles show the four defined flight regions: Central Europe, Malta and Central Mediterranean, Crete and Aegean as well as Cyprus and Eastern Mediterranean.

An overview of the border longitudes and latitudes of the resulting flight regions is given in table 3.2. Figure 3.12 shows an overlay of a map of Europe as well as the A-LIFE flight paths to give geographical context of the defined flight regions.

Table 3.2.: Table giving an overview of the four flight regions.

Flight Region (Abbreviation in bold)	**Description**	**Latitudes**	**Longitudes**
Central Europe	Flights above Austria, France, and Germany	46 - 49	5 - 17
Malta and Central Mediterranean	Flights over the Mediterranean in the vicinity of Malta / Italy	35 - 36	14 - 20
Crete and Aegean	Flights in the vicinity of Crete	34 - 37	23 - 30
Cyprus and Eastern Mediterranean	Flights in the vicinity of Cyprus	33 - 36	30 - 34

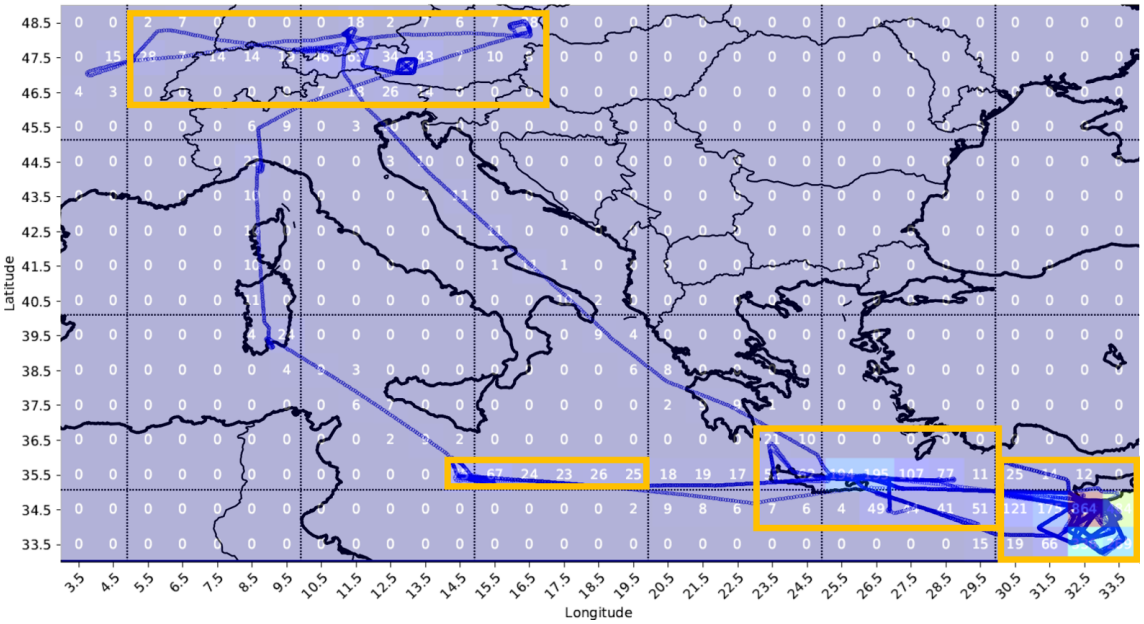

Figure 3.12.: Map of all flight paths (blue lines) overlayed with number of minute FLEXPART data points per grid point. The four flight regions (Central Europe, Malta, Crete and Cyprus) are again drawn as orange rectangles.

3.4. Data visualisation and further analysis

All plots in following two chapters were created in python via the matplotlib library. In the Statistics section of the chapter on FLEXPART simulated BC mass concentration results (chapter 4.2.2) modes were calculated in Python using the 'signal.argrelmax' function from the SciPy library with an order of five.

4. Results

This chapter focuses on results of rBC measurements made with an SP2 during A-LIFE as well as the outcome of the FLEXPART calculations for BC. First, vertical profiles of rBC median mass concentrations as well as coated fraction of rBC particles will be shown for all flights in total and for four selected flight regions. Then the FLEXPART modelled BC mass concentration results will be discussed by the example of two chosen flights. Further, this chapter provides statistical data (mean, standard deviation, median, first and third quantiles and mode) of FLEXPART modelled BC mass concentrations for twenty selected source regions. At the end of the chapter altitude depended average rBC mass concentrations for the A-LIFE sequences including information on the sequence class will be presented.

4.1. rBC vertical profiles

Figure 4.1 shows median vertical profiles of rBC mass concentration for the four selected flight regions that are described in Table 3.2 and can be seen in Figure 3.12 as well as all flights in total. rBC median mass concentrations are plotted for altitude intervals of 1 km starting from 0 (sea level) to 11 km. Values for Central Europe are colored red, Malta blue, Crete green, Cyprus purple and all flights black. For the median vertical profile for all flights the first and third quantiles are included as a grey shaded area. The other median vertical profiles including quantiles for each flight region can be found in the appendix B.3. For comparison, data published in Schwarz et al. (2017) is also included in the graph as dashed and dotted lines. Vertical profiles of rBC mass mixing ratio were converted into mass concentration at STP conditions. The data was collected in the time period between 2011 and 2013 through several different aircraft field experiments including CONCERT, ACCESS, DC3, SALTRACE and SEAC4RS for different geographical regions. The regions are Europe, Senegal, Barbados, the Arctic and North America (NA).

rBC mass concentrations measured during A-LIFE at low altitudes (below 2 km) ranged from 7 to 717 ng/m^3 with a mean concentration of 212 ng/m^3. In general, rBC mass concentrations were decreasing with increasing altitude. The graph shows that median rBC mass above central Europe decreased faster with increasing altitude and tended to be lower in general. At altitudes above 5 km the A-LIFE data for central Europe fits very well with the Schwarz et al. (2017) data. Median rBC mass over the Mediterranean in the vicinity of Malta showed more variability with altitude, it must be noted, however, that only a

few data points were collected in some altitude intervals in this region (e.g. only 13 data points in sum from 0 to 2 km). Still, the lower values at low altitudes compared to the other flight regions are probably due to the fact that most of the flights took place over the Mediterranean Sea. The Falcon only landed in Malta once, whereas there are multiple landings in the other flight regions. Further, the low mass concentrations at low altitudes indicate little BC emissions in this region since the majority of BC sources are located at the Earth's surface as was explained in chapter 1.2.1. BC mass concentrations at higher altitudes are similar to other flight regions, indicating that BC was probably transported there. At higher altitudes (above 5 km) median rBC mass over Crete was noticeably higher than over the other regions. All curves show a steeper slope at high altitudes with median rBC mass increasing again in the highest altitude intervals. Taking all flights into account, median rBC mass ranged from 12 to 223 ng/m^3.

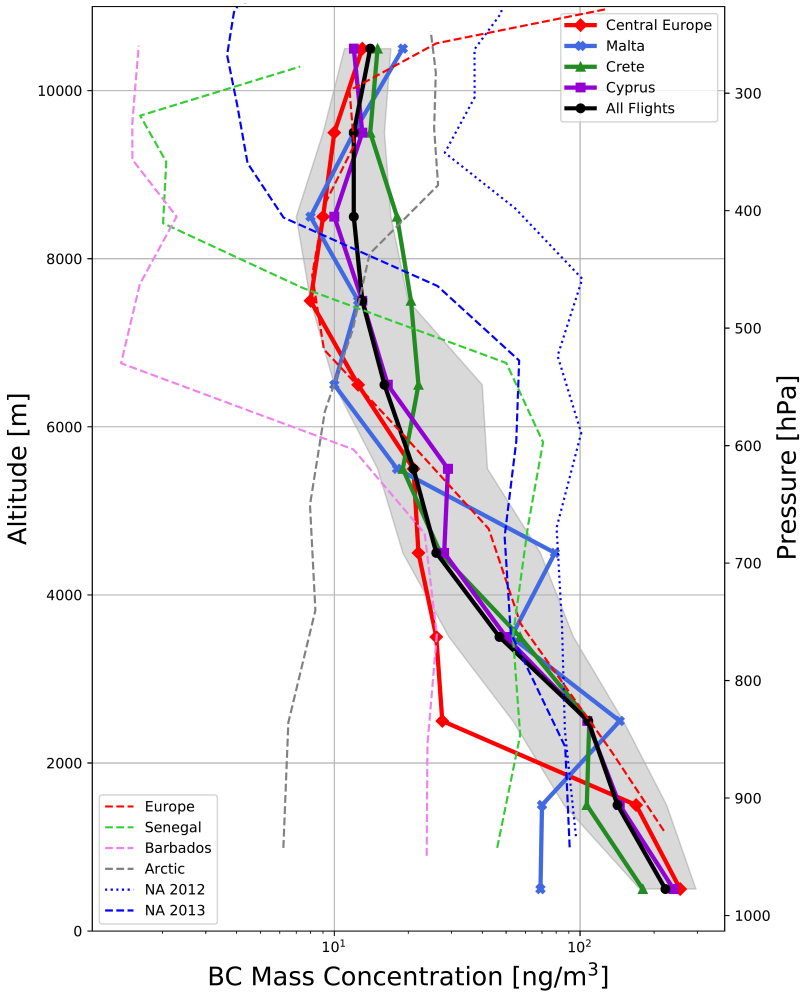

Figure 4.1.: Median vertical profiles of rBC mass concentration measured during A-LIFE for the individual flight regions (colored) , as well as all flights (black) are shown in bold lines. The flight regions are Central Europe (red), Malta (blue), Crete (green) and Cyprus (violet). Q1 and Q3 are included as shaded grey area for all flights. For comparison, vertical profiles of rBC mass concentrations over different geographical regions published in Schwarz et al. (2017) are plotted as dashed and dotted lines. The geographical regions are Europe (red), Senegal (green), Barbados (pink), the Arctic (grey), and North America (2012: blue dotted, 2013: blue dashed).

Figure 4.2 shows median vertical profiles of SP2 measured rBC coated fraction for rBC sizes from 175 to 250 nm. As was described in chapter 3.3.1, the coated fraction is defined as the fraction of rBC particles with a coating that induces a higher delay time between scattering and incandescence signal (> 2 μs). Uncoated or thinly coated rBC particles with coatings smaller than $\sim$ 30 nm have shorter delay times and therefore don't classify as 'coated'. For all sequences the median coating thickness (obtained via Leo-fit) in the size range 175 to 250 nm was 36 nm.

The left graph in Fig. 4.2 shows median vertical profiles for all flights as well as the four flight regions color coded in the same way as Fig. 4.1. The median rBC coated fraction for all flights was equal for almost all altitude intervals considering measurement errors with only a small increase above 8 km. Similar to the median mass concentration values, there was a high variability above Malta, which again can be explained by a low number of data points in some altitude intervals. More significant is the variability above central Europe as well as the higher coated fraction in that region indicating BC with a higher age. The right graph shows the median vertical profiles of rBC coated fraction (again for rBC sizes from 175 to 250 nm) for Crete only including first and third quantiles in order to highlight the abrupt increase at altitudes above 9 km up to a coated fraction of 0.24, meaning a fourth of measured rBC particles had thick coatings. This indicates that there was a higher percentage of aged BC at high altitudes above Crete than at low altitudes.

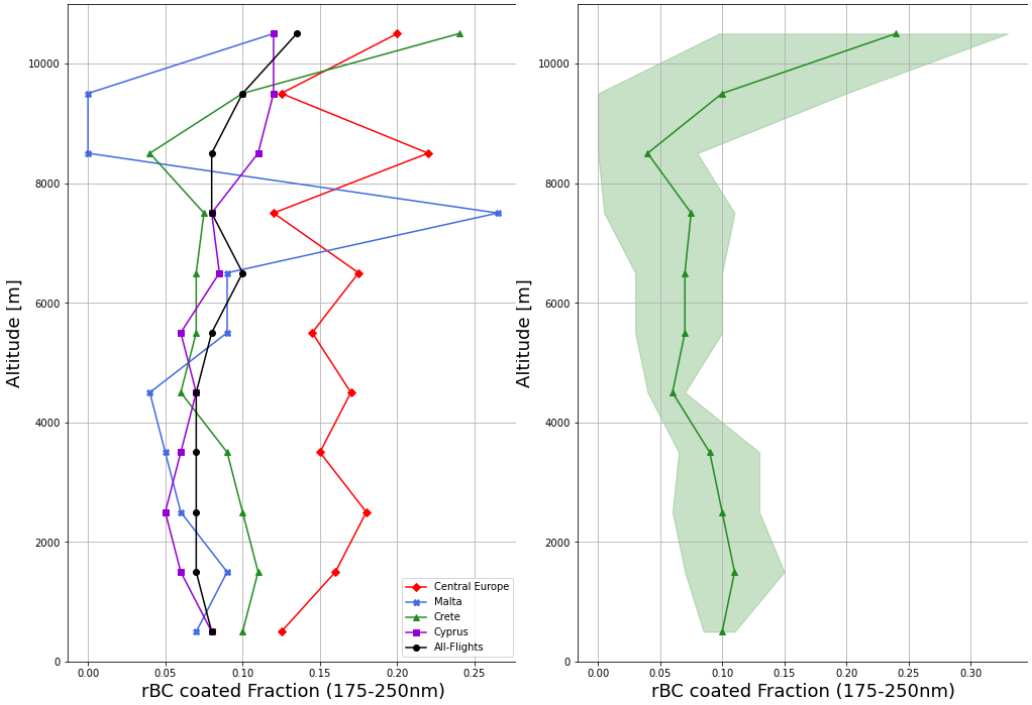

Figure 4.2.: Left: median vertical profiles of rBC coated fraction for the individual flight regions (colored lines) and all flights (black line). The flight regions are: Central Europe (red), Malta (blue), Crete (green) and Cyprus (violet). Right: vertical profile only for Crete including first and third quantile as shaded areas (green).

The coated fraction values depicted here are lower than comparable results in the literature. McMeeking et al. (2011), for example, found that the number fraction of thickly coated rBC particles over the United Kingdom ranged between 16 and 37 % (depending on the observed air mass). They analysed SP2 measurements of rBC obtained in 2008 and 2009 and calculated the coated fraction based on the time delay between incandescence and scattering signal (as was done in this work). Their results show lower coated fractions for urban plumes, while coated fractions in European continental outflow were higher. This could indicate that a high percentage of rBC measured over the eastern Mediterranean during A-LIFE stems from urban sources. Another explanation for the low values could be that the median coating thickness for the different altitude intervals is close to the separation between thin and thick coating (∼30 nm). The low values don't necessarily indicate that most measured rBC particles are uncoated, but rather that particles with coatings close to 30 nm, which are classified as 'thinly coated', make up a large percentage. For a deeper understanding of the matter more detailed calculations of coating thickness time series, exceeding the scope of this thesis, are needed.

4.2. FLEXPART simulated BC mass concentration

4.2.1. Time series of BC mass concentrations for example flights

Figure 4.3 shows a time series of SP2 measured rBC mass concentrations together with FLEXPART simulated BC mass concentrations in ng/m^3 exemplary for the flight on the 6th of April 2017 (flight 20170406a), which took place over the Mediterranean south of Cyprus. In addition to the BC time series already shown in Fig. 3.10, the FLEXPART modelled BC source region contribution for each time step is included in color. A map of the twenty selected BC source regions can be seen in Fig. 3.8. The flight altitude is plotted as a solid line and the measured rBC mass concentration is depicted as triangle markers excluding cloud sequences, which are indicted as blue bars. West Middle East is the predominant source region for this flight, with high mass concentrations at low altitudes. Above 2 km there are noticeable contributions from East Egypt incl. Nile Delta, but also Morocco and North-East Europe.

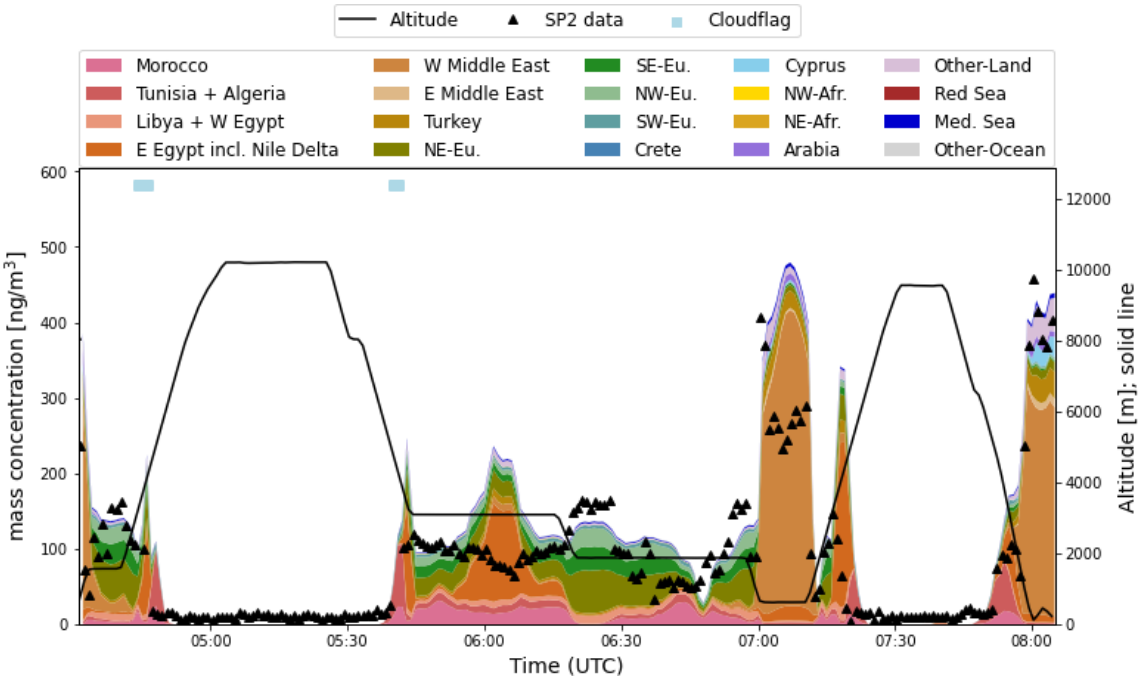

Figure 4.3.: Time series of SP2 measured rBC mass concentration (black triangles) and FLEXPART simulated BC concentration for all source regions for flight 20170406a including altitude (black solid line) and cloud sequences (blue squares).

Another exemplary BC time series can be seen in Figure 4.4 showing the flight on the 22nd of April 2017 (flight 20170422a), which took place in roughly the same area as 20170406a, although at a later time. The FLEXPART results show a different source region composition than for flight 20170406a. Here Tunisian and Algerian BC have the highest contribution to BC mass, followed by BC originating from the E Egypt incl. Nile Delta and SW Europe. West Middle Eastern and East European BC is not visible in the graph.

In both plots BC originating from Cyprus can be seen in light blue at very low altitudes. The two flights presented were chosen due to their different, but rather 'typical' composition in terms of dominant BC origin observed during A-LIFE, as will be discussed in the next section.

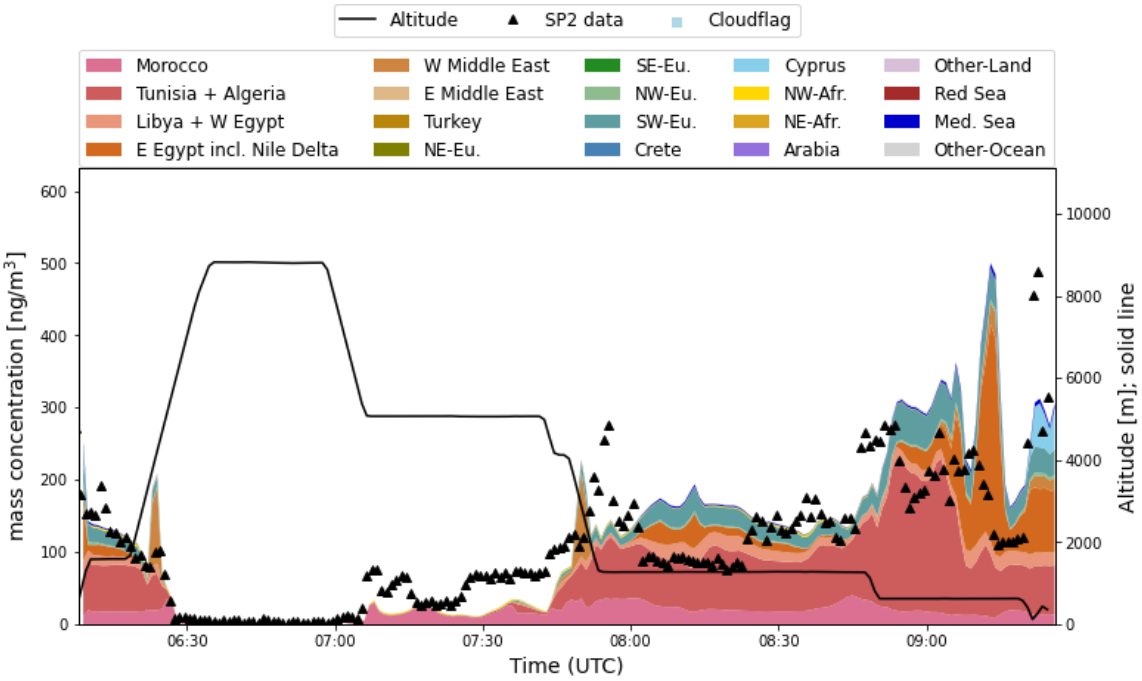

Figure 4.4.: Time series of SP2 measured rBC mass concentration (black triangles) and FLEXPART simulated BC concentration for all source regions for flight 20170422a including altitude (black solid line) and cloud sequences (blue squares).

4.2.2. Statistical parameters for BC source regions

Table 4.1 shows mean mass concentration values as well as other statistical parameters such as median, standard deviation, quantiles and modes for the twenty selected BC source regions. The most dominant source regions for all flights in terms of mean mass concentration are West Middle East, followed by Tunisia + Algeria and South-West Europe with high contributions also from Morocco, Libya + West Egypt, North-West and North-East Europe. It must be noted though that the values highly depend on the location and time of flights and must therefore be viewed in context of sampling bias. The last column of Tab. 4.1 shows the relative fraction of data points where modelled BC mass concentrations were equal to zero (BC=0). Modes are included in the table due to the fact that histograms of the BC mass concentration for different source regions show different frequency distributions, with some having a clear one-modal frequency distribution, while other show two or even three modes. Figure 4.6 shows four exemplary histograms (all other histograms can be found in the appendix B.5) for the most dominant source regions West Middle East, Tunisia + Algeria and South-West Europe, but also Turkey as an example for a bimodal frequency distribution. For all histograms BC mass concentration values are binned from 10^{-7} to 10^{3} ng/m^3 in 25 logarithmic bins. It can be seen that West Middle Eastern BC is shifted to higher mass concentration than BC from other source regions, which is one explanation for its predominance.

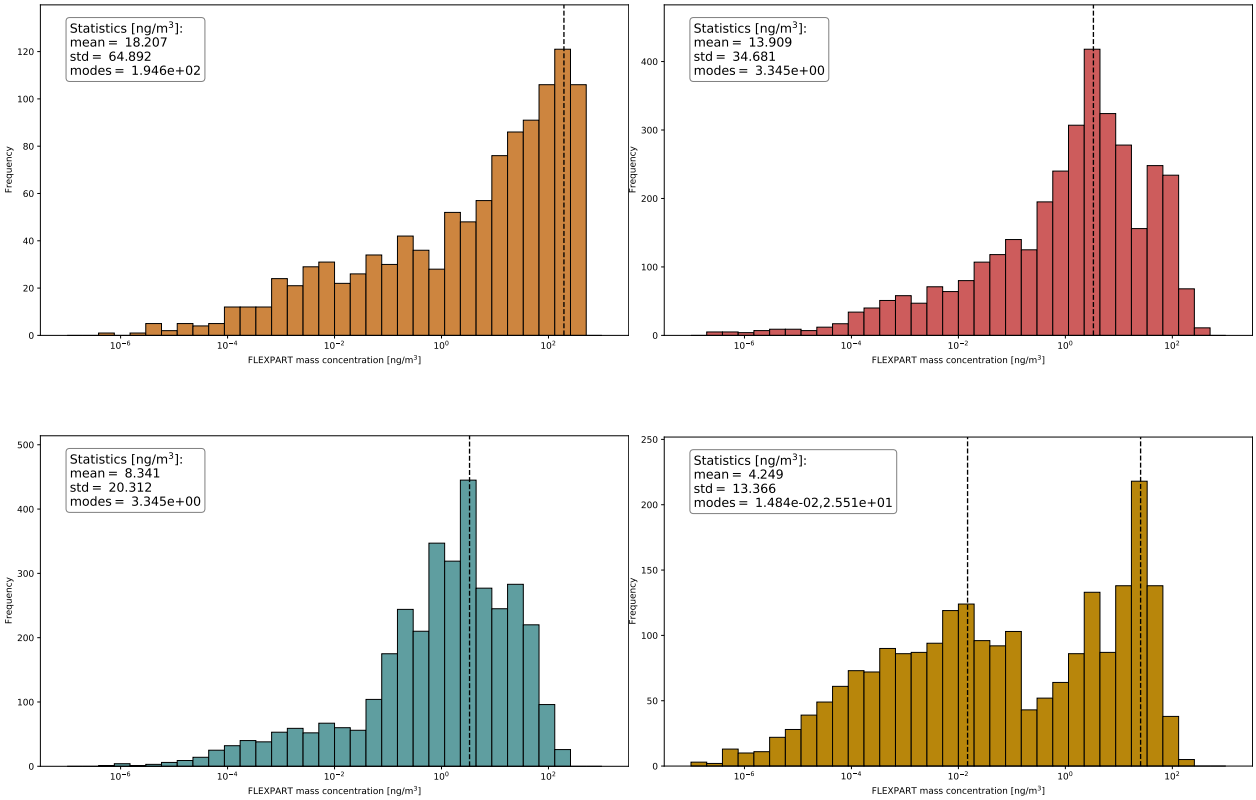

Figure 4.6.: Histograms of FLEXPART simulated BC mass concentrations over all flights for source regions: West Middle East (upper left), Tunisia + Algeria (upper right), South-West Europe (lower left) and Turkey (lower right). Modes (of frequency) are drawn in as vertical dotted lines.

Table 4.1.: Source region statistics

BC source regions	**Mean [ng/m^3]**	**Std [ng/m^3]**	**Median [ng/m^3]**	**Q1 [ng/m^3]**	**Q3 [ng/m^3]**	**Modes (of frequency) [ng/m^3]**			**relative fraction BC=0**
Morocco	7	15	0.33	0.00038	5.7	26			0.1931
Tunisia + Algeria	14	35	0.77	0.00065	7.1	3.4			0.2049
Libya + W Egypt	3.0	6.5	0.13	0.0	2.8	6.6			0.2557
E Egypt incl. Nile Delta	8	37	0.0	0.0	0.12	0.0075	1.7		0.5781
W Middle East	18	65	0.0	0.0	0.00010	190			0.7436
E Middle East	0.8	4.0	0.0	0.0	0.0	0.00050	6.6		0.7935
Turkey	4	13	8.2e-06	0.0	0.083	0.015	26		0.4791
NE Europe	4	13	0.0014	0.0	1.4	0.0038	13		0.4183
SE Europe	3	11	0.011	0.0	1.2	0.029	13		0.3042
NW Europe	6	23	0.15	0.0	2.3	0.44			0.2628
SW Europe	8	20	0.69	0.0012	4.9	3.4			0.2006
Crete	0.2	1.7	2.9e-05	0.0	0.0094	0.058			0.4538
Cyprus	1.0	5.0	0.0	0.0	0.00052	0.029	1.7		0.6990
NW Africa	0.395	0.72	0.023	3.2e-05	0.43	0.44			0.1995
NE Africa	0.1	1.1	0.00029	0.0	0.026	0.00050	0.058		0.33586
Arabia	0.8	3.7	0.0	0.0	0.0	0.0075	13		0.7889
Other Land	1.4	6.8	0.0	0.0	0.0043	0.0038	3.4		0.6202
Red Sea	0.04	0.37	0.0	0.0	0.0	6.6e-5	0.029	3.4	0.8377
Mediterranean Sea	1.2	2.9	0.15	8.5e-05	13	1.7			0.2165
Other Ocean	0.41	0.68	0.14	0.00079	0.56	0.86			0.16447

4.3. rBC mass in mineral dust layers

High rBC mass concentrations were measured in dust layers. There are 2 A-LIFE sequences classified as *polluted Saharan* and 8 as *polluted Arabian dust* as well as 80 *moderately polluted Saharan* and 8 *moderately polluted Arabian dust* sequences. Saharan and Arabian dust falling into the clean category make up 64 and 2 sequences, respectively. From these numbers alone it can be seen that Arabian dust tends to be more polluted than Saharan dust. It must be mentioned though that sequences that don't qualify as polluted do not automatically show low rBC concentration. The pollution criteria are mainly based on the ratio of the number concentration of coarse particles (larger 800 nm in diameter) to rBC mass concentration as mentioned in chapter 3.1.1.

Figure 4.7 shows sequence averages of SP2 measured rBC mass concentration vs. altitude for the different sequence classes. Since the focus of this thesis is on BC in mineral dust, polluted and moderately polluted mixtures with enhanced coarse mode concentration were grouped together. The same was done for polluted and moderately polluted mixtures with low coarse mode contribution. The plot shows that Arabian dust, whether polluted or not, shows higher rBC concentration than Saharan dust (mean rBC mass for all pollution levels: Saharan dust: 72 ng/m^3; Arabian dust: 246 ng/m^3). Further, dust of Arabian origin was observed at lower altitudes than Saharan dust layers.

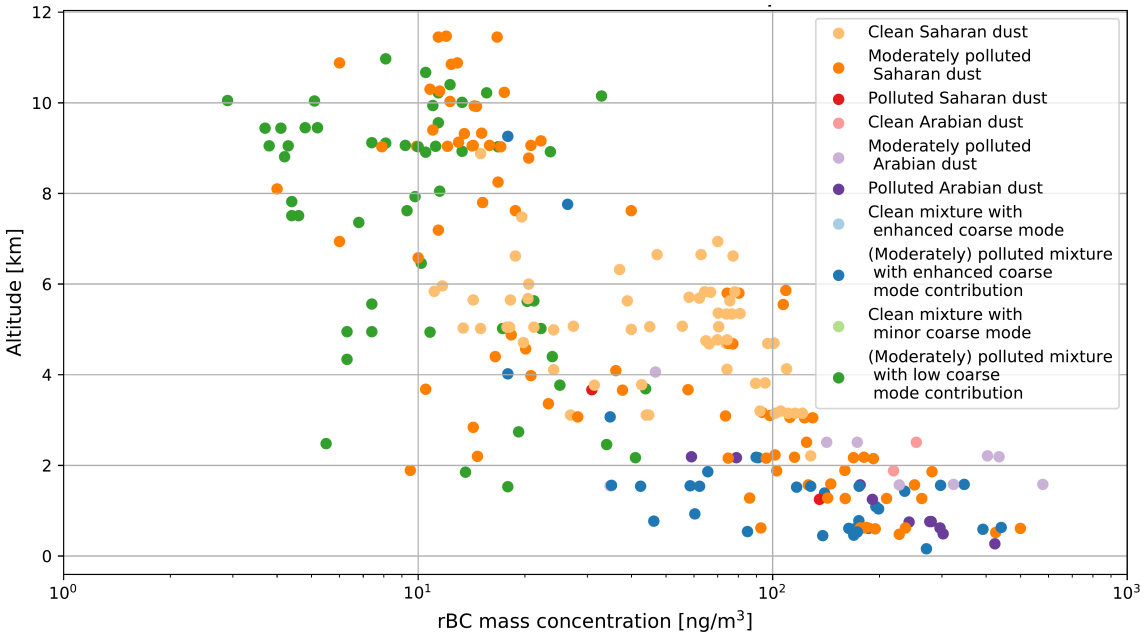

Figure 4.7.: Altitude dependent average rBC mass concentration for all sequences. Sequence classes (for classification scheme see chapter 3.1.1) are color coded: Background (pink), Mixture with coarse mode (light blue), Polluted mixture with coarse mode (dark blue), Mixture without coarse mode (green), Polluted mixture without coarse mode (dark green), Saharan dust (orange), Polluted Saharan dust (red), Arabian dust (light purple), Polluted Arabian dust (dark purple).

5. Discussion

5.1. Black carbon source regions dependent on altitude

In Figure 5.1 1-min data points from all flights are plotted as a 3D diagram with longitude on the x-axis, latitude on the y-axis and altitude on the z-axis. Here the previously introduced BC source regions are grouped into Europe (Turkey, NE Europe, SE, Europe, NW Europe, SW Europe, Cyprus, Crete) and Africa/Asia (Morocco, Tunisia + Algeria, Libya + W Egypt, E Egypt incl. Nile Delta, W Middle East, E Middle East, NW Africa, NE Africa, Arabia). Here it must be noted that Africa refers to north African regions and Asia refers to south west Asian regions. The data points are color coded with the predominant BC source where dark blue means 100% African/Asian origin, dark red means 100% European origin and white means a 50:50 mix. In Figure 5.2 mean SP2 rBC mass concentrations of all A-LIFE sequences are plotted against altitude with the same color coding. Both plots show that BC measured during A-LIFE tends to originate predominantly from Africa and Asia and to a smaller extent from Europe. BC of European origin is more dominant at lower altitudes and occurs in generally lower mass concentrations than African/Asian BC, which makes up the majority of data points and is predominant at high altitudes and high mass concentrations. Above Europe BC of dominant European origin was measured at low altitudes. At higher altitudes the dominant BC source region shifts to African/ Asian origin meaning BC from Africa/Asia must have been transported to Europe at altitudes above roughly 4 km.

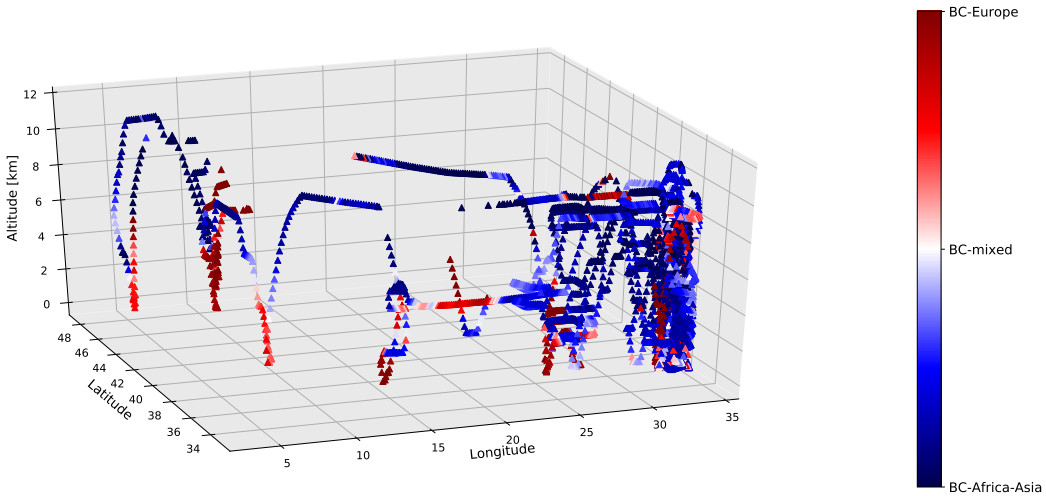

Figure 5.1.: 3D plot of gps-coordinates of 1 minute data points for all flights. Predominant BC source is color coded: 100% European origin in red, 100% African/Asian origin in blue and a 50:50 mix in white.

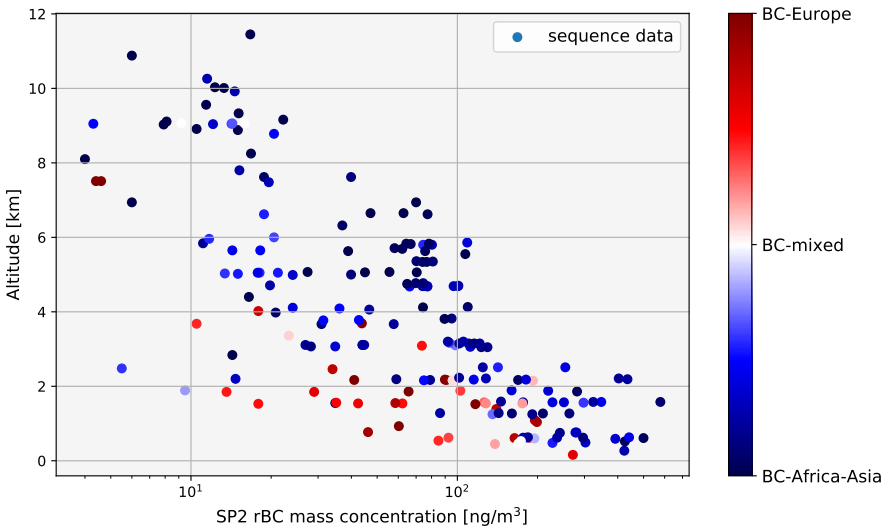

Figure 5.2.: Altitude (y-axis) vs. SP2 measured rBC mass for sequence averages. Predominant BC source is color coded the same as in Fig. 5.1.

Figure 5.3 gives a closer look at the BC source for flights above Europe, where the shift from European to African/Asian BC origin can be seen. The BC origin is likely dependent on the weather conditions during the flights in central Europe. Figure 5.4 strengthens this argument as it shows the wind direction the Falcon meteorological instrumentation. The figure shows that for data points with high African/Asian BC fraction, S and SSW wind was measured.

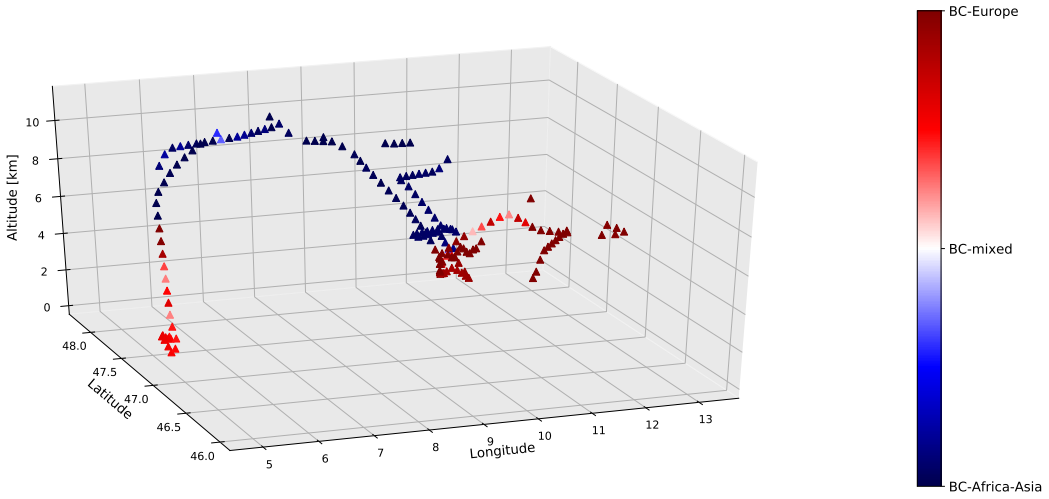

Figure 5.3.: 3D plot of gps-coordinates of 1 minute data points for Flights above central Europe. Predominant BC source is color coded: 100% European origin in red, 100% African/Asian origin in blue and a 50:50 mix in white.

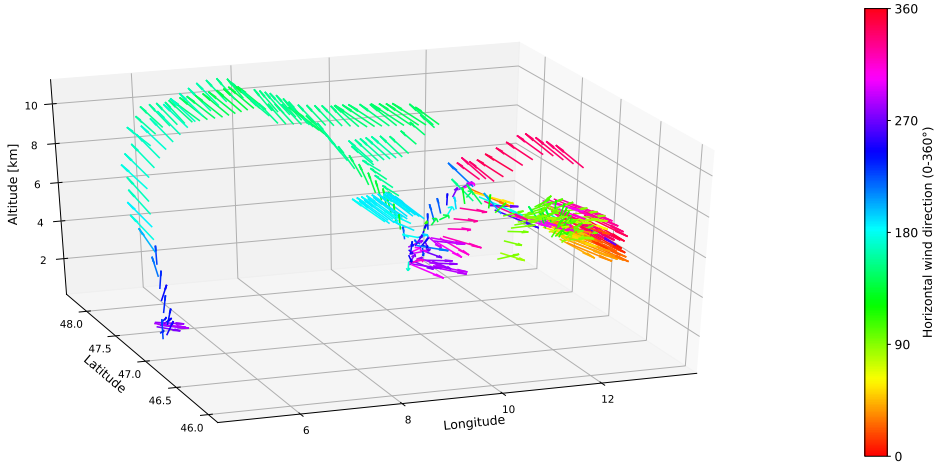

Figure 5.4.: 3D quiver plot of gps-coordinates of 1 minute data points for flights above central Europe including 3D wind direction as vectors. The horizontal wind direction is color coded: 0° / 360°, meaning N wind in red, 90° (E wind) in green, 180° (S wind) in cyan and 270° (W wind) in purple

As was already shown in the previous chapter by median vertical profiles, rBC mass decreases with altitude. This can also be seen in the FLEXPART BC results. Figure 5.5 shows the mean FLEXPART simulated BC concentration for altitude intervals of 1 km from 0 to 11 km. Not only the mean BC mass concentration decreases with increasing altitudes, but also the mass predominance of BC of W Middle Eastern origin (beige-brown color).

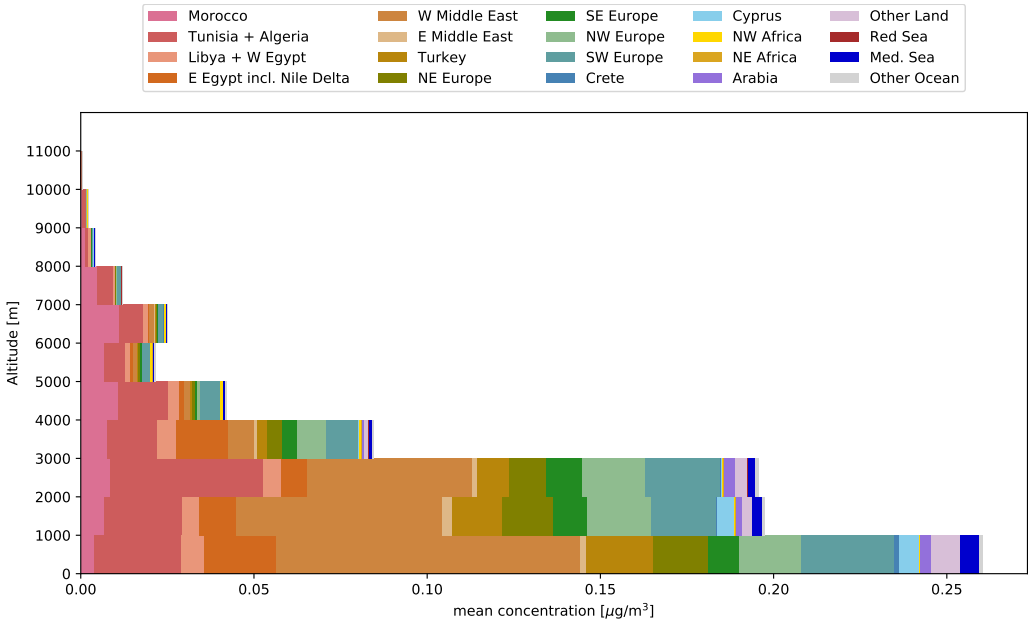

Figure 5.5.: Mean values of FLEXPART simulated BC source region mass concentration as horizontal stacked bar charts dependent on altitude for all flights.

A more detailed view on the BC composition in terms of source region (independent of mass concentration) is given in Figure 5.6. As was shown above, the percentage of European

BC is decreasing with altitude, which can be seen above 4 km. South West European BC (turquoise) seems to be the exception with a relative concentration that is rather constant with altitudes. Above 4 km the dominant BC source shifts to Morocco (pink) and Tunisia + Algeria (red) and North West African BC (yellow) take up a higher fraction, as does BC from the region Other Ocean (grey) indicating that BC was transported further distances at higher altitudes. At very low altitudes below 2 km BC originating from Cyprus (light blue) can be seen in the graph, although it makes up only a small percentage.

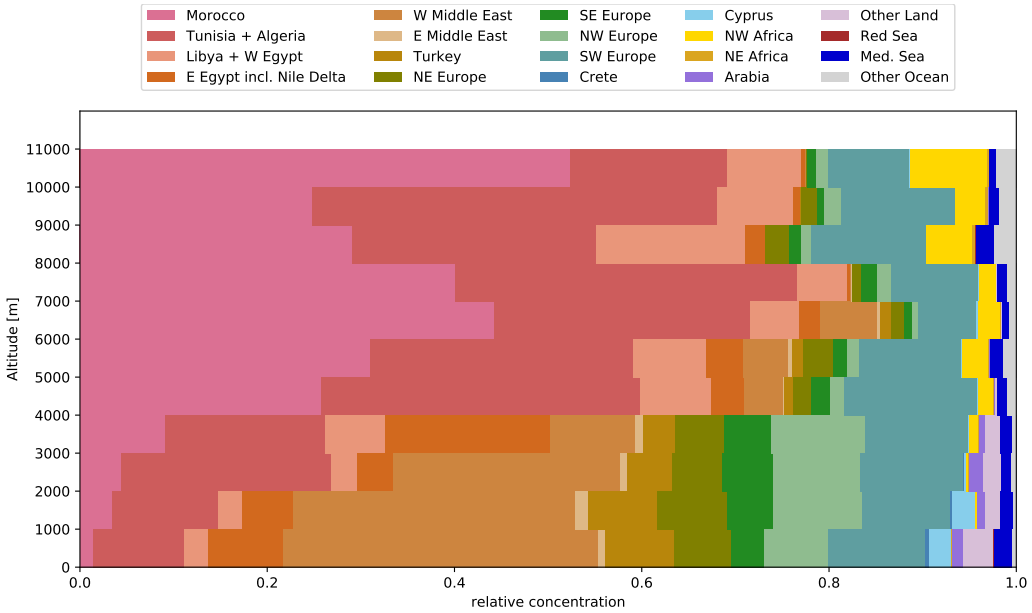

Figure 5.6.: Relative values of FLEXPART simulated BC source region mass concentration as horizontal stacked bar charts dependent on altitude for all flights.

5.1.1. Flight regions

Both source region composition and mass concentration of BC observed during A-LIFE not only depend on altitude, but also the geographical region of the flights. Figure 5.7 shows the mean FLEXPART simulated BC concentration for twenty selected source regions as stacked bar plots for each of four chosen flight regions. With 31 ng/m^3 FLEXPART simulated BC over central Europe has the lowest mean mass concentration, while the mean BC mass concentration over Cyprus is the highest with 96 ng/m^3. BC over Malta and Crete show similar mean mass concentrations of 76 ng/m^3 and 74 ng/m^3 respectively. In order to make the general geographical source for each flight region visible at first sight, black lines are drawn in the graph to separate dominant African, Middle Eastern and European source regions. African source regions including Morocco, Tunisia + Algeria, Libya + W Egypt and E Egypt incl. Nile Delta are separated from Middle Eastern source regions including W Middle East, E Middle East and Turkey by a dashed black line. Between Middle Eastern and European source regions (North East Europe, South East Europe, North West Europe, South West Europe, Crete and Cyprus) there's a dotted black line

and a dash-dotted black line separates European sources from other sources. 'Other' refers to all regions further away (North West Africa, North East Africa, Arabia, Other Land, Red Sea, Mediterranean Sea, Other Ocean), which were not further distinguished due to their low mass concentrations.

BC over central Europe mainly originates from European sources, namely North West and South West Europe. BC over Malta has African and European sources, with the most prominent source regions being Tunisia and South West Europe. BC over Crete has mixed origin, mainly of African and European sources (Tunisia + Algeria, South West Europe and North West Europe are the most common). The most dominant sources for BC over Cyprus are Middle Eastern, with W Middle Eastern BC making up the highest percentage, but African and European sources also show high mass concentrations. The graph also shows that local BC emissions originating from Crete and Cyprus only make up a very small percentage of mean BC measured over Crete and Cyprus, respectively. This strengthens the previously made statement that the majority of BC is not of local origin but was transported to the measurement area.

Table 5.1 presents statistical parameters such as mass concentration mean, standard deviation and median for both SP2 measured rBC and FLEXPART simulated BC as well as coated rBC fraction for each flight region. Additionally, ratios of SP2 measured rBC mass and FLEXPART modelled BC mass are given. SP2 measured rBC mass and FLEXPART modelled BC mass fit together best for Cyprus where the ratio of their means is very close to 1 (1.04) and worst for Crete where mean rBC mass is about 50% smaller than BC mass (ratio of 1.52). Here it must be noted that the standard deviations are rather high due to the fact the data points are taken from all altitudes and there is a large decrease of rBC and BC mass concentrations with increasing altitude, as was previously shown. It still makes sense to look at the mean and median data of all altitudes since the goal here is to compare the different flight regions independent of altitude. For Malta, Crete and Cyprus the ratio FLEXPART mass mean to SP2 mass mean is greater than 1 meaning more FLEXPART BC than SP2 rBC. This is expected because the SP2 is only able to measure rBC, a 'sub-type' of BC, as was explained in the introduction. The ratio is smaller than 1 (0.81) for central Europe, though, indicating higher measured than modelled mass concentrations. In central Europe the coated fraction is also the largest which indicates a high percentage of aged BC. This could indicate BC populations older than 10 days since FLEXPART calculations only go back 10 days. It could also be that FLEXPART assumes lower concentrations above central Europe than were measured by overestimating wet and or dry deposition. More data and a closer analysis exceeding the scope of this work is needed before any conclusions can be drawn.

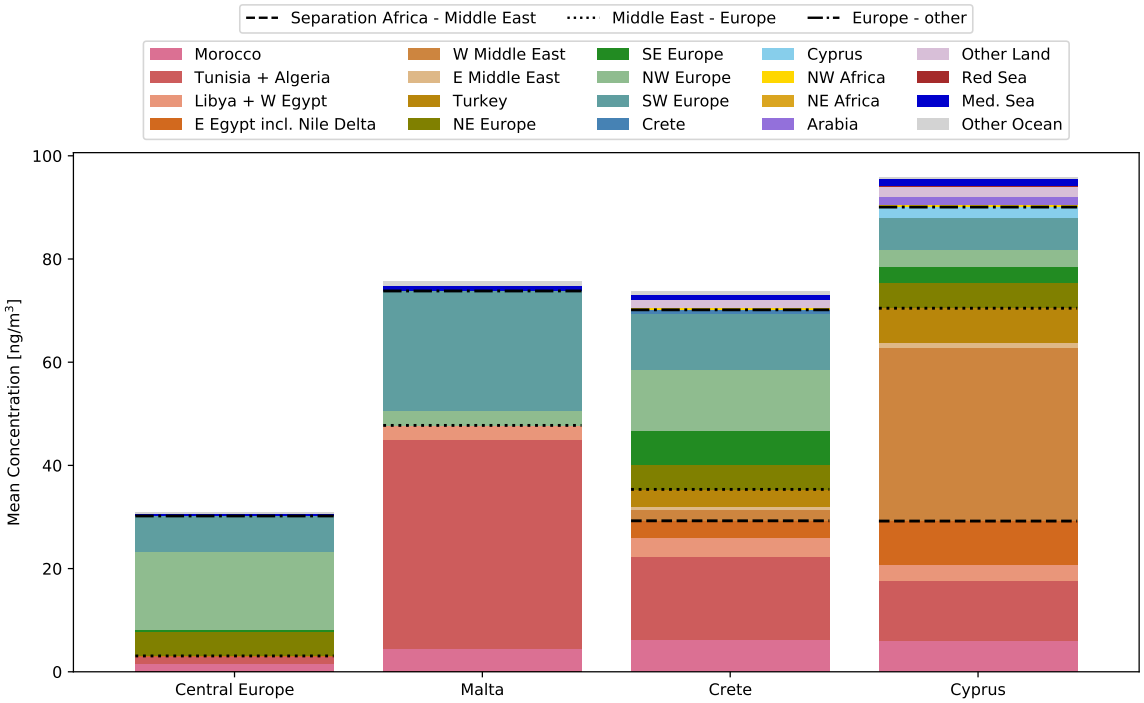

Figure 5.7.: Mean values of FLEXPART simulated BC source region mass concentration as stacked bar charts for the flight regions: Central Europe, Malta, Crete and Cyprus. Horizontal black lines separate source regions of the same general geographical region (dashed line: separation between African and Middle Eastern regions; dotted line: separation between Middle Eastern and European sources; dash-dotted line: separation between European and other source regions).

Table 5.1.: Source region statistics

Flight region	**FLEXPART**			**SP2**				**Ratio**
	BC mean [ng/m^3]	**BC std [ng/m^3]**	**BC median [ng/m^3]**	**rBC mean [ng/m^3]**	**rBC std [ng/m^3]**	**rBC median [ng/m^3]**	**rBC coated fraction []**	**FP mean / SP2 mean []**
Central Europe	31	93	0.00025	38	64	20	0.17	0.81
Malta	76	135	6	58	58	30	0.08	1.30
Crete	74	89	235	49	56	22	0.10	1.52
Cyprus	96	131	29	92	121	38	0.10	1.04

In the following sub-chapters a closer look at BC source composition of the flight regions Crete and Cyprus is given. Most flights took place in the proximity of Cyprus followed by the Mediterranean near Crete as these regions were of greatest study interest during A-LIFE.

Crete

Figures 5.8 and 5.9 shows similar graphs to Fig. 5.5 and Fig. 5.6 for the flight region Crete instead of all flights. Data for the altitude interval from 7 to 8 km is missing due to less than 20 data points being available in total in that interval. The upper plot shows a decrease of mean BC mass concentration with altitude with the exception of a layer of higher concentrations between 2 and 3 km as well as 6 and 7 km. The lower graph shows a shift in relative BC mass concentration above 4 km from a mixed, predominately European source (South East, South West and North West European) to BC of mainly Tunisian, Algerian and Moroccan origin (although Tunisia makes up a large relative portion as low as 1 km). Local BC emission from Crete can only be seen at very low altitudes below 2 km and make up a small fraction in comparison. Above 4 km, BC originating from North West Africa is visible in the graph with increasing relative concentration with increasing altitude. It must also be highlighted that W Middle Eastern BC, which is the most dominant source region in terms of mass concentration when looking at all flights, only makes up a small fraction of BC mass concentrations here.

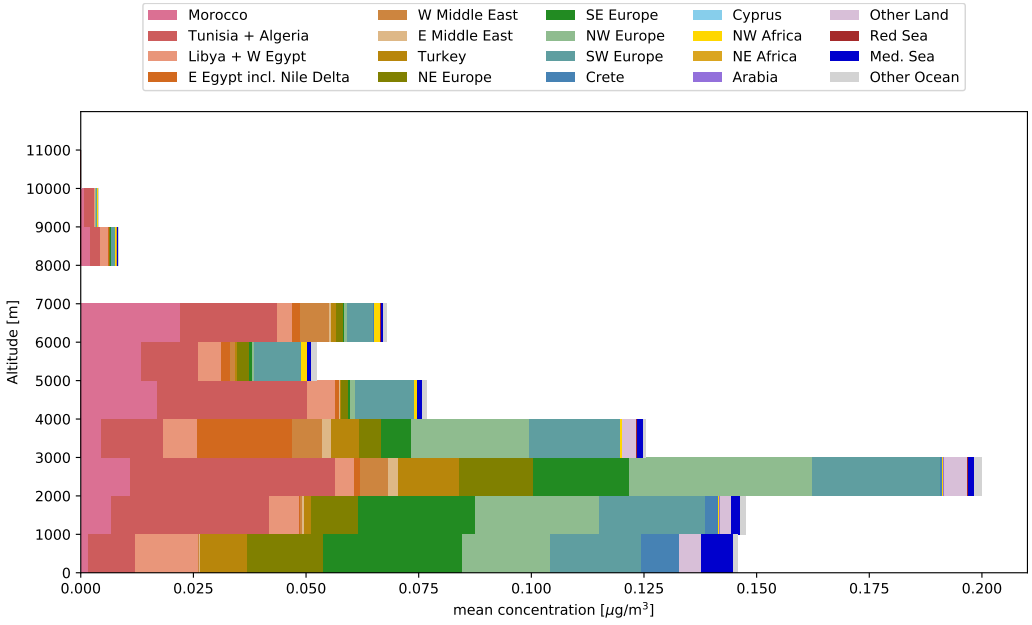

Figure 5.8.: Mean values of FLEXPART simulated BC source region mass concentration as horizontal stacked bar charts dependent on altitude for the flight region Crete.

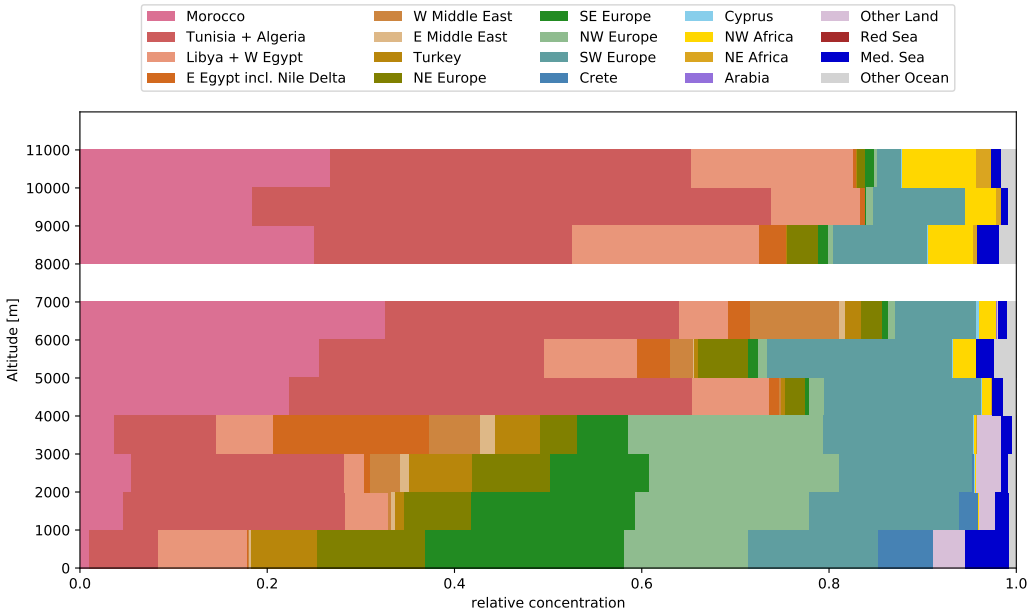

Figure 5.9.: Relative values of FLEXPART simulated BC source region mass concentration as horizontal tacked bar charts dependent on altitude for the flight region Crete.

Figure 5.10 shows the mean horizontal wind direction and its standard deviation as error bars depending on the altitude for the flight region Crete. The shift in dominant BC origin at an altitude of 3-4 km, as shown in Fig. 5.9 above, is likely due to different meteorological conditions and mean wind direction is likely a big factor. Below 4 km altitude the mean wind velocity along the flight routes of the Falcon is generally lower and more variable than from 4 to 10 km altitude, where westerly winds dominate.

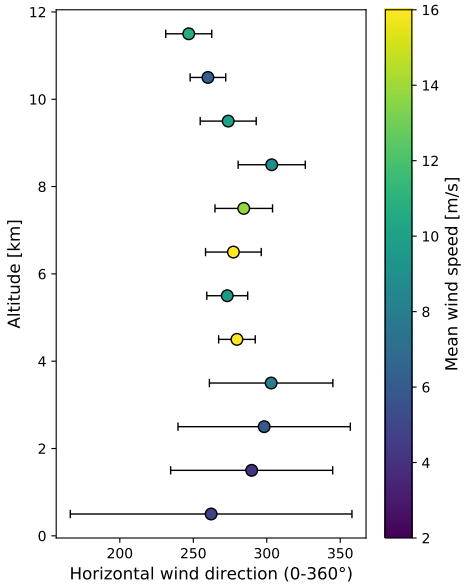

Figure 5.10.: Mean horizontal wind direction profile including color coded mean wind speed for the flight region Crete. Standard deviations are plotted as error bars.

Cyprus

Analogous to Crete, Figures 5.11 and 5.12 show the mean FLEXPART simulated BC mass concentration dependent on altitude in the upper and the relative BC mass concentrations in the lower plot for the flight region Cyprus. For Cyprus mean BC mass decreases with increasing altitude with a clear drop in concentration above 3 km. Below 3 km, the predominant source region is W Middle East shifting to Morocco and Tunisia + Algeria above 4 km. This means that in lower altitudes most BC is transported to Cyprus from the East and in higher altitudes most is transported from the West with the Western source regions being further away. There is little transport from North or South of the flight region. Local BC emissions from Cyprus are, similar to Crete in the previous sub-chapter, only visible in the graph at altitudes below 2 km making up only a very small fraction. Also similar to the results for Crete is the increase of North West African BC above 3 km, with the largest fraction in the highest altitude interval. Surprisingly, North East African BC is not visible in the graphs for the flight regions Cyprus nor Crete. BC originating from E Egypt incl. Nile Delta looks to be more dominant in Cyprus than in Crete and Arabian BC is only visible for Cyprus (although making up only a small relative proportion). There are only few other studies looking at source regions of BC observed over Cyprus. Debevec et al. (2017), who studied source regions of volatile organic compounds at a background site in Cyprus, found that periods when the station was influenced by air masses transported from close Middle Eastern regions (called 'southwest Asia' in the study) BC levels were enhanced compared to air masses from other sources.

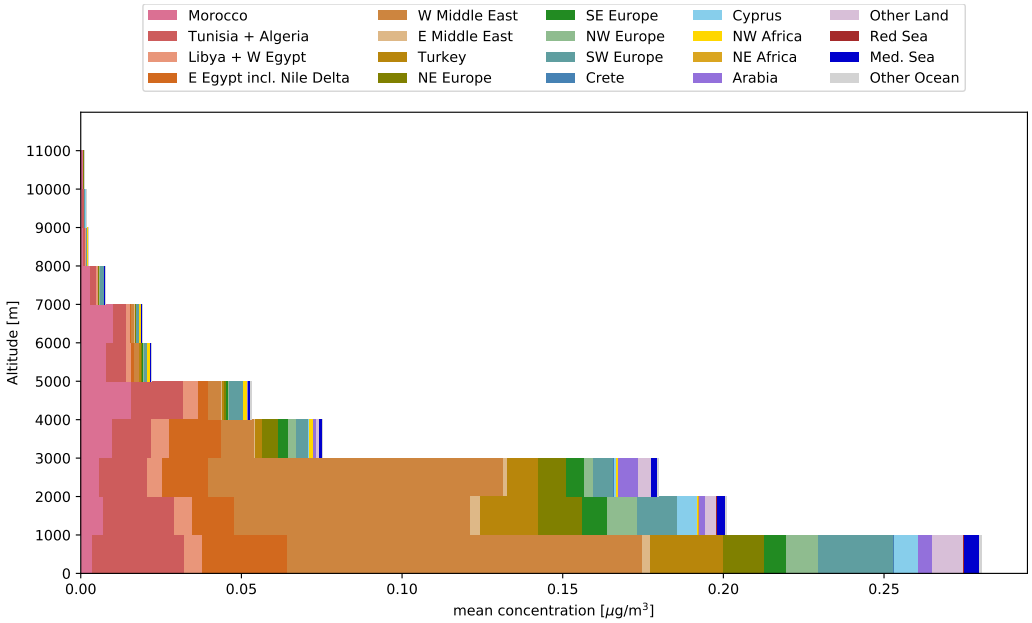

Figure 5.11.: Mean values of FLEXPART simulated BC source region mass concentration as horizontal stacked bar charts dependent on altitude for the flight region Cyprus.

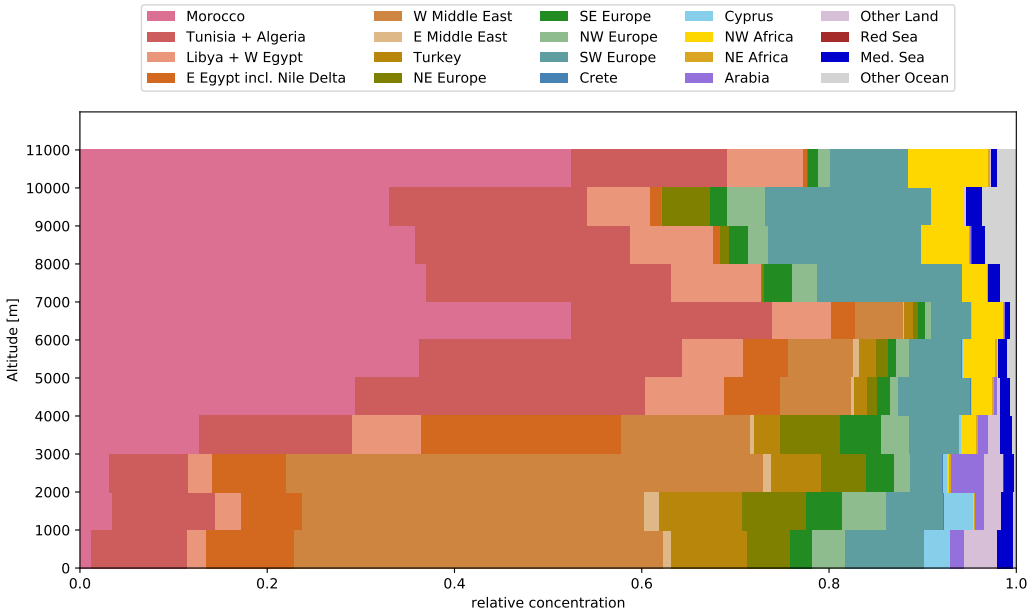

Figure 5.12.: Relative values of FLEXPART simulated BC source region mass concentration as horizontal stacked bar charts dependent on altitude for the flight region Cyprus.

Similar to Crete, the shift in dominant BC origin at altitudes 3-4 km for the flight region Cyprus can very likely be attributed to different meteorological conditions, especially changing mean wind directions. Figure 5.13 shows the mean horizontal wind direction and its standard deviation as error bars depending on the altitude for the flight region Cyprus. Again, the mean wind direction at lower altitudes (below 3 km) is more variable and the mean wind speed is lower. With increasing altitude, the mean wind direction gradually changes from SE to W, which serves as an explanation for the shift from eastern BC origin below 3 km to western BC origin above 4 km.

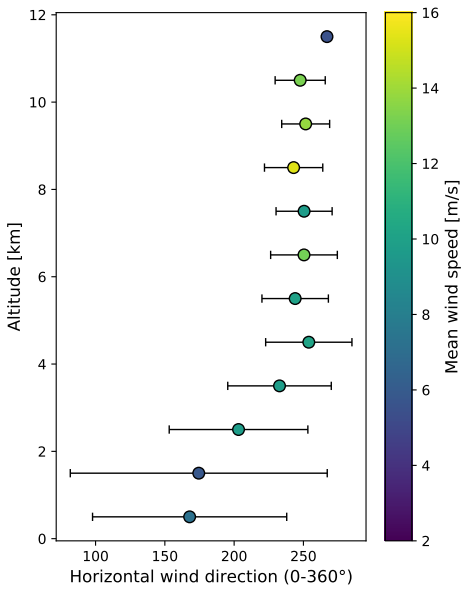

Figure 5.13.: Mean horizontal wind direction profile including color coded mean wind speed for the flight region Cyprus. Standard deviations are plotted as error bars.

5.2. BC source regions in mineral dust layers

As described in Section 3.1.1, A-LIFE flight segments at constant altitude, called sequences, were divided into twelve different aerosol sequence classes plus a background category. In this section a closer look on the origin of BC in the different mineral dust classes according to FLEXPART model calculations is given. Since the classification scheme is based on the ratio of the number concentration of particles larger than 800 nm (measured by the 'Second generation Cloud, Aerosol, and Precipitation Spectrometer with Polarization Detection (CAPS)') to SP2 measured rBC, this does not mean that there is no rBC pollution in sequences classified as clean, just that the amount of pollution relative to non-pollution aerosol is low.

The following section shows source region specific BC mass concentrations for the different aerosol sequence classes in the category mineral dust. In order to be transparent, table 5.2 gives an overview of the number of sequences classified as each class. The more sequences there are per class the more reliable the data is, as the probability of a given sequence being an outlier and not representative of the class is higher the lower the number of sequences per class.

Table 5.2.: Table showing the number of sequences per mineral dust class.

Mineral dust sequence classes	**Flight region**		
	All flights	**Crete**	**Cyprus**
Clean Saharan dust	64	18	35
Moderately polluted Saharan dust	80	17	52
Polluted Saharan dust	2	1	1
Clean Arabian dust	2	0	2
Moderately polluted Arabian dust	8	0	8
Polluted Arabian dust	8	0	8

Looking at source region dependent BC mass concentrations for sequences classified as polluted gives insight in where observed high rBC mass concentrations relative to the amount of aerosol originate from. As can be seen in Figure 5.14 sequences classified as *polluted Arabian dust* have the highest mean FLEXPART simulated BC mass concentration, with 311 ng/m^3 more than twice as high as polluted Saharan with 138 ng/m^3. Moderately polluted Arabian dust has a mean BC concentration of 282 ng/m^3, whereas moderately polluted Saharan dust has a mean BC concentration of 92 ng/m^3. Sequences falling into the clean category show mean BC concentration of 299 ng/m^3 and 66 ng/m^3 for Arabian and Saharan dust. FLEXPART simulated BC concentrations are therefore much higher in Arabian than in Saharan dust layers (almost twice as high for polluted and almost four

times as high for unpolluted sequences). This strengthens the argument made with Fig. 4.7 that during A-LIFE higher amounts of pollution were observed in Arabian than in Saharan dust layers. The fact that rBC mass concentration are similar for the different pollution levels in Arabian dust can be explained by the definition of the pollution criterion. Polluted means high amounts of rBC relative to coarse mode aerosol and clean low amounts of rBC relative to coarse mode aerosol. This leads to the conclusion that in Arabian dust the coarse mode aerosol number concentration must be rather constant with increasing rBC mass concentrations within the different pollution classes, whereas in Saharan dust it increases with increasing rBC mass concentrations, as can be seen in Figure 5.15.
Similar to Fig. 5.7 the black lines in Figure 5.14 separate more general geographical regions (Africa, Middle East, Europe and other) to give a clearer view of BC sources for each class at first sight. Again, only 'close' regions were grouped into the categories Africa, Middle East and Europe, whereas regions farther away as well as sea regions were put into 'other' due to their low contributions to BC mass. BC in Saharan dust layers is predominately of African origin with BC in clean Saharan dust stemming mainly from Moroccan, Algerian and Tunisian sources. In moderately polluted Saharan dust dominant BC sources are Tunisia + Algeria and E Egypt incl. Nile Delta, similar to polluted Saharan dust. The fraction of BC originating from European regions, especially SW Europe, is increasing with increasing pollution level. This is also the case for BC from E Egypt incl. Nile Delta, but this information must also be interpreted in the context that there are only 2 sequences in total in this class. For Arabian dust the composition of BC mass in terms of source region looks similar for clean, moderately polluted and polluted sequences. W Middle East is clearly the most dominant BC source for Arabian dust in general, with Middle Eastern sources making up more than three fourths for all pollution levels. It is notable that Arabian BC (dark purple), which otherwise shows very little mass concentrations, can be seen in Arabian dust, especially in polluted Arabian dust. The fraction of BC originating from European sources is decreasing with increasing amount of pollution in Arabian dust, contrarily to Saharan dust. Also, BC from E Egypt incl. Nile Delta has slightly higher mass concentrations in polluted than in clean and moderately polluted Arabian dust.

From the figure, it seems that BC in Saharan dust stems from different source regions depending on the level of pollution, whereas the source regions of BC in Arabian dust are very similar regardless of pollution. But, given the fact that there are many more Saharan dust than Arabian dust sequences, this could just be by chance.

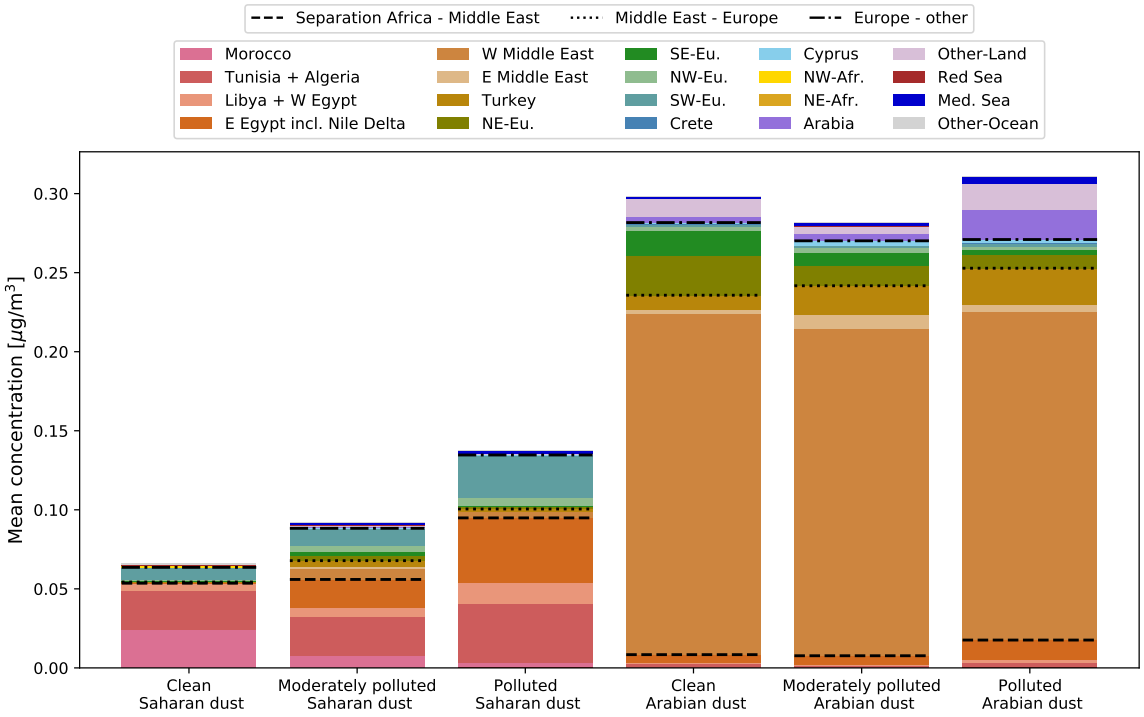

Figure 5.14.: Mean values of FLEXPART simulated BC source region mass concentration as stacked bar charts for the sequence classes: clean Saharan dust, moderately polluted Saharan dust, polluted Saharan dust as well as clean Arabian dust, moderately polluted Arabian dust and polluted Arabian dust.

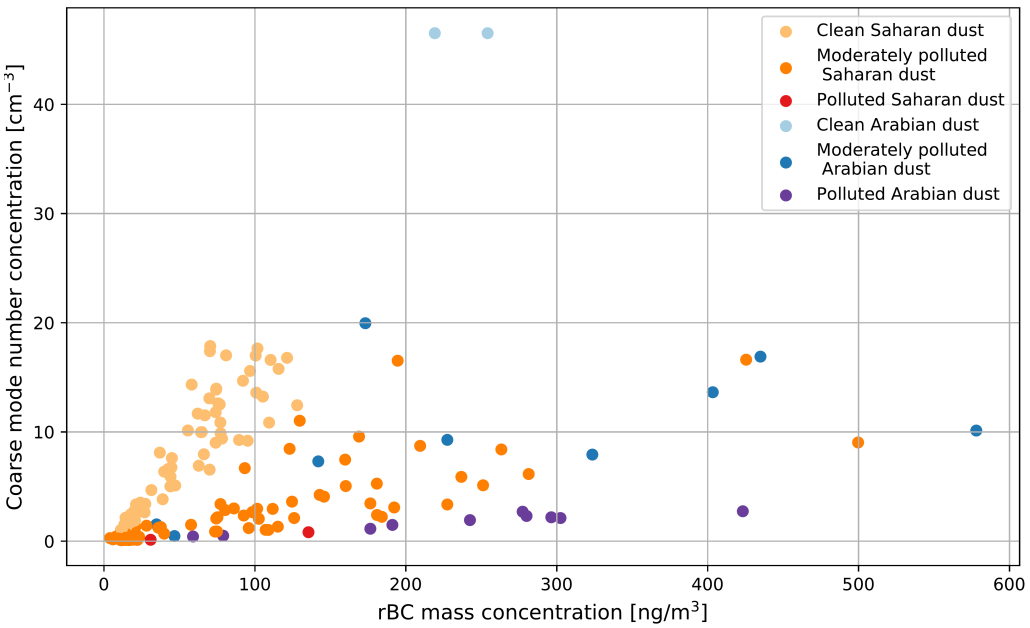

Figure 5.15.: Number concentration of coarse mode aerosol per cubic centimeter depended on rBC mass concentration in nanogram per cubic meter for the different mineral dust sequence classes.

Since most of the sequences classified as mineral dust are of Saharan origin, a closer look at the dependence of BC source region composition in Saharan dust layers of different pollution level on the flight region gives further insight on BC transport. Figures 5.16 and 5.17 show the mean FLEXPART simulated BC concentrations in Saharan dust for the flight regions Crete and Cyprus, respectively. The source region composition of Saharan dust looks very similar, but the mean BC mass concentrations are much lower in Cyprus than in Crete, indicating that higher number concentrations of dust aerosol were measured in Crete since the pollution criteria is based on the ratio of the amount of coarse particles to the rBC mass. In moderately polluted Saharan dust layers above Crete, the BC origin is mixed with African, Middle Eastern and European sources taking up almost equal fractions, whereas above Cyprus BC is mainly of African origin with a high fraction stemming from E Egypt incl. Nile Delta region. The polluted Saharan dust cases show the biggest difference in terms of BC source regions between flights above Crete and Cyprus. There is each only 1 sequence falling into this class, though. In both cases the African BC fraction is the most dominant with most of BC originating from E Egypt incl. Nile Delta region for the flight region Crete. For Cyprus, Tunisia + Algeria is the most dominant BC source region, but the European (especially SW-European) BC fraction is prominent as well.

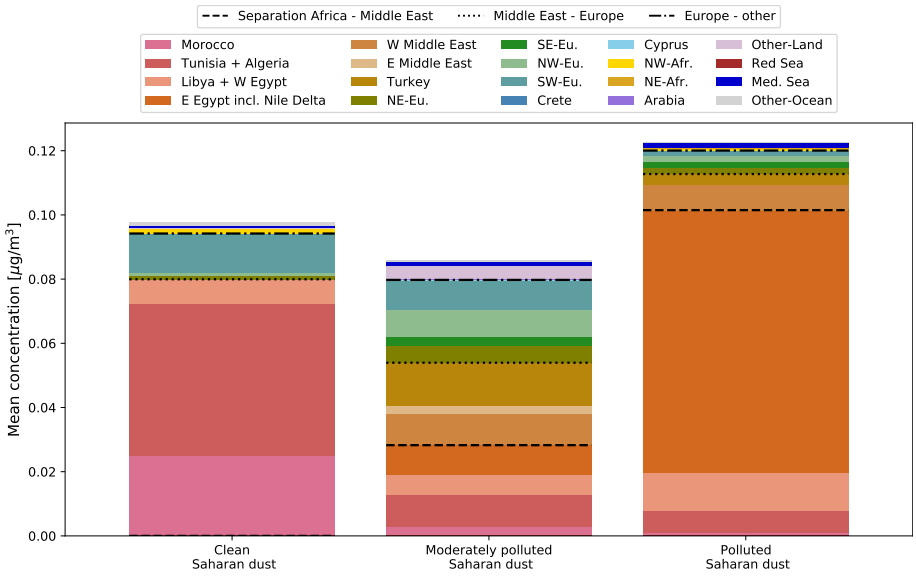

Figure 5.16.: Mean values of FLEXPART simulated BC source region mass concentration as stacked bar charts for the flight region Crete for the sequence classes: clean Saharan dust, moderately polluted Saharan dust, polluted Saharan dust.

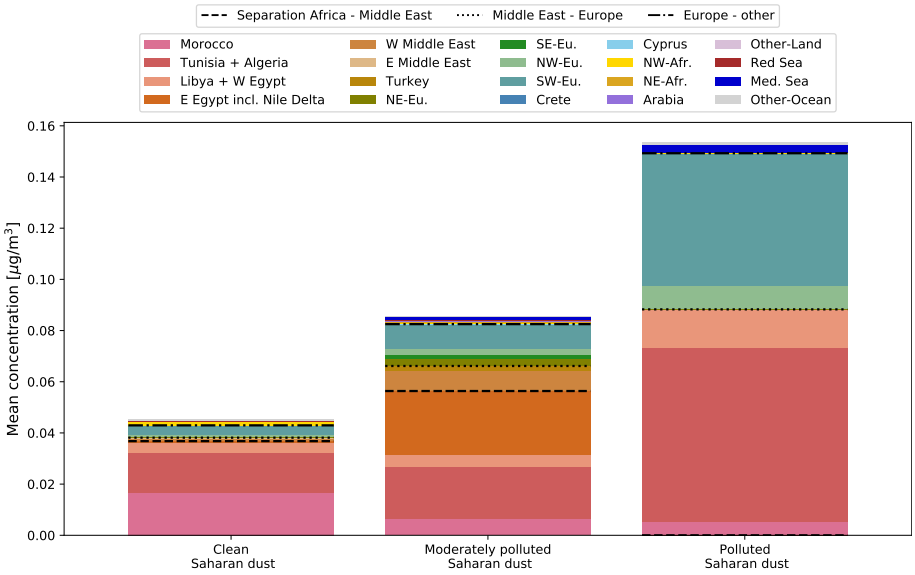

Figure 5.17.: Mean values of FLEXPART simulated BC source region mass concentration as stacked bar charts for the flight region Cyprus for the sequence classes: clean Saharan dust, moderately polluted Saharan dust, polluted Saharan dust.

For completeness, Figure 5.18 shows the composition in terms of FLEXPART simulated BC source regions for the sequence classes that don't fall into the mineral dust criteria: clean mixtures with enhanced coarse mode, moderately polluted mixtures with enhanced coarse mode, polluted mixtures with enhanced coarse mode, moderately polluted mixtures with low coarse mode contribution and polluted mixtures with low coarse mode contribution (there are no sequences classified as clean mixtures with low coarse mode contribution). The BC mean concentrations for moderately polluted mixtures with low coarse mode contribution are multiplied by the factor 10 in order to make the source region distribution more visible. The European BC fraction is the most prominent for all sequence classes shown in the figure. Mean FLEXPART simulated BC concentrations are very low (< 0.03 ng/m^3) for mixtures with low coarse mode contribution. For mixtures with enhanced coarse mode, mean BC mass concentrations are higher with increasing levels of pollution. Interestingly, BC originating from the Mediterranean Sea (dark blue) can only be seen in very low mass concentrations in moderately polluted and polluted mixtures with enhanced coarse mode. High coarse mode concentrations with a low fraction of mineral dust aerosol could indicate a higher number of sea salt aerosol, which is also commonly found in the coarse mode. The fact that BC originating from water source regions only has very low mass concentrations could mean that shipping emissions only played a very minor role in the observed rBC mass concentrations.

To summarize, Figure 5.19 shows the relative BC source region mass concentrations for all sequence classes. As was stated above, there are no sequences classified as clean mixtures with low coarse mode contribution, which is why only 11 classes are plotted.

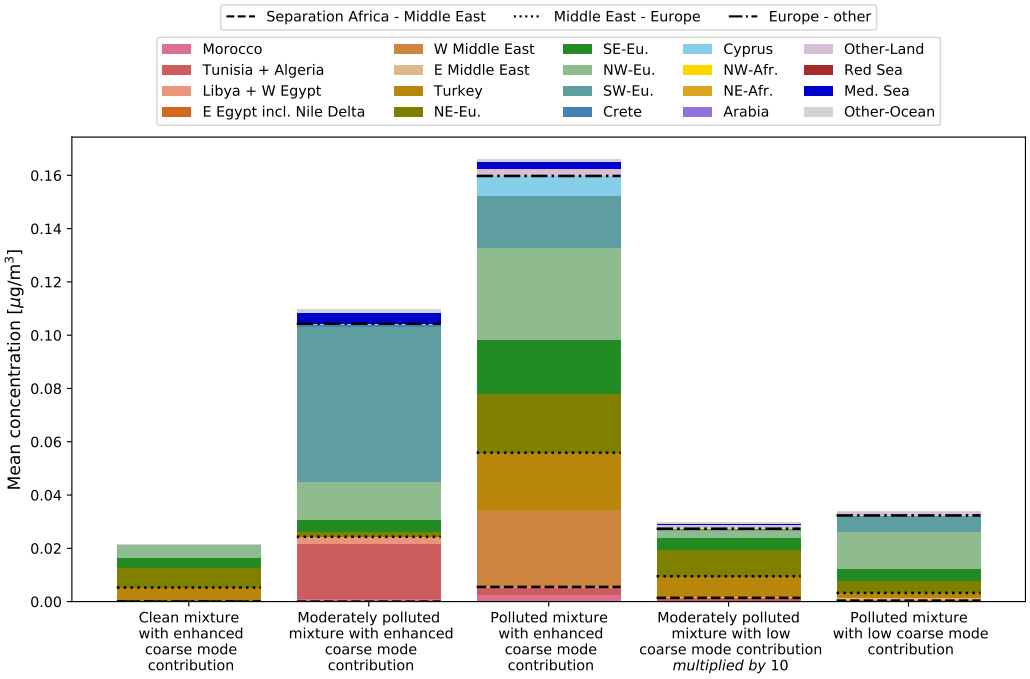

Figure 5.18.: Mean values of FLEXPART simulated BC source region mass concentration as stacked bar charts for all flights for the sequence classes: clean mixtures with enhanced coarse mode, moderately polluted mixtures with enhanced coarse mode, polluted mixtures with enhanced coarse mode, moderately polluted mixtures with low coarse mode contribution (multiplied by 10) and polluted mixtures with low coarse mode contribution. The BC mean concentrations for moderately polluted mixtures with low coarse mode contribution are multiplied by the factor 10 in order to make the source region distribution more visible.

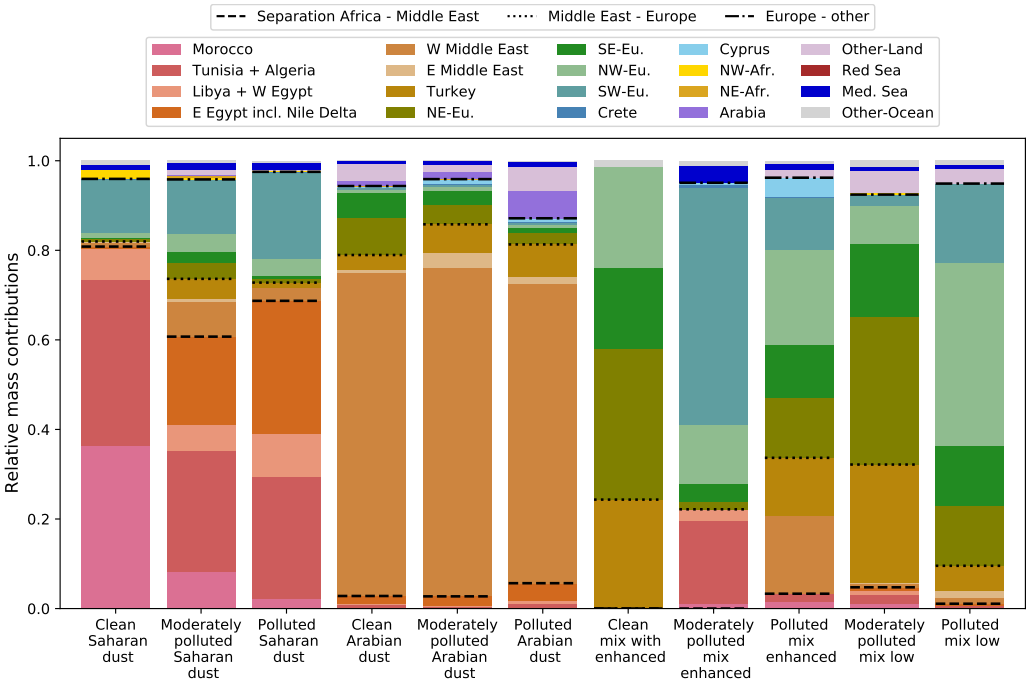

Figure 5.19.: Relative values of FLEXPART simulated BC source region mass concentration as stacked bar charts for all flights for all sequence classes.

6. Conclusion

The A-LIFE aircraft field campaign, which took place in April 2017, presented the opportunity to investigate properties of absorbing aerosol layers over the Eastern Mediterranean. This thesis focuses on SP2 rBC measurements obtained during A-LIFE and combines observational data with FLEXPART modelled BC concentrations to determine BC source regions.[1] BC has the highest light absorption efficiency of all atmospheric aerosols and plays an import role in the climate system.

At low altitudes (below 2 km), rBC mass concentrations were observed to be between 7 and 717 ng/m^3 with a mean of 212 ng/m^3. This is in agreement with data collected during the ChArMEx/ADRIMED campaign conducted in the western Mediterranean region in summer 2013: Mallet et al. (2016) report rBC mass concentrations between 20 and 690 ng/m^3 close to the surface. Vertical profiles of both measured and modelled A-LIFE data show a decrease of measured rBC and modelled BC mass concentrations with increasing altitude averaged over all flights with measured median rBC concentration ranging from 12 to 223 ng/m^3. In the measurement data a slight increase of median rBC mass concentration as well as first and third quantile concentrations can be seen at high altitudes (above 9 km), whereas this is not the case for the modelled BC mass concentrations. Since backward trajectories were only calculated 12 days back, this could indicate layers of aged BC which were not covered by the model. At high altitudes BC has longer atmospheric lifetimes because of less wet deposition than at low altitudes (Bond et al. 2013). Vertical profiles of observed rBC mass concentrations above central Europe fit very well to similar data published in Schwarz et al. (2017) at altitudes above 5 km. At lower altitudes (below 5 km) lower mass concentrations were observed during A-LIFE. Very likely, seasonal variability plays a role here, since A-LIFE took place in early spring 2017 and the Schwarz et al. (2017) data was collected in early autumn 2011. Further, BC mass concentration above central Europe are decreasing over time. Sun et al. (2020) for example show an annual decrease of BC mass concentration between 1.7 and 13.1 % for the time period 2008 to 2019 at different observational sites in Germany.

In general, rBC median mass concentration at higher altitudes (above 6km) were higher in the region around Cyprus, which is also reflected in the FLEXPART simulated BC

[1] As was described in the introduction (chapter 1), the term refractory black carbon (rBC) used to describe black carbon measured specifically by a *Single Particle Soot Photometer (SP2)* by laser-induced incandescence as recommended in Petzold et al. (2013). BC refers to black carbon in the context of no specific measurement device and is hence used to describe the FLEXPART model output.

concentration at the altitude interval 6 to 7 km. According to the model data, the highest mean BC concentrations for this region are between 2 and 3 km altitude, whereas the measurement data shows the highest median concentration in the lowest altitude range between 0 to 1 km and the second highest between 2 and 3 km. Median rBC particle coated fraction values for all flights were observed to be below 15% and therefore lower than comparable results in the literature (e.g. McMeeking et al. (2011)). Vertical profiles of the rBC coated fraction show higher coated fractions above central Europe than over the other flight regions. Above Cyprus there was a slight increase of coated fraction at high altitude ranges, whereas above Crete there was a rapid increase at altitudes above 8 km up to 24% between 10 and 11 km. This is an indication for higher concentrations of aged BC.

Arabian dust layers were observed at lower altitudes than Saharan dust layers, which is rather typical for the Eastern Mediterranean, as earlier lidar studies (e.g. Engelmann et al. (2016)) have shown. SP2 measured rBC as well as FLEXPART modelled BC mass concentrations are generally higher in Arabian than in Saharan dust (mean rBC concentrations in Saharan dust: 72 ng/m^3; Arabian dust: 246 ng/m^3). FLEXPART simulated BC mass concentrations show an increase with increasing pollution in Saharan, but not in Arabian dust.

FLEXPART simulated BC source region mass concentrations show that most of the observed BC is of north African and south west Asian origin. In general, north African and south west Asian BC can be found at higher altitudes and at higher mass concentrations than European BC. Especially interesting is the shift of dominant BC origin for flights above central Europe from European to north African and south west Asian source regions at altitudes above 4 km.

Mean FLEXPART simulated BC concentrations are lowest for the flight region central Europe (31 ng/m^3) and highest for Cyprus (96 ng/m^3). Crete and Malta have similar mean BC concentrations of 76 ng/m^3 and 74 ng/m^3, respectively. According to FLEXPART, BC above central Europe is mainly of European origin with a small fraction stemming from African sources. This fits well with the finding that African BC was observed at higher altitudes and that rBC concentrations were decreasing with increasing altitude. For the regions Malta and Crete BC originates from African and European sources with the first being more dominant for Malta and the latter more dominant for Crete. A small fraction of BC in the flight region Crete is of Middle Eastern origin. BC in the vicinity of Cyprus is of mixed African, Middle Eastern and European origin with close middle Eastern sources making up the largest fraction.

Looking at the vertical distribution of BC source region mass concentrations, there is a shift in dominant origin for both Crete and Cyprus at altitudes above 3-4 km. For the flight region Crete, BC mainly originates from European source regions below 3 km whereas

BC above Cyprus is predominately of Middle Eastern origin indicating BC transport from close Eastern regions. Above 4 km over Crete as well as Cyprus relative FLEXPART simulated BC mass concentrations show that BC is dominantly of African origin (Crete: 75%, Cyprus: 73%), stemming especially from north western African regions. Relative mass concentrations from north eastern African regions make up a much smaller fraction indicating BC transport to Crete and Cyprus from western region in higher altitudes but little from southern regions. Local BC emission stemming from Crete and Cyprus themselves only contribute notably to total BC mass concentrations at altitudes below 2 km, albeit in low relative concentrations with 4% for Crete and 3% for Cyprus. BC was transported to Cyprus from close eastern regions at low altitudes (below 3 km) and from further away western regions at higher altitudes (above 4 km), whereas there was little transport from north / south. Interestingly this shift at altitudes of 3-4 km cannot be seen clearly in coated fraction vertical profiles for the region Cyprus. BC transported from further away source regions generally indicates older BC populations and as was explained in the introduction (chapter 1), BC coatings are a sign of aged BC. There is an increase of coated fraction above 3 km, but it is not as abrupt as one would expect from the model data. But, depending on wind conditions and meteorological conditions in general, it must not be necessarily the case that air masses from further away regions take proportionally longer to be transported to a certain location than air masses stemming from closer regions. Flaounas et al. (2015), for example, show that in April (when the A-LIFE flights above Cyprus took place) extreme Saharan dust transport events over the Mediterranean region peak due to high cyclonic activity. Cyclones are capable of transporting dust but also other aerosol types like BC over large distances in rather short periods of time. (e.g. Raut et al. (2017))

In Saharan dust layers, African regions are the most prominent origin for BC with the fraction of BC stemming from the Nile Delta as well as SW Europe increasing with increasing pollution. Abdelkader et al. (2015) describe a dust event where Saharan dust was transported to Cyprus due to a high-pressure system over the Sahara and a low-pressure system over Cyprus, which enhanced transport of air pollution from central and southern Europe. Similar weather conditions occurred around the 17th of April 2017 [2] and during the next A-LIFE flights (on the 19th of April) moderately polluted Saharan dust layers were observed.

Middle Eastern BC makes up more than three fourths of BC in Arabian dust (in terms of mean mass concentration) and with increasing pollution the (East) European BC fraction is decreasing. BC in mixtures with enhanced as well as mixtures with low coarse mode contributions is mainly of European origin. BC stemming from sea source regions shows only minor contributions to mean mass concentrations in mixtures with enhanced coarse mode, possibly indicating low ship emissions.

[2] according to ZAMG weather maps:
https://www.zamg.ac.at/cms/de/wetter/wetterkarte?tag=17&monat=04&jahr=2017&utc=06
last called: 01.02.21
.

These results show the highly complex situation of BC and its source regions in the Eastern Mediterranean. In future studies, the low values of rBC particle coated fraction should be investigated further. Calculating coating thickness time series could lead to more insight on the history and sources of the observed rBC. In addition, future work should focus on the discrepancy of measured rBC and modelled BC mass concentration at high altitudes by e.g. using FLEXPART to calculate trajectories further than 12 days backward.

Bibliography

A-LIFE webpage (2017), 'A-life project webpage by the aerosol physics environmental physics department of the university of vienna'.
URL: *https://www.a-life.at/*

Abdelkader, M., Metzger, S., Mamouri, R. E., Astitha, M., Barrie, L., Levin, Z. & Lelieveld, J. (2015), 'Dust–air pollution dynamics over the eastern mediterranean', *Atmospheric Chemistry and Physics* **15**, 9173–9189.

Adachi, K., Chung, S. H., Friedrich, H. & Buseck, P. R. (2007), 'Fractal parameters of individual soot particles determined using electron tomography: Implications for optical properties', *J. Geophys. Res.* **112**, D14202.

AMAP (2015). AMAP Assesment 2015: Black carbon and ozone as Arctic climate forcers. Arctic Monitoring and Assessment Programme (AMAP), Oslo, Norway. vii + 116 pp.

Bohren, C. F. & Huffman, D. (2004), *Absorption and Scattering of Light by Small Particles*, second edn, Wiley-VCH Verlag GmbH KGaA.

Bond, T. C. & Bergstrom, R. W. (2006), 'Light absorption by carbonaceous particles: An investigative review', *Aerosol Science and Technology* **40:1**, 27–67.

Bond, T. C., Doherty, S. J., Fahey, D. W., Forster, P. M., Berntsen, T., DeAngelo, B. J., Flanner, M. G., Ghan, S., Kärcher, B., Koch, D., Kinne, S., Kondo, Y., Quinn, P. K., Sarofim, M. C., Schultz, M. G., Schulz, M., Venkataraman, C., Zhang, H., Zhang, S., Bellouin, N., Guttikunda, S. K., Hopke, P. K., Jacobson, M. Z., Kaiser, J. W., Klimont, Z., Lohmann, U., Schwarz, J. P., Shindell, D., Storelvmo, T., Warren, S. G., & Zender, C. S. (2013), 'Bounding the role of black carbon in the climate system: A scientific assessment', *J. Geophys. Res. Atmos.* **118**, 5380–5552.

Brown, W. K. & Wohletz, K. H. (1995), 'Derivation of the weibull distribution based on physical principles and its connection to the rosin–rammler and lognormal distributions', *Journal of Applied Physics* **78**, 2758–2763.

CAMS (n.d.), 'Copernicus atmosphere monitoring service webpage'.
URL: *https://atmosphere.copernicus.eu/*

Dahlkötter, F. (2013), 'Airborne observations of black carbon aerosol layers at mid-latitudes', *Disseration, Deutsches Zentrum für Luft- und Raumfahrt, Institut für Physik der Atmosphäre* .

Debevec, C., Sauvage, S., Gros, V., Sciare, J., Pikridas, M., Stavroulas, I., Salameh, T., Leonardis, T., Gaudion, V., Depelchin, L., Fronval, I., Sarda-Esteve, R., Baisnée, D., Bonsang, B., Savvides, C., Vrekoussis, M. & Locoge, N. (2017), 'Origin and variability in volatile organic compounds observed at an eastern mediterranean background site (cyprus)', *Atmospheric Chemistry and Physics* **17**, 11355–11388.

Eckhardt, S., Stohl, A., Wernli, H., James, P., Forster, C. & Spichtinger, N. (2004), 'A 15-year climatology of warm conveyor belts', *Journal of climate* **17**(1), 218–237.

Engelmann, R., Ansmann, A., Bühl, J., Heese, B., Baars, H., Althausen, D., Marinou, E., Amiridis, V., Mamouri, R. E. & Vrekoussis, M. (2016), 'Observation of arabian and saharan dust in cyprus with a new generation of the smart raman lidar polly', *EPJ Web of Conferences* **119**, 27003.

Flaounas, E., Kotroni, V., Lagouvardos, K., Kazadzis, S., Gkikas, A. & Hatzianastassiou, N. (2015), 'Cyclone contribution to dust transport over the mediterranean region', *Royal Meteorological Society* **16**, 473–478.

Fung, K. (1990), 'Particulate carbon speciation by mno2 oxidation', *Aerosol Science and Technology* **12:1**, 122–127.

Gao, R. S., Schwarz, J. P., Kelly, K. K., Fahey, D. W., Watts, L. A., Thompson, T. L., Spackman, J. R., Slowik, J. G., Cross, E. S., Han, J. H., Davidovits, P., Onasch, T. B. & Worsnop, D. R. (2007), 'A novel method for estimating light-scattering properties of soot aerosols using a modified single-particle soot photometer', *Aerosol Science and Technology* **41**, 125–135.

Hatch, T. & Choate, S. P. (1908), 'Statistical description of the size properties of non uniform particulate substances', *Journal of the Franklin Institute* **207**, 369–387.

Heimerl, K. (2011), 'Characterisation of the dlr single particle soot photometer and its sensitivity to different absorbing aerosol types', *Diplom, Fakultät für Physik, Ludwig-Maximilians-Universität München* .

Heimerl, K. (2018), 'Characterizing north american biomass burning layers in the free troposphere with a single particle soot photometer', *Dissertation, Fakultät für Physik, Ludwig-Maximilians-Universität München* .

Hinds, W. C. (2012), *Aerosol Technology: Properties, Behavior, and Measurement of Airborne Particles*, second edn, Wiley-Interscience.

Holton, J. R. (2004), *An Introduction to Dynamic Meteorology*, forth edn, Elsevier Science Technology.

Huntrieser, H., Lichtenstern, M., Scheibe, M., Aufmhoff, H., Schlager, H., Pucik, T., Minikin1, A., Weinzierl, B., Heimerl, K., Pollack, I. B., Peischl, J., Ryerson, T. B.,

Weinheimer, A. J., Honomichl, S., Ridley, B. A., Biggerstaff, M. I., Betten, D. P., Hair, J. W., Butler, C. F., Schwartz, M. J. & Barth, M. C. (2016), 'Injection of lightning-produced nox, water vapor, wildfire emissions, and stratospheric air to the ut/ls as observed from dc3 measurements', *J. Geophys. Res. Atmos* **121**, 6638–6668.

IPCC (2013). IPCC: Climate Change 2013: The Physical Science Basis. Contribution of Working Group I to the Fifth Assessment Report of the Intergovernmental Panel on Climate Change, edited by: Stocker, T. F., D. Qin, G.-K. Plattner, M. Tignor, S.K. Allen, J. Boschung, A. Nauels, Y. Xia, V. Bex and P.M. Midgley, Cambridge University Press, Cambridge, United Kingdom and New York, NY, USA, 1535 pp., 2013.

Jaenicke, R. (1980), 'Atmospheric aerosols and global climate', *Journal of Aerosol Science* **11**, 577-588.

Koch, D., Bauer, S. E., Genio, A. D., Faluvegi, G., Mcconnell, J. R., Menon, S., Miller, R. L., Rind, D., Ruedy, R., Schmidt, G. A. & Shindell, D. (2011), 'Coupled aerosol-chemistry–climate twentieth-century transient model investigation: Trends in short-lived species and climate responses', *JOURNAL OF CLIMATE* **24**, 2693–2714.

Laborde, M., Mertes, P., Zieger, P., Dommen, J., Baltensperger, U. & Gysel, M. (2012b), 'Sensitivity of the single particle soot photometer to different black carbon types', *Atmospheric measurement techniques* **5**, 1031–1043.

Laborde, M., Schnaiter, M., Linke, C., Saathoff, H., Naumann, K.-H., Möhler, O., Berlenz, S., Wagner, U., Taylor, J. W., Liu, D., Flynn, M., Allan, J. D., Coe, H., Heimerl, K., Dahlkötter, F., Weinzierl, B., Wollny, A. G., Zanatta, M., Cozic, J., Laj, P., Hitzenberger, R., Schwarz, J. P. & Gysel, M. (2012a), 'Single particle soot photometer intercomparison at the aida chamber', *Atmospheric Measurement Techniques* **5**, 3077–3097.

Lund, M. T., Berntsen, T. K. & Samset, B. H. (2017), 'Sensitivity of black carbon concentrations and climate impact to aging and scavenging in osloctm2–m7', *Atmospheric Chemistry and Physics* **17**, 6003–6022.

Mahrt, F., Marcolli, C., David, R. O., Grönquist, P., Eszter, Meier, B., Lohmann, U. & Kanji, Z. A. (2018), 'Ice nucleation abilities of soot particles determined with the horizontal ice nucleation chamber', *Atmospheric Chemistry and Physics* **18**, 13363–13392.

Mallet, M., Dulac, F., Formenti, P., Nabat, P., J. Sciare and, G. R., Pelon, J., Ancellet, G., Tanré, D., Parol, F., Denjean, C., Brogniez, G., di Sarra, A., Alados-Arboledas, L., Arndt, J., Auriol, F., Blarel, L., Bourrianne, T., Chazette, P., Chevaillier, S., Claeys, M., D'Anna, B., Derimian, Y., Desboeufs, K., Iorio, T. D., Doussin, J.-F., Durand, P., Féron, A., Freney, E., Gaimoz, C., Goloub, P., Gómez-Amo, J. L., Granados-Muñoz, M. J., Grand, N., Hamonou, E., Jankowiak, I., Jeannot, M., Léon, J.-F., Maillé, M., Mailler, S., Meloni, D., Menut, L., Momboisse, G., Nicolas, J., Podvin, T., Pont, V., Rea, G., Renard, J.-B., Roblou, L., Schepanski, K., Schwarzenboeck, A., Sellegri, K.,

Sicard, M., Solmon, F., Somot, S., Torres, B., Totems, J., Triquet, S., Verdier, N., Verwaerde, C., Waquet, F., Wenger, J., & Zapf, P. (2016), 'Overview of the chemistry-aerosol mediterranean experiment/aerosol direct radiative forcing on the mediterranean climate (charmex/adrimed) summer 2013 campaign', *Atmospheric Chemistry and Physics* **16**, 455–504.

McMeeking, G. R., Morgan, W. T., Flynn, M., Highwood, E. J., Turnbull, K., Haywood, J. & Coe, H. (2011), 'Black carbon aerosol mixing state, organic aerosols and aerosol optical properties over the united kingdom', *Atmospheric Chemistry and Physics* **11**(17), 9037–9052.

Medalia, A. I. & Iieckman, F. A. (1969), 'Morphology of aggregates - ii. size and shape factors of carbon black aggregates from electron microscopy', *Pergmon Press.* **7**, 567–582.

Mie, G. (1908), 'Beiträge zur optik trüber medien, speziell kolloidaler metallösungen', *Annalen der Physik* **330**, 377–445.

Moteki, N. & Kondo, Y. (2007), 'Effects of mixing state on black carbon measurements by laser-induced incandescence', *Aerosol Science and Technology* **41:4**, 398–417.

Motos, G., Schmale, J., Corbin, J. C., Zanatta, M., Baltensperger, U. & Gysel-Beer, M. (2019), 'Droplet activation behaviour of atmospheric black carbon particles in fog as a function of their size and mixing state', *Atmospheric Chemistry and Physics* **19**, 2183–2207.

Park, R. J., Jacob, D. J., Palmer, P. I., Clarke, A. D., Weber, R. J., Zondlo, M. A., Eisele, F. L., Bandy, A. R., Thornton, D. C., Sachse, G. W. & Bond, T. C. (2005), 'Export efficiency of black carbon aerosol in continental outflow: Global implications', *Journal of Geophysical Research - Atmospheres* **110**(D11), D11205–n/a.

Peterson, D. A., Hyer, E. J., Campbell, J. R., Fromm, M. D., Hair, J. W., Butler, C. F. & Fenn, M. A. (2012), 'Implications for predicting extreme fire spread, pyroconvection, and smoke emissions', *Bulletin of the American Meteorological Society* **96**(2), 229–248.

Petzold, A., Dopelheuer, A., Brock, C. & Schroder, F. (1999), 'In situ observations and model calculations of black carbon emission by aircraft at cruise altitude', *J. Geophys. Res. Atmos* **104**, 22171–22181.

Petzold, A., Ogren, J. A., Fiebig, M., Laj, P., Li, S.-M., Baltensperger, U., Holzer-Popp, T., Kinne, S., Pappalardo, G., Sugimoto, N., Wehrli, C., Wiedensohler, A., & Zhang, X.-Y. (2013), 'Recommendations for reporting "black carbon" measurements', *Atmospheric Chemistry and Physics* **13**, 8365–8379.

Ramanathan, V. & Carmichael, G. (2008), 'Global and regional climate changes due to black carbon', *Nature Geoscience* **1**, 221–227.

Ramanathan, V. & Feng, Y. (2009), 'Air pollution, greenhouse gases and climate change: Global and regional perspectives', *Atmospheric Environment* **43**, 37–50.

Raut, J. C., Marelle, L., Fast, J. D., Thomas, J. L., Weinzierl, B., Law, K. S., Berg, L. K., Roiger, A., Easter, R. C., Heimerl, K., Onishi, T., Delanoë, J. & Schlager, H. (2017), 'Cross-polar transport and scavenging of siberian aerosols containing black carbon during the 2012 access summer campaign', *Atmospheric Chemistry and Physics* **17**, 10969–10995.

Roede, W. (2011), *Physik unserer Umwelt : die Atmosphäre*, forth edn, Springer.

Schwarz, J., Gao, R., Fahey, D. W., Thomson, D. S., Watts, L. A., Wilson, J. C., Reeves, J., Darbeheshti, M., Baumgardner, D. G., Kok, G. L., Chung, S. H., Schulz, M., Hendricks, J., Lauer, A., Karcher, B., Slowik, J. G., Rosenlof, K. H., Thompson, T. L., Langford, A. O., Loewenstein, M. & Aikin, K. C. (2006), 'Single-particle measurements of midlatitude black carbon and light-scattering aerosols from the boundary layer to the lower stratosphere', *J. Geophys. Res. Atmos.* **111**.

Schwarz, J. P., Gao, R. S., Spackman, J. R., Watts, L. A., Thomson, D. S., Fahey, D. W., Ryerson, T. B., Peischl, J., Holloway, J. S., Trainer, M., Frost, G. J., Baynard, T., , Lack, D. A., de Gouw, J. A., Warneke, C. & Negro, L. A. D. (2008), 'Measurement of the mixing state, mass, and optical size of individual black carbon particles in urban and biomass burning emissions', *Geophys. Res. Lett.* **35**, L13810.

Schwarz, J. P., Samset, B. H., Perring, A. E., Spackman, J. R., Gao, R. S., Stier, P., Schulz, M., Moore, F. L., Ray, E. A. & Fahey, D. W. (2013), 'Global-scale seasonally resolved black carbon vertical profiles over the pacific', *Geophys. Res. Lett.* **40**, 5542–5547.

Schwarz, J. P., Spackman, J. R., Gao, R. S., Perring, A. E., Cross, E., Onasch, T. B., Ahern, A., Wrobel, W., Davidovits, P., Olfert, J., Dubey, M. K., Mazzoleni, C. & Fahey, D. W. (2010), 'The detection efficiency of the single particle soot photometer', *Aerosol science and technology* **44**(8), 612–628.

Schwarz, J. P., Weinzierl, B., Samset, B. H., Dollner, M., Heimerl, K., Markovic, M. Z., Perring, A. E. & Ziemba, L. (2017), 'Aircraft measurements of black carbon vertical profiles show upper tropospheric variability and stability', *Geophys. Res. Lett.* **44**.

Seinfeld, J. H. & Pandis, S. (2006), *Atmospheric chemistry and physics : from air pollution to climate change*, second edn, John Wiley Sons.

Shine, K. P. (2000), 'Radiative forcing of climate change', *Space Science Reviews* **94**, 363–373.

Singh, R. P., Kumar, S. & Singh, A. K. (2018), 'Elevated black carbon concentrations and atmospheric pollution around singrauli coal-fired thermal power plants (india) using ground and satellite data', *International Journal of Environmental Research and Public Health* **15**, 2472.

Stohl, A., Forster1, C., Frank, A., Seibert, P., & Wotawa, G. (2005), 'Technical note: The lagrangian particle dispersion model flexpart version 6.2', *Atmos. Chem. Phys.* **5**, 2461–2474.

Subramanian, R., Kok, G. L., Baumgardner, D., Clarke, A., Shinozuka, Y., Campos, T. L., Heizer, C. G., Stephens, B. B., de Foy, B., Voss, P. B. & Zaveri, R. A. (2010), 'Black carbon over mexico: the effect of atmospheric transport on mixing state, mass absorption cross-section, and bc/co ratios', *Atmospheric chemistry and physics* **10**(1), 219–237.

Sun, J., Birmili, W., Hermann, M., Tuch, T., Weinhold, K., Merkel, M., Rasch, F., Müller, T., Schladitz, A., Bastian, S., Löschau, G., Cyrys, J., Gu, J., Flentje, H., Briel, B., Asbach, C., Kaminski, H., Ries, L., Sohmer, R., Gerwig, H., Wirtz, K., Meinhardt, F., Schwerin, A., Bath, O., Ma, N. & Wiedensohler, A. (2020), 'Decreasing trends of particle number and black carbon mass concentrations at 16 observational sites in germany from 2009 to 2018', *Atmospheric Chemistry and Physics* **20**, 7049–7068.

Weinzierl, B., Gasteiger, J., Dollner, M., Schöberl, M., Seibert, P. & Philipp, A. (2020), 'A-care data acquisition report', *University of Vienna, University of Natural Resources and Life Sciences Vienna, EARTHCARE – A-CARE, ESA Contract No. 4000125810/18/NL/CT/gp, V1.0, 2020* **13**.

Zhang, R., Khalizov, A. F., Pagels, J., Zhang, D., Xue, H. & McMurry, P. H. (2008), 'Variability in morphology, hygroscopicity, and optical properties of soot aerosols during atmospheric processing', *PNAS* **105**(30), 10291–10296.

A. Acknowledgements

I would like to give my thanks to everyone who helped me in one way or another during the creation of my Master's thesis.

First of all, I would like to thank Bernadett Weinzierl, who supervised me, for the constructive feedback and stimulating new ideas throughout my work.

Special thanks to Katharina Heimerl for providing me with pre-processed SP2 data, always answering my questions regarding the measurement device and providing me with valuable feedback throughout. I would also like to thank Petra Seibert and Anne Phillips, for their work on FLEXPART. A big thank you to Anne, who always took the time to answer any questions of mine and helped me improve my programming skills greatly.

For providing sequence average data as well as constructive feedback throughout, I would like to thank Josef Gasteiger. Thank you, Josef, for taking the time to read through first drafts of this work and helping me improve my thesis. I would also like to thank Maximilian Dollner, not only for organising almost weakly A-LIFE update meetings but also for his comments to my work and providing me with new ideas for improving plots etc.

I would also like to thank my colleagues from the aerosol group and especially everyone participating in the A-LIFE project.

Last, but not least, I would like to thank my boyfriend Moritz as well as my family for their support and patience during the completion of this work.

A-LIFE is an ERC project at the University of Vienna with PI Bernadett Weinzierl. This project has received funding from the European Research Council (ERC) under the European Union's Horizon 2020 research and innovation program under grant agreement No. 640458. In addition, the German Aerospace Center (DLR) provided funding for a significant amount of flight hours and aircraft allocation days for the A-LIFE aircraft field experiment. Furthermore, two EUFAR projects were clustered with A-LIFE and provided funding for 16 flight hours. Moreover, various groups participated in the A-LIFE field experiment on their own funding.

B. Appendix

B.1. A-LIFE flight overview

Table B.1.: Overview of all flights, taken from A-LIFE webpage (2017).

#	Flight	Take-off [UTC]	Landing[UTC]	Objective
1	28.03.2017	09:00:47	11:57:18	Dust sampling over France and Germany; low approach at Dijon Airport
		Oberpfaff. (DE)	Oberpfaff. (DE)	(10:16:18 - 10:16:23 UTC, ∼230 m)
2	31.03.2017	07:35:42	10:43:59	Comparison of pollution levels over two major European cities (Munich,
		Oberpfaff. (DE)	Oberpfaff. (DE)	Vienna) in comparision with the tropospheric background site Mount Sonnblick GAW Observatory; low approach at Vienna International Airport (09:52:35 - 09:52:38 UTC, ∼250 m)
3	03.04.2017	06:08:30	09:01:59	Transfer flight, in-situ profiling over Mount Sonnblick GAW Observatory,
		Oberpfaff. (DE)	Cagliari (IT)	Genua and Sardinia (aged dust)
4	03.04.2017	12:38:03	15:49:47	Transfer flight, dust ahead of a low pressure system; in-situ profiling near
		Cagliari (IT)	Paphos (CY)	Crete
5	05.04.2017	08:50:01	12:08:09	Middle East/Arabian dust, cloud-free conditions; low approach at Paphos
		Paphos (CY)	Paphos (CY)	Airport (12:02:51 - 12:03:09 UTC, ∼50 m)
6	06.04.2017	04:30:27	08:05:57	Middle East/Arabian (low altitudes) & Saharan dust (higher altitudes),
		Paphos (CY)	Paphos (CY)	cloud-free conditions; low approach at Paphos Airport (08:01:10 - 08:01:35 UTC; ∼50m); Lagrangian match with flight 1?
7	11.04.2017	05:04:10	08:56:45	Dust in the Cyprus area before trough passage; „pattern cloud“; heavily
		Paphos (CY)	Paphos (CY)	polluted atmosphere at 2000ft over the sea south of Cyprus, low approach at Paphos Airport (08:49:53 - 08:50:02 UTC, ∼50m)
8	11.04.2017	09:56:35	12:59:01	Dust in the Cyprus area before trough passage; „pattern preferred“; low
		Paphos (CY)	Paphos (CY)	approach at Paphos Airport (12:55:06 - 12:55:26 UTC ∼50m)
9	13.04.2017	08:27:31	11:46:42	Dust embedded in clouds, ice formation at high temps; heavy pollution at
		Paphos (CY)	Paphos (CY)	low altitudes over the sea south of Cyprus; polluted dust down to the ground
10	14.04.2017	04:07:35	07:58:23	Dust and pollution sampling over Crete; lidar flight Cyprus - Crete; in-situ
		Paphos (CY)	Heraklion (GR)	profiling over Finokalia before landing; indications for vertical mixing inside the dust layer; dust gradient with dust surge east of Crete
11	14.04.2017	09:03:58	12:24:40	Dust and pollution sampling over Crete; in-situ & lidar flight with W-E
		Heraklion (GR)	Paphos (CY)	profiling Finokalia; dust gradient with dust surge east of Crete; low approach Pafos (12:20:17 - 12:20:44 UTC; ∼50m)
12	19.04.2017	09:58:52	13:56:52	Beginning of a Saharan dust outbreak which moved eastwards; lidar flight
		Paphos (CY)	Malta (MT)	Cyprus - Malta with vertical in-situ profiling in the Malta region
13	19.04.2017	15:10:26	19:06:37	Beginning of a Saharan dust outbreak which moved eastwards; in-situ
		Malta (MT)	Paphos (CY)	profiling after take-off in Malta; chasing of dust-impacted clouds near Malta
14	20.04.2017	10:06:17	13:34:59	Cyprus – Crete: maximum of the Saharan dust outbreak; coordinated
		Paphos (CY)	Heraklion (GR)	measurements with Crete; Lagrangian dust sampling of the airmass sampled the day before?
15	20.04.2017	14:40:23	18:33:30	Crete – Cyprus: maximum of the Saharan dust outbreak, chasing of dustimpacted
		Heraklion (GR)	Paphos (CY)	clouds near/over Crete in the cloud top layer; aerosol-cloud interaction
16	21.04.2017	11:48:30	16:01:13	Dust sampling west and south-west of Cyprus: end of Saharan dust outbreak;
		Paphos (CY)	Paphos (CY)	low approach at Paphos Airport (15:55:20 - 15:55:53 UTC, ∼50m); Lagrangian dust sampling of the airmasses detected the day before?
17	22.04.2017	06:07:01	09:26:15	Dust sampling south of Cyprus: end of Saharan dust outbreak;
		Paphos (CY)	Paphos (CY)	low approach at Paphos Airport (09:22:08 - 09:22:31 UTC, ∼50m)
18	25.04.2017	08:03:40	10:20:25	Sampling of pollution (and biomass burning?) from Turkey and the Black
		Paphos (CY)	Paphos (CY)	Sea west and north-west of Cyprus; low approach at Paphos Airport (10:15:16 - 10:15:37 UTC; ∼50m)
19	26.07.2017	12:06:05	14:39:49	Arabian and Sahran dust outbreak; Saharan dust mainly in the western
		Paphos (CY)	Paphos (CY)	part of the flight pattern, Arabian dust in the south-eastern part of the flight pattern
20	27.04.2017	07:13:15	10:18:11	Arabian and Sahran dust outbreak (same flight pattern as on the day before);
		Paphos (CY)	Paphos (CY)	probably boundary of Arabian dust between Paphos and Limassol during take-off; low approach at Paphos Airport (10:13:18 - 10:13:32 UTC; ∼50m)
21	29.04.2017	07:06:29	10:34:11	Transfer flight: Cyprus – Crete: Saharan dust outbreak, coordinated measurements
		Paphos (CY)	Heraklion (GR)	with Crete
22	29.04.2017	11:42:25	14:48:26	Crete - Oberpfaffenhofen; flight on the back side of a low pressure system
		Heraklion (GR)	Oberpfaff. (DE)	

B.2. A-LIFE BC data overview

Table B.2.: Overview of measured and modelled data used in this thesis.

Instrumentation / model	**Measured / simulated quantity**	**Size range**	**Serial number / version**
Single Particle Soot Photometer (SP2)	Refractory black carbon (rBC) mass concentration, coated fraction	mass in range 5 - 104 fg, corresponding to an equivalent size range of 70 - 990 nm	SN: 0710-009 (without computer) SN: 0903-013 (with computer)
FLEXPART	Black carbon (BC) mass concentration	Accumulation mode (∼0.01 - 1 μm)	version 8.2

B.3. Vertical profiles

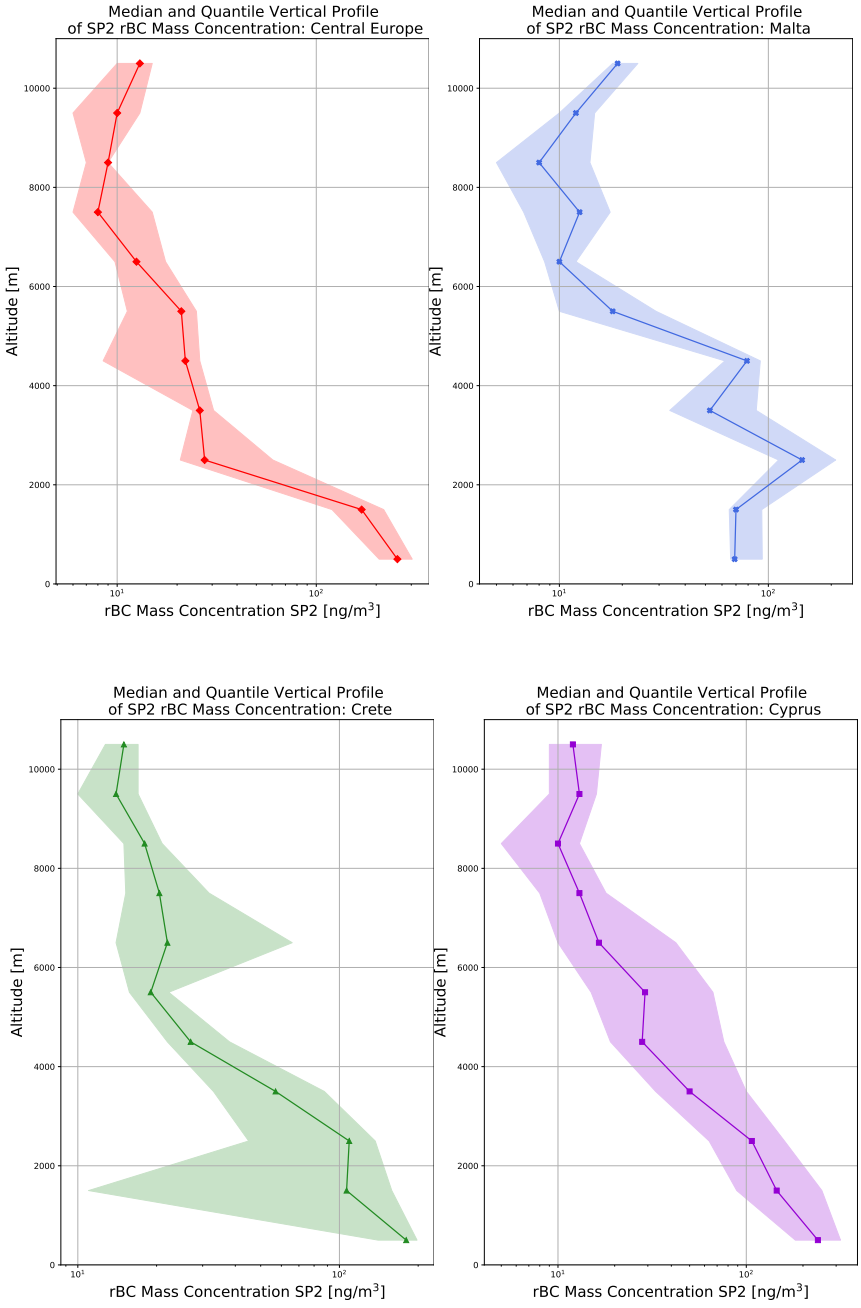

Figure B.2.: Median vertical profiles of rBC mass concentrations including first and third quantile as shaded areas for the individual flight regions (Europe: red, Malta: blue, Crete: green, Cyprus: purple).

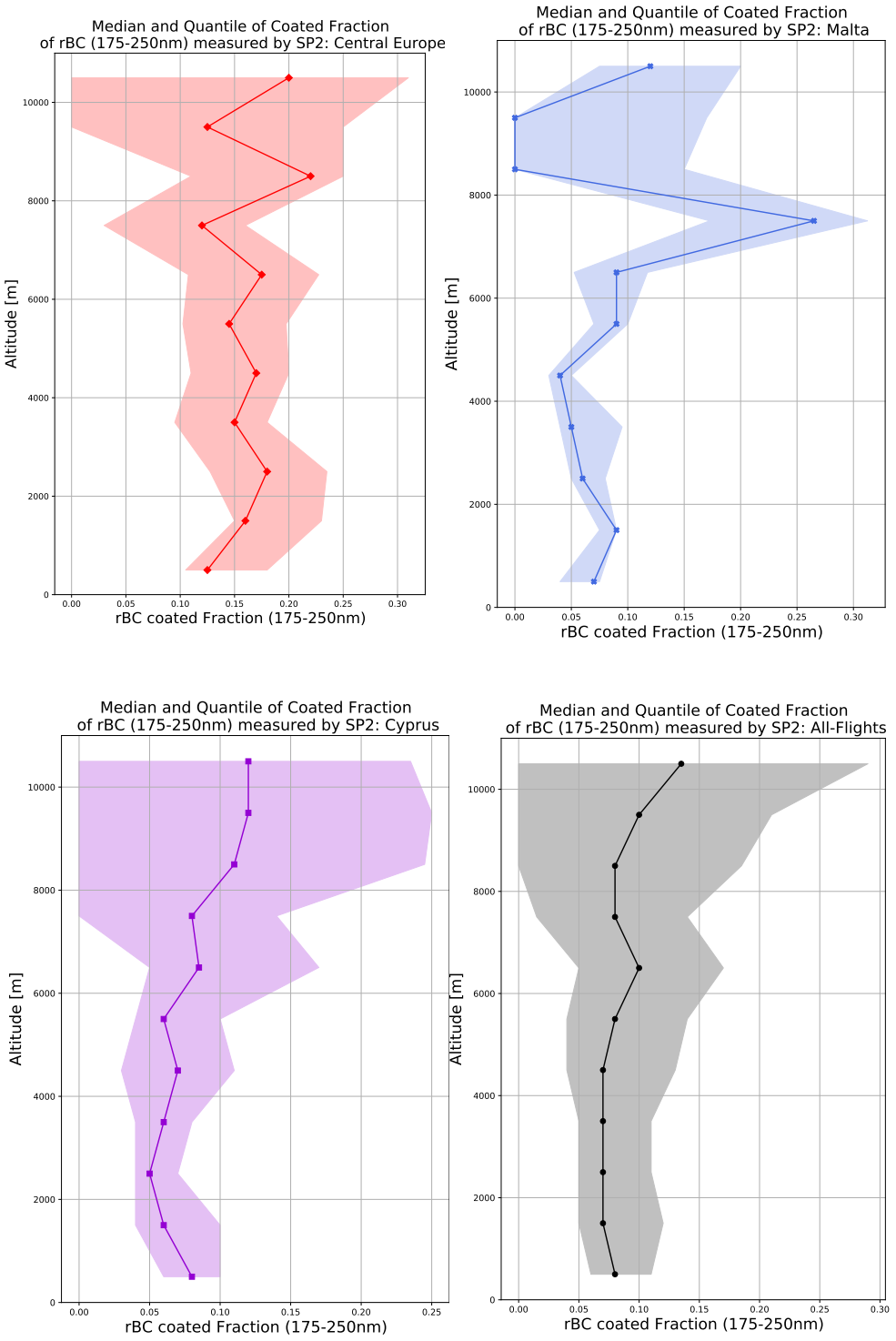

Figure B.4.: Median vertical profiles of rBC coated fraction including first and third quantile as shaded areas for the individual flight regions (Europe: red, Malta: blue, Cyprus: purple) and all flights (black) .

B.4. Time series of measured and modelled BC mass concentrations for individual flights

Time series of all flights including altitude (black solid line), SP2 rBC mass concentration (black triangles), cloud sequences (blue squares) and FLEXPART BC concentration for all source regions.

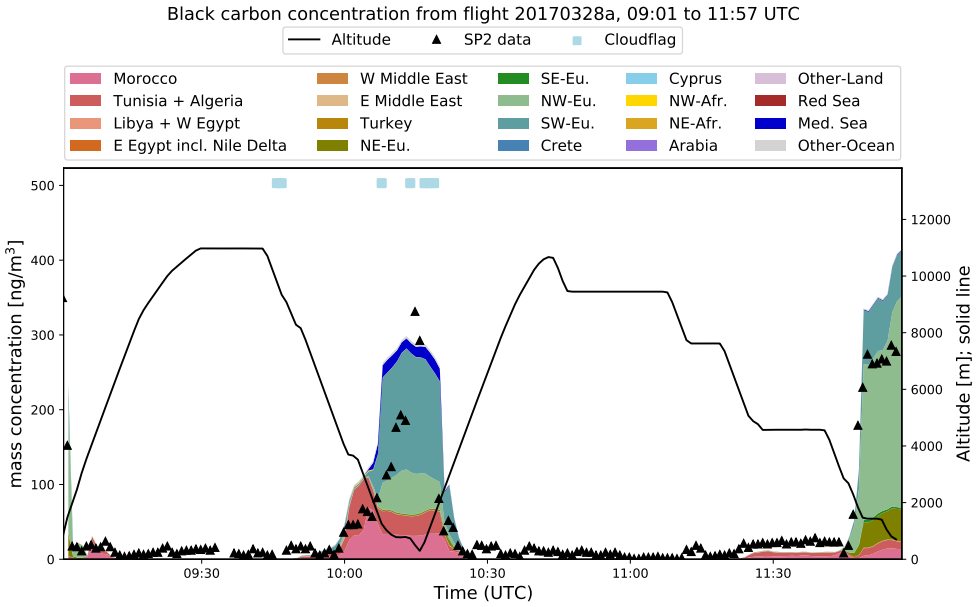
Black carbon concentration from flight 20170328a, 09:01 to 11:57 UTC
Altitude
SP2 data
Cloudflag
Morocco
Tunisia + Algeria
Libya + W Egypt
E Egypt incl. Nile Delta
W Middle East
E Middle East
Turkey
NE-Eu.
SE-Eu.
NW-Eu.
SW-Eu.
Crete
Cyprus
NW-Afr.
NE-Afr.
Arabia
Other-Land
Red Sea
Med. Sea
Other-Ocean
mass concentration [ng/m^3]
Altitude [m]; solid line
Time (UTC)

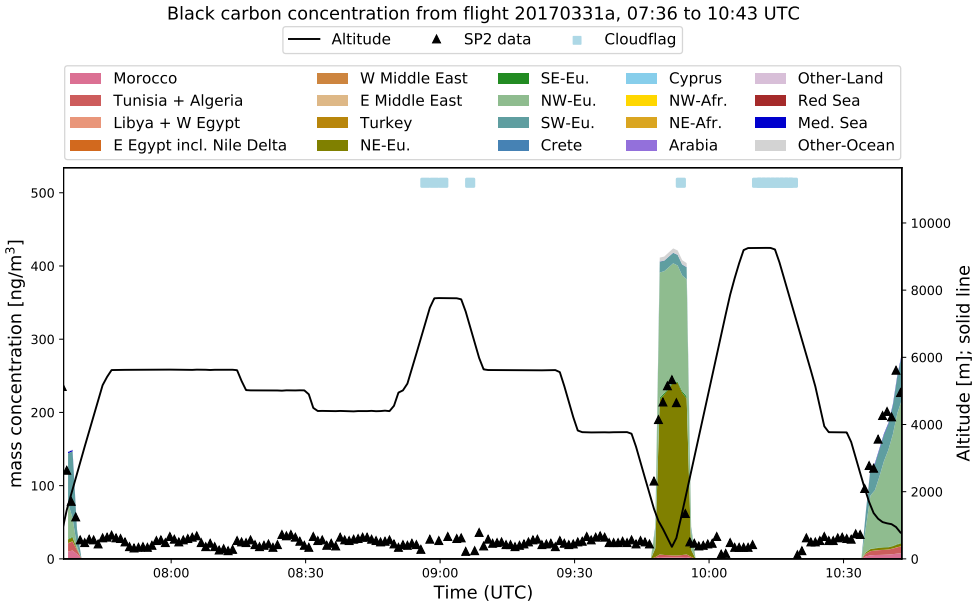
Black carbon concentration from flight 20170331a, 07:36 to 10:43 UTC
Altitude
SP2 data
Cloudflag
Morocco
Tunisia + Algeria
Libya + W Egypt
E Egypt incl. Nile Delta
W Middle East
E Middle East
Turkey
NE-Eu.
SE-Eu.
NW-Eu.
SW-Eu.
Crete
Cyprus
NW-Afr.
NE-Afr.
Arabia
Other-Land
Red Sea
Med. Sea
Other-Ocean
mass concentration [ng/m^3]
Altitude [m]; solid line
Time (UTC)

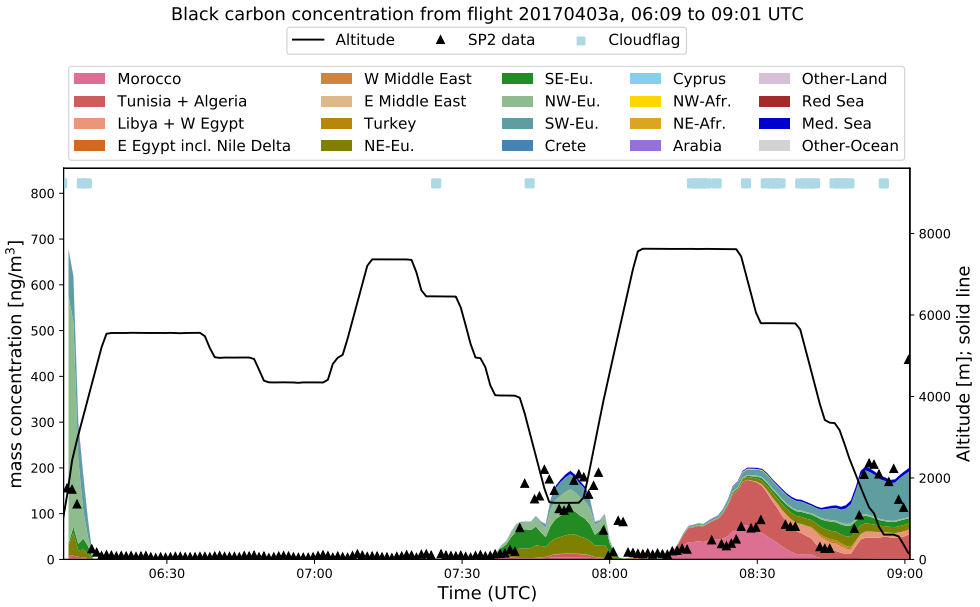
Black carbon concentration from flight 20170403a, 06:09 to 09:01 UTC
Altitude
SP2 data
Cloudflag
Morocco
Tunisia + Algeria
Libya + W Egypt
E Egypt incl. Nile Delta
W Middle East
E Middle East
Turkey
NE-Eu.
SE-Eu.
NW-Eu.
SW-Eu.
Crete
Cyprus
NW-Afr.
NE-Afr.
Arabia
Other-Land
Red Sea
Med. Sea
Other-Ocean
mass concentration [ng/m^3]
Altitude [m]; solid line
Time (UTC)

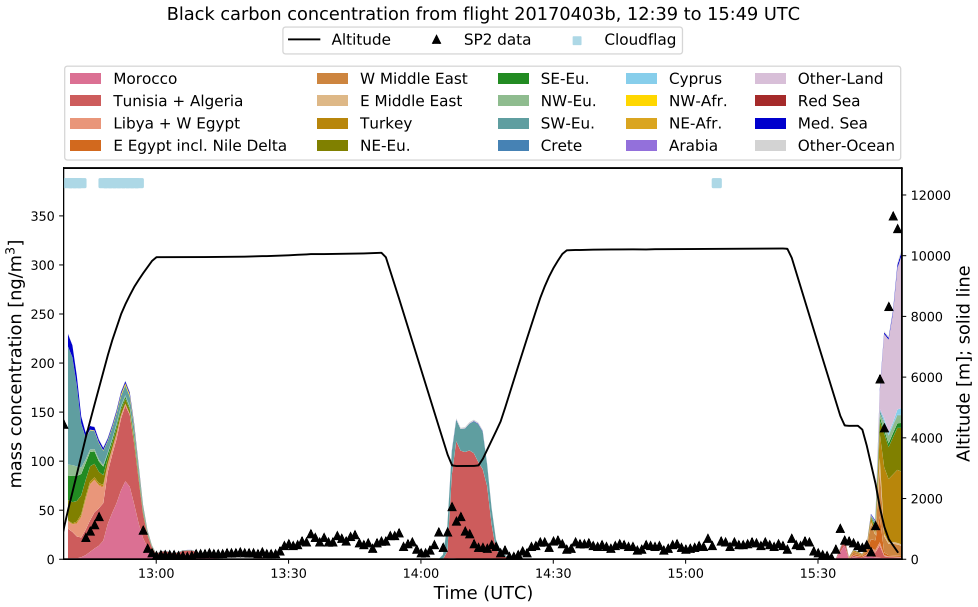
Black carbon concentration from flight 20170403b, 12:39 to 15:49 UTC
Altitude
SP2 data
Cloudflag
Morocco
Tunisia + Algeria
Libya + W Egypt
E Egypt incl. Nile Delta
W Middle East
E Middle East
Turkey
NE-Eu.
SE-Eu.
NW-Eu.
SW-Eu.
Crete
Cyprus
NW-Afr.
NE-Afr.
Arabia
Other-Land
Red Sea
Med. Sea
Other-Ocean
mass concentration [ng/m^3]
Altitude [m]; solid line
Time (UTC)

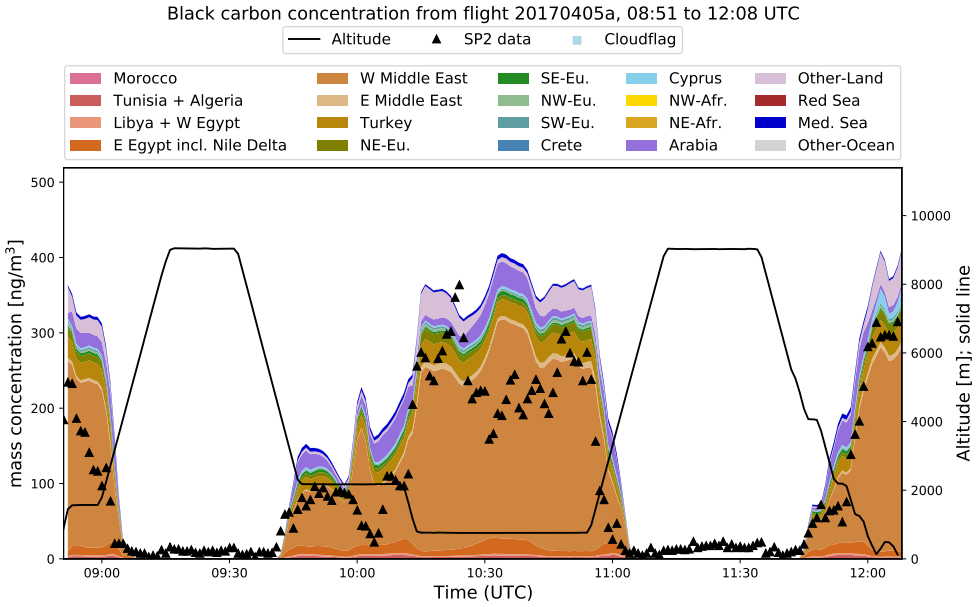
Black carbon concentration from flight 20170405a, 08:51 to 12:08 UTC
Altitude
SP2 data
Cloudflag
Morocco
Tunisia + Algeria
Libya + W Egypt
E Egypt incl. Nile Delta
W Middle East
E Middle East
Turkey
NE-Eu.
SE-Eu.
NW-Eu.
SW-Eu.
Crete
Cyprus
NW-Afr.
NE-Afr.
Arabia
Other-Land
Red Sea
Med. Sea
Other-Ocean
mass concentration [ng/m^3]
Altitude [m]; solid line
Time (UTC)

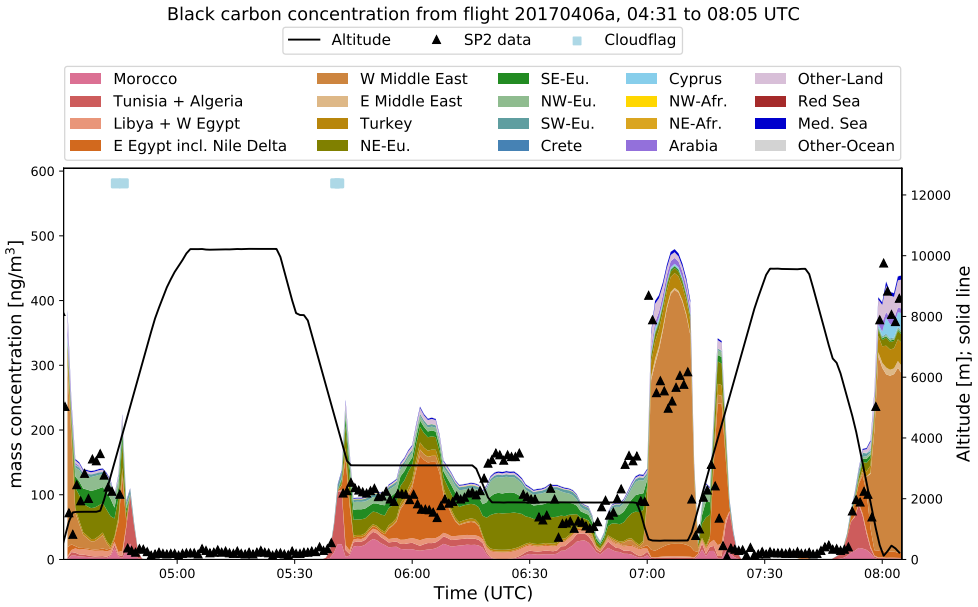
Black carbon concentration from flight 20170406a, 04:31 to 08:05 UTC
Altitude
SP2 data
Cloudflag
Morocco
Tunisia + Algeria
Libya + W Egypt
E Egypt incl. Nile Delta
W Middle East
E Middle East
Turkey
NE-Eu.
SE-Eu.
NW-Eu.
SW-Eu.
Crete
Cyprus
NW-Afr.
NE-Afr.
Arabia
Other-Land
Red Sea
Med. Sea
Other-Ocean
mass concentration [ng/m^3]
Altitude [m]; solid line
Time (UTC)

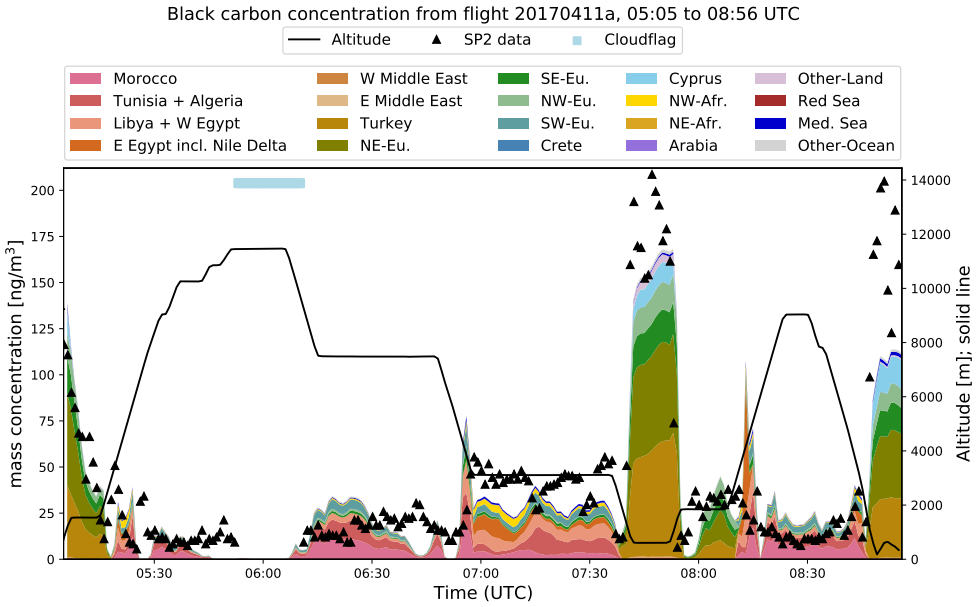
Black carbon concentration from flight 20170411a, 05:05 to 08:56 UTC
Altitude
SP2 data
Cloudflag
Morocco
Tunisia + Algeria
Libya + W Egypt
E Egypt incl. Nile Delta
W Middle East
E Middle East
Turkey
NE-Eu.
SE-Eu.
NW-Eu.
SW-Eu.
Crete
Cyprus
NW-Afr.
NE-Afr.
Arabia
Other-Land
Red Sea
Med. Sea
Other-Ocean
mass concentration [ng/m^3]
Altitude [m]; solid line
Time (UTC)

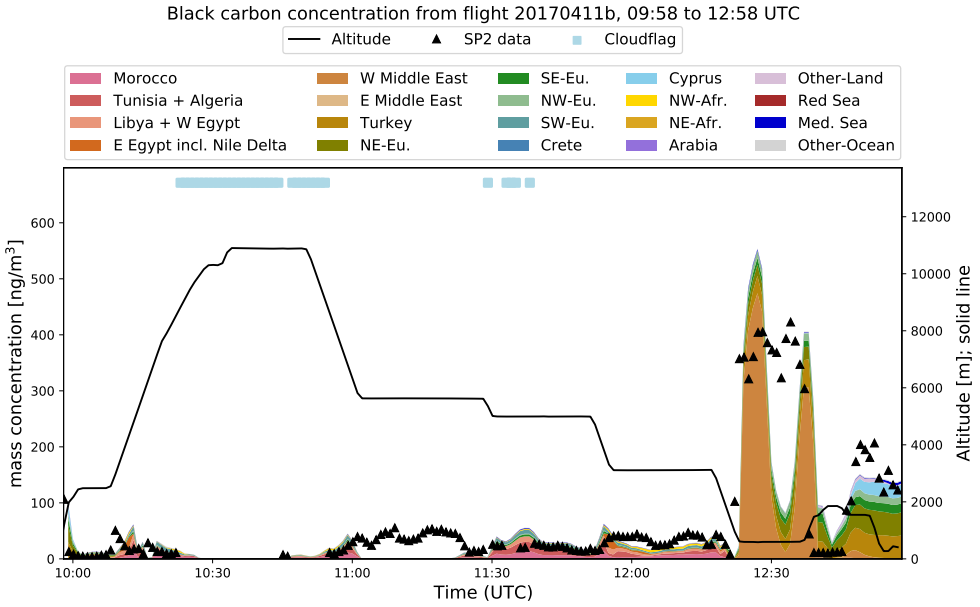
Black carbon concentration from flight 20170411b, 09:58 to 12:58 UTC
Altitude
SP2 data
Cloudflag
Morocco
Tunisia + Algeria
Libya + W Egypt
E Egypt incl. Nile Delta
W Middle East
E Middle East
Turkey
NE-Eu.
SE-Eu.
NW-Eu.
SW-Eu.
Crete
Cyprus
NW-Afr.
NE-Afr.
Arabia
Other-Land
Red Sea
Med. Sea
Other-Ocean
mass concentration [ng/m^3]
Altitude [m]; solid line
Time (UTC)

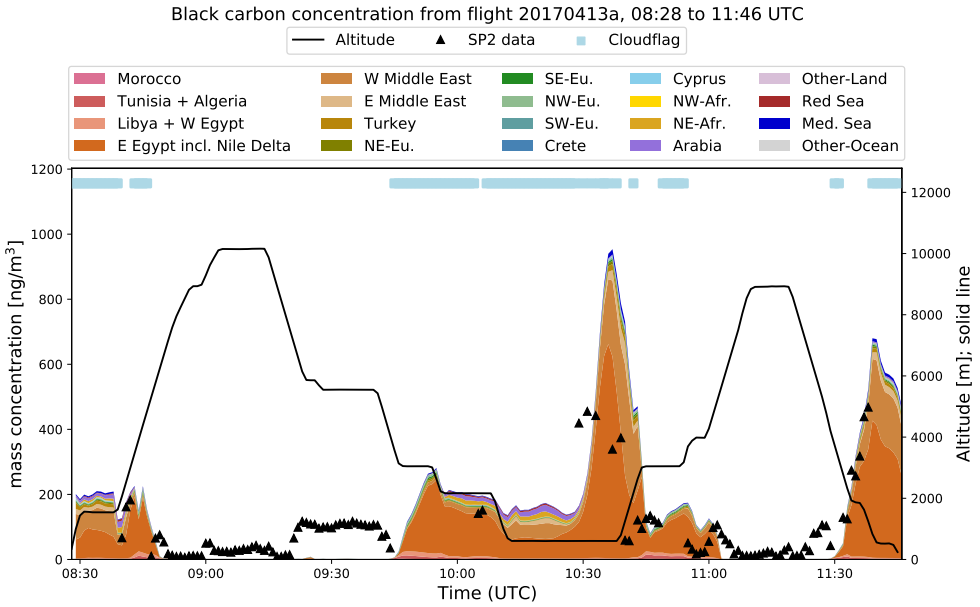
Black carbon concentration from flight 20170413a, 08:28 to 11:46 UTC
Altitude
SP2 data
Cloudflag
Morocco
Tunisia + Algeria
Libya + W Egypt
E Egypt incl. Nile Delta
W Middle East
E Middle East
Turkey
NE-Eu.
SE-Eu.
NW-Eu.
SW-Eu.
Crete
Cyprus
NW-Afr.
NE-Afr.
Arabia
Other-Land
Red Sea
Med. Sea
Other-Ocean
mass concentration [ng/m^3]
Altitude [m]; solid line
Time (UTC)

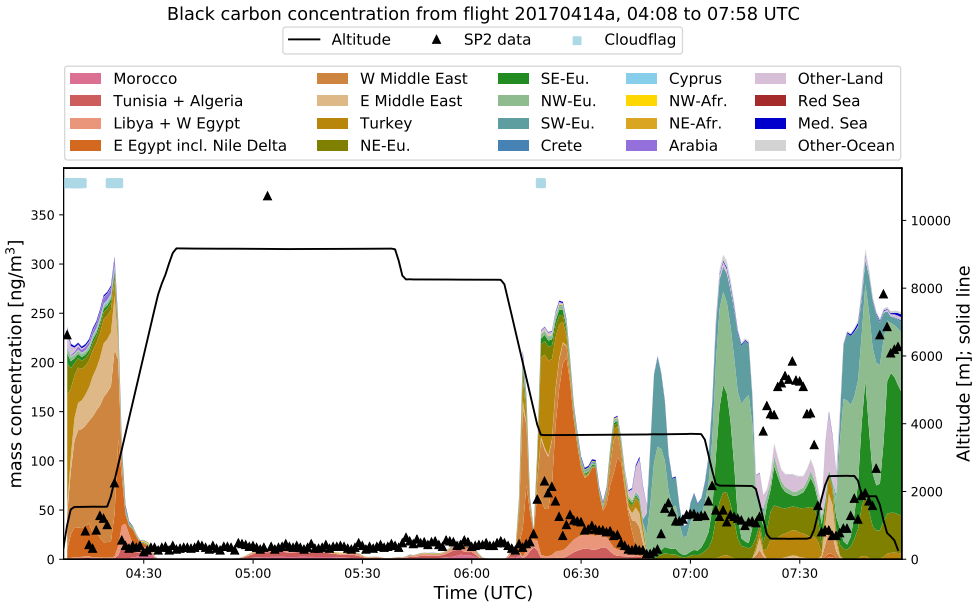
Black carbon concentration from flight 20170414a, 04:08 to 07:58 UTC
Altitude
SP2 data
Cloudflag
Morocco
Tunisia + Algeria
Libya + W Egypt
E Egypt incl. Nile Delta
W Middle East
E Middle East
Turkey
NE-Eu.
SE-Eu.
NW-Eu.
SW-Eu.
Crete
Cyprus
NW-Afr.
NE-Afr.
Arabia
Other-Land
Red Sea
Med. Sea
Other-Ocean
mass concentration [ng/m^3]
Altitude [m]; solid line
Time (UTC)

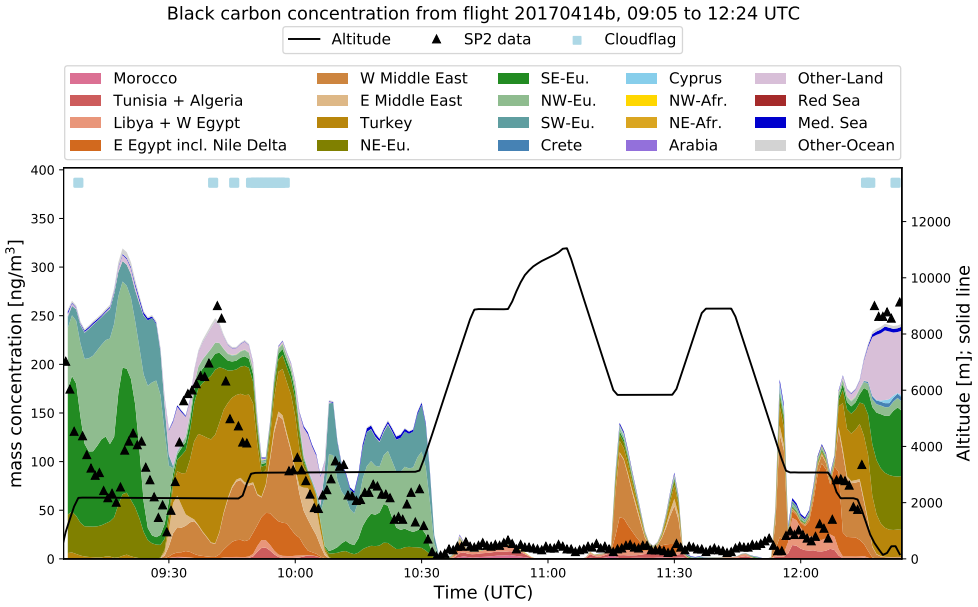
Black carbon concentration from flight 20170414b, 09:05 to 12:24 UTC
Altitude
SP2 data
Cloudflag
Morocco
Tunisia + Algeria
Libya + W Egypt
E Egypt incl. Nile Delta
W Middle East
E Middle East
Turkey
NE-Eu.
SE-Eu.
NW-Eu.
SW-Eu.
Crete
Cyprus
NW-Afr.
NE-Afr.
Arabia
Other-Land
Red Sea
Med. Sea
Other-Ocean
mass concentration [ng/m^3]
Altitude [m]; solid line
Time (UTC)

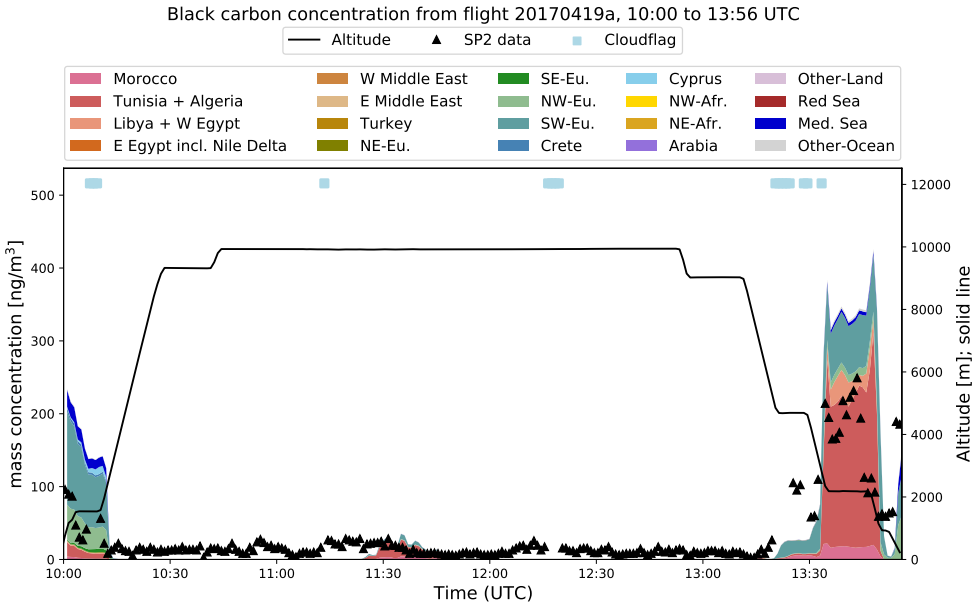
Black carbon concentration from flight 20170419a, 10:00 to 13:56 UTC
Altitude
SP2 data
Cloudflag
Morocco
Tunisia + Algeria
Libya + W Egypt
E Egypt incl. Nile Delta
W Middle East
E Middle East
Turkey
NE-Eu.
SE-Eu.
NW-Eu.
SW-Eu.
Crete
Cyprus
NW-Afr.
NE-Afr.
Arabia
Other-Land
Red Sea
Med. Sea
Other-Ocean
mass concentration [ng/m^3]
Altitude [m]; solid line
Time (UTC)

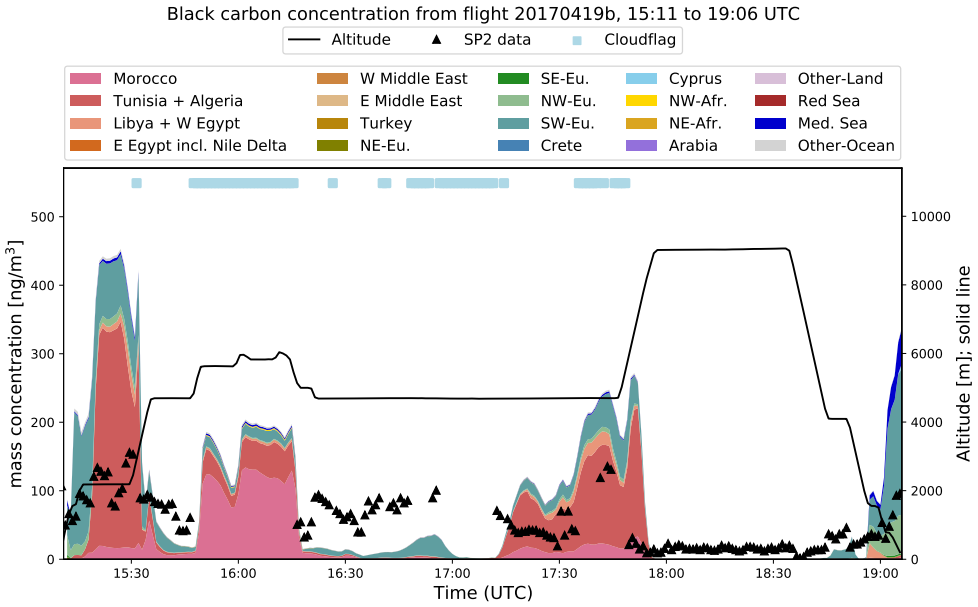
Black carbon concentration from flight 20170419b, 15:11 to 19:06 UTC
Altitude
SP2 data
Cloudflag
Morocco
Tunisia + Algeria
Libya + W Egypt
E Egypt incl. Nile Delta
W Middle East
E Middle East
Turkey
NE-Eu.
SE-Eu.
NW-Eu.
SW-Eu.
Crete
Cyprus
NW-Afr.
NE-Afr.
Arabia
Other-Land
Red Sea
Med. Sea
Other-Ocean
mass concentration [ng/m^3]
Altitude [m]; solid line
Time (UTC)

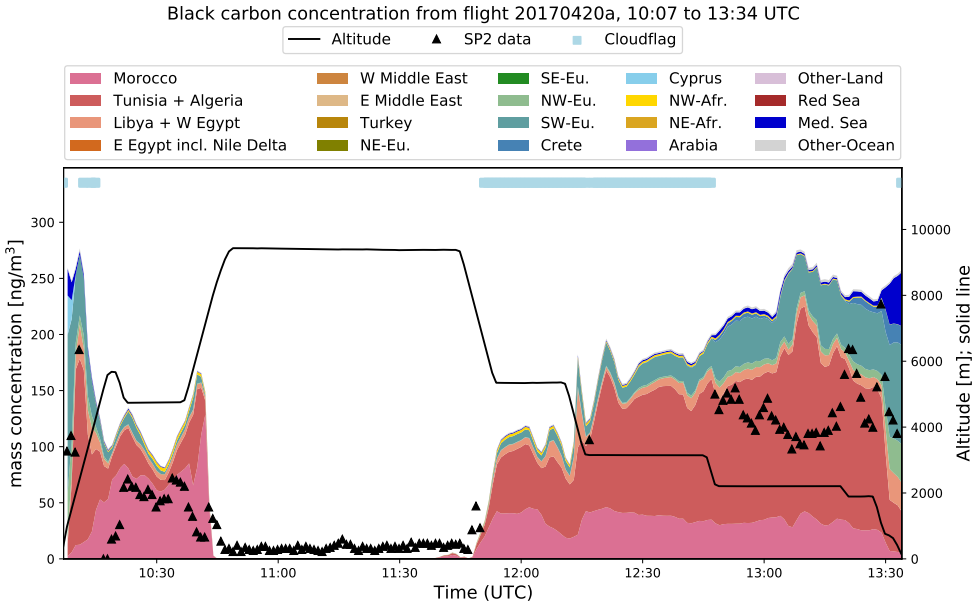
Black carbon concentration from flight 20170420a, 10:07 to 13:34 UTC
Altitude
SP2 data
Cloudflag
Morocco
Tunisia + Algeria
Libya + W Egypt
E Egypt incl. Nile Delta
W Middle East
E Middle East
Turkey
NE-Eu.
SE-Eu.
NW-Eu.
SW-Eu.
Crete
Cyprus
NW-Afr.
NE-Afr.
Arabia
Other-Land
Red Sea
Med. Sea
Other-Ocean
mass concentration [ng/m^3]
Altitude [m]; solid line
Time (UTC)

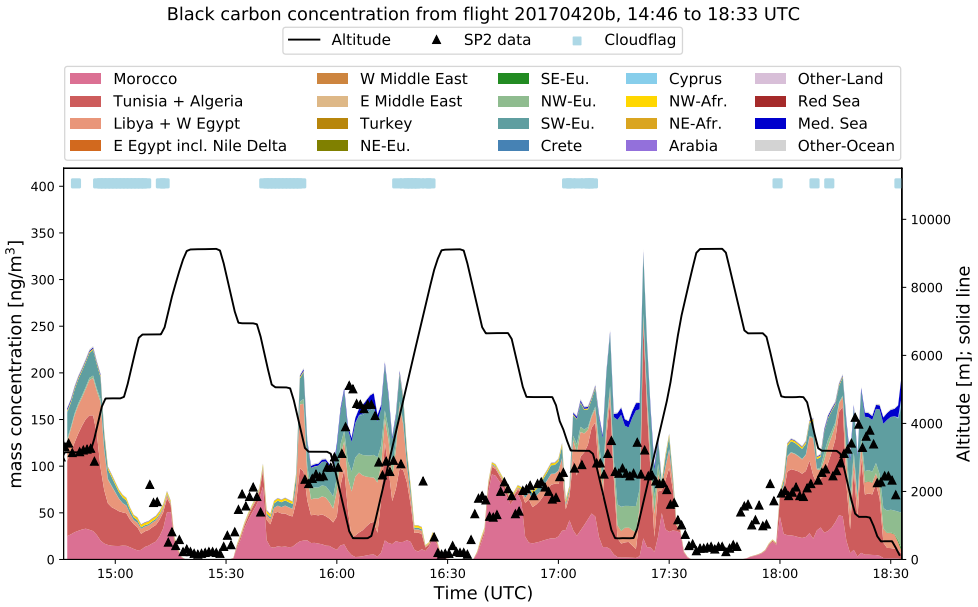
Black carbon concentration from flight 20170420b, 14:46 to 18:33 UTC
Altitude
SP2 data
Cloudflag
Morocco
Tunisia + Algeria
Libya + W Egypt
E Egypt incl. Nile Delta
W Middle East
E Middle East
Turkey
NE-Eu.
SE-Eu.
NW-Eu.
SW-Eu.
Crete
Cyprus
NW-Afr.
NE-Afr.
Arabia
Other-Land
Red Sea
Med. Sea
Other-Ocean
mass concentration [ng/m^3]
Altitude [m]; solid line
Time (UTC)

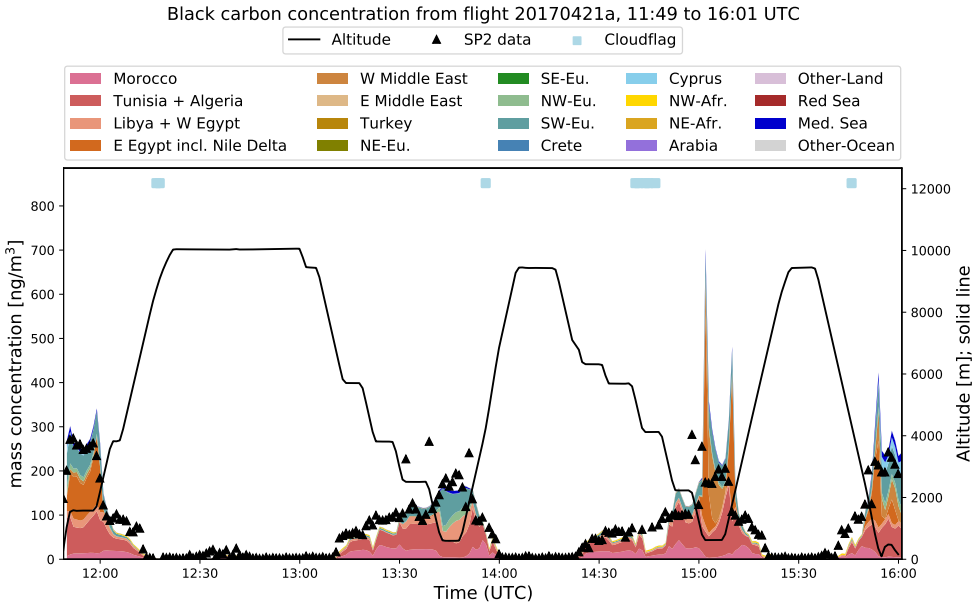
Black carbon concentration from flight 20170421a, 11:49 to 16:01 UTC
Altitude
SP2 data
Cloudflag
Morocco
Tunisia + Algeria
Libya + W Egypt
E Egypt incl. Nile Delta
W Middle East
E Middle East
Turkey
NE-Eu.
SE-Eu.
NW-Eu.
SW-Eu.
Crete
Cyprus
NW-Afr.
NE-Afr.
Arabia
Other-Land
Red Sea
Med. Sea
Other-Ocean
mass concentration [ng/m³]
Altitude [m]; solid line
Time (UTC)

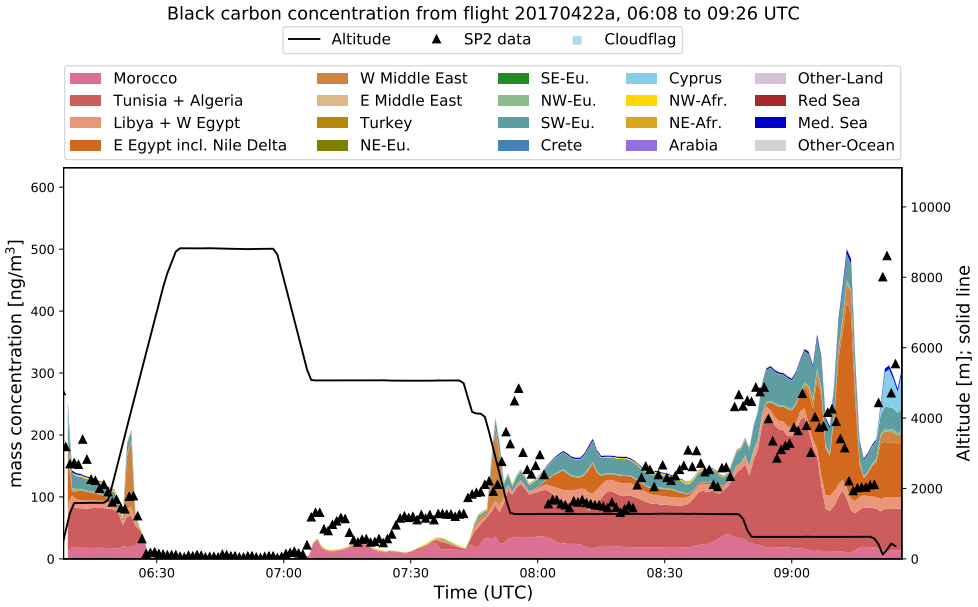
Black carbon concentration from flight 20170422a, 06:08 to 09:26 UTC
Altitude
SP2 data
Cloudflag
Morocco
Tunisia + Algeria
Libya + W Egypt
E Egypt incl. Nile Delta
W Middle East
E Middle East
Turkey
NE-Eu.
SE-Eu.
NW-Eu.
SW-Eu.
Crete
Cyprus
NW-Afr.
NE-Afr.
Arabia
Other-Land
Red Sea
Med. Sea
Other-Ocean
mass concentration [ng/m³]
Altitude [m]; solid line
Time (UTC)

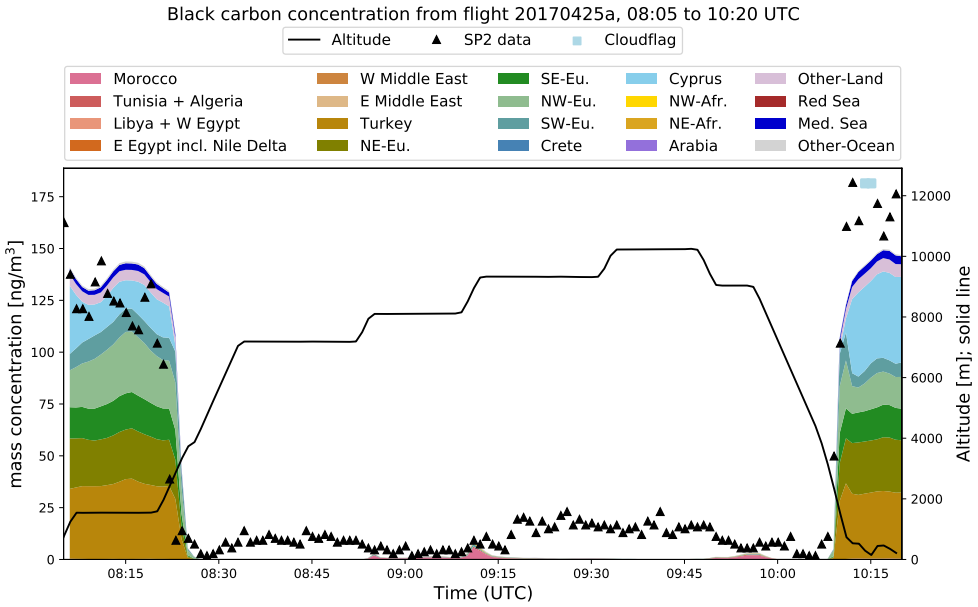
Black carbon concentration from flight 20170425a, 08:05 to 10:20 UTC
Altitude
SP2 data
Cloudflag
Morocco
Tunisia + Algeria
Libya + W Egypt
E Egypt incl. Nile Delta
W Middle East
E Middle East
Turkey
NE-Eu.
SE-Eu.
NW-Eu.
SW-Eu.
Crete
Cyprus
NW-Afr.
NE-Afr.
Arabia
Other-Land
Red Sea
Med. Sea
Other-Ocean
mass concentration [ng/m³]
Altitude [m]; solid line
Time (UTC)

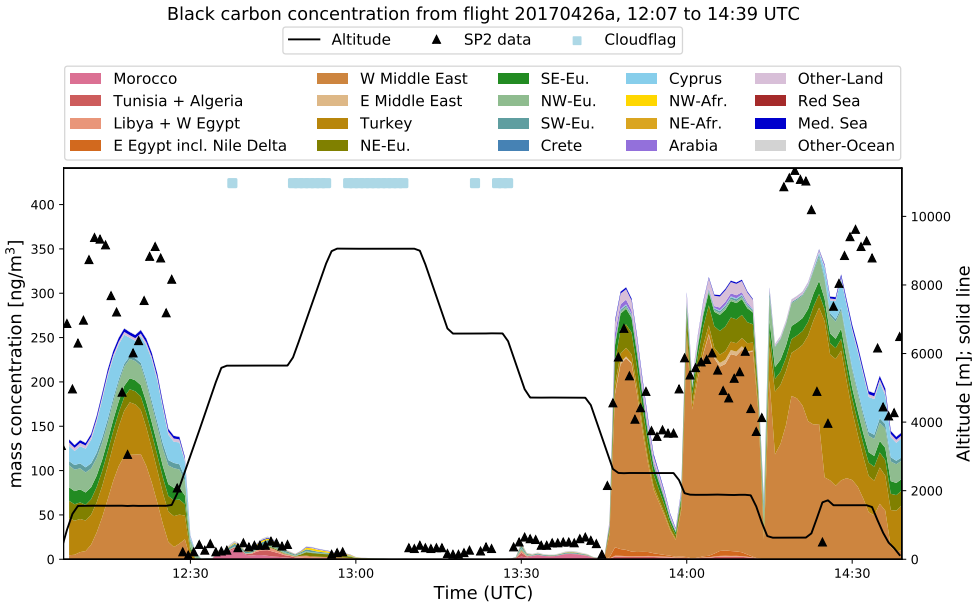
Black carbon concentration from flight 20170426a, 12:07 to 14:39 UTC
Altitude
SP2 data
Cloudflag
Morocco
Tunisia + Algeria
Libya + W Egypt
E Egypt incl. Nile Delta
W Middle East
E Middle East
Turkey
NE-Eu.
SE-Eu.
NW-Eu.
SW-Eu.
Crete
Cyprus
NW-Afr.
NE-Afr.
Arabia
Other-Land
Red Sea
Med. Sea
Other-Ocean
mass concentration [ng/m^3]
Altitude [m]; solid line
Time (UTC)

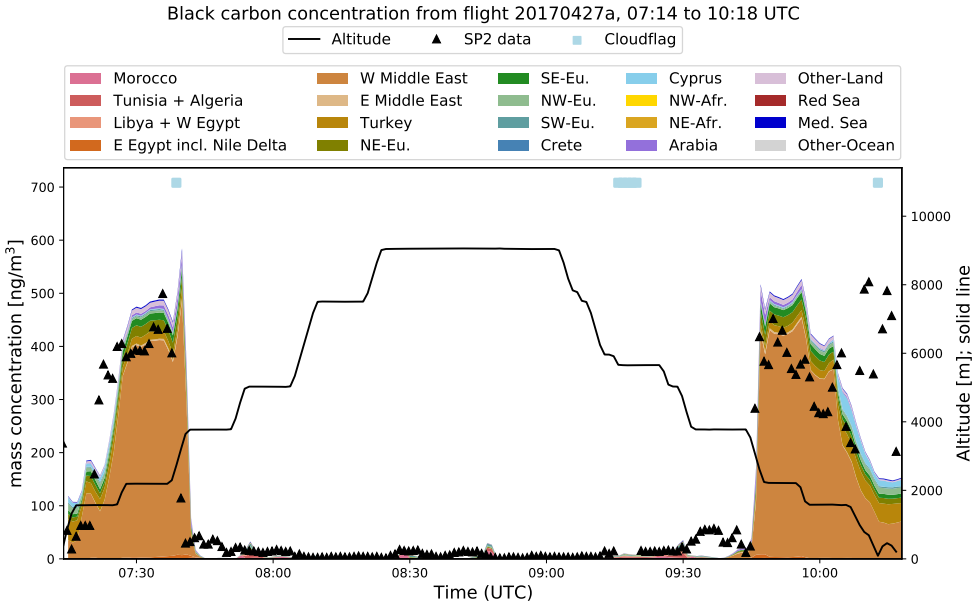
Black carbon concentration from flight 20170427a, 07:14 to 10:18 UTC
Altitude
SP2 data
Cloudflag
Morocco
Tunisia + Algeria
Libya + W Egypt
E Egypt incl. Nile Delta
W Middle East
E Middle East
Turkey
NE-Eu.
SE-Eu.
NW-Eu.
SW-Eu.
Crete
Cyprus
NW-Afr.
NE-Afr.
Arabia
Other-Land
Red Sea
Med. Sea
Other-Ocean
mass concentration [ng/m^3]
Altitude [m]; solid line
Time (UTC)

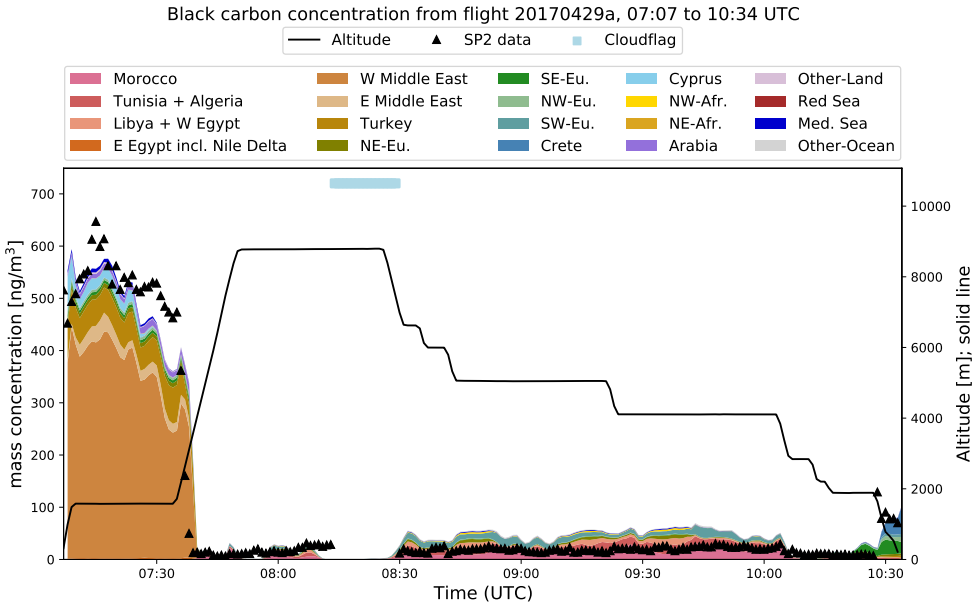
Black carbon concentration from flight 20170429a, 07:07 to 10:34 UTC
Altitude
SP2 data
Cloudflag
Morocco
Tunisia + Algeria
Libya + W Egypt
E Egypt incl. Nile Delta
W Middle East
E Middle East
Turkey
NE-Eu.
SE-Eu.
NW-Eu.
SW-Eu.
Crete
Cyprus
NW-Afr.
NE-Afr.
Arabia
Other-Land
Red Sea
Med. Sea
Other-Ocean
mass concentration [ng/m^3]
Altitude [m]; solid line
Time (UTC)

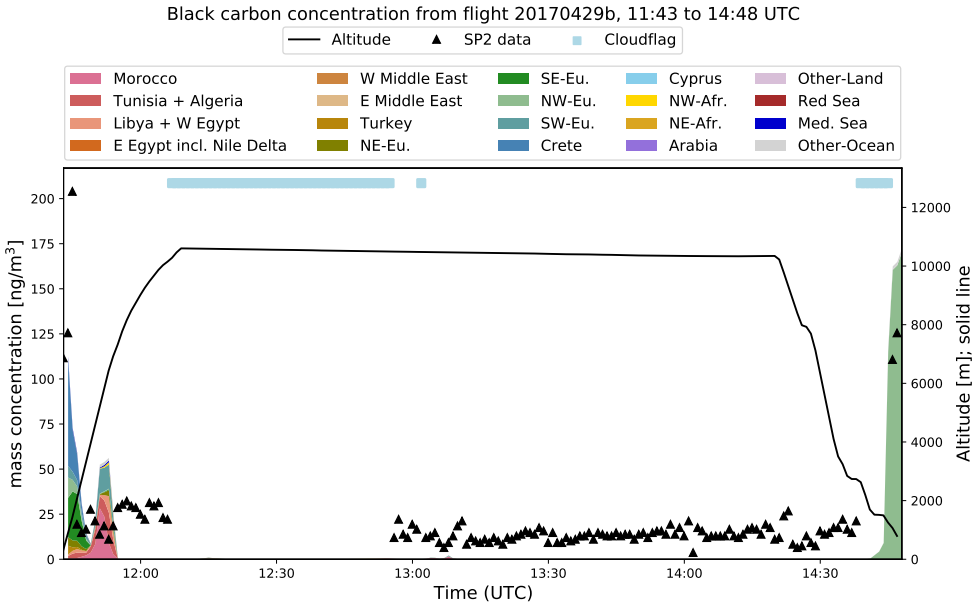

B.5. FLEXPART modelled BC source region histograms

Histograms of all FLEXPART BC source region mass concentrations including statistical parameters.

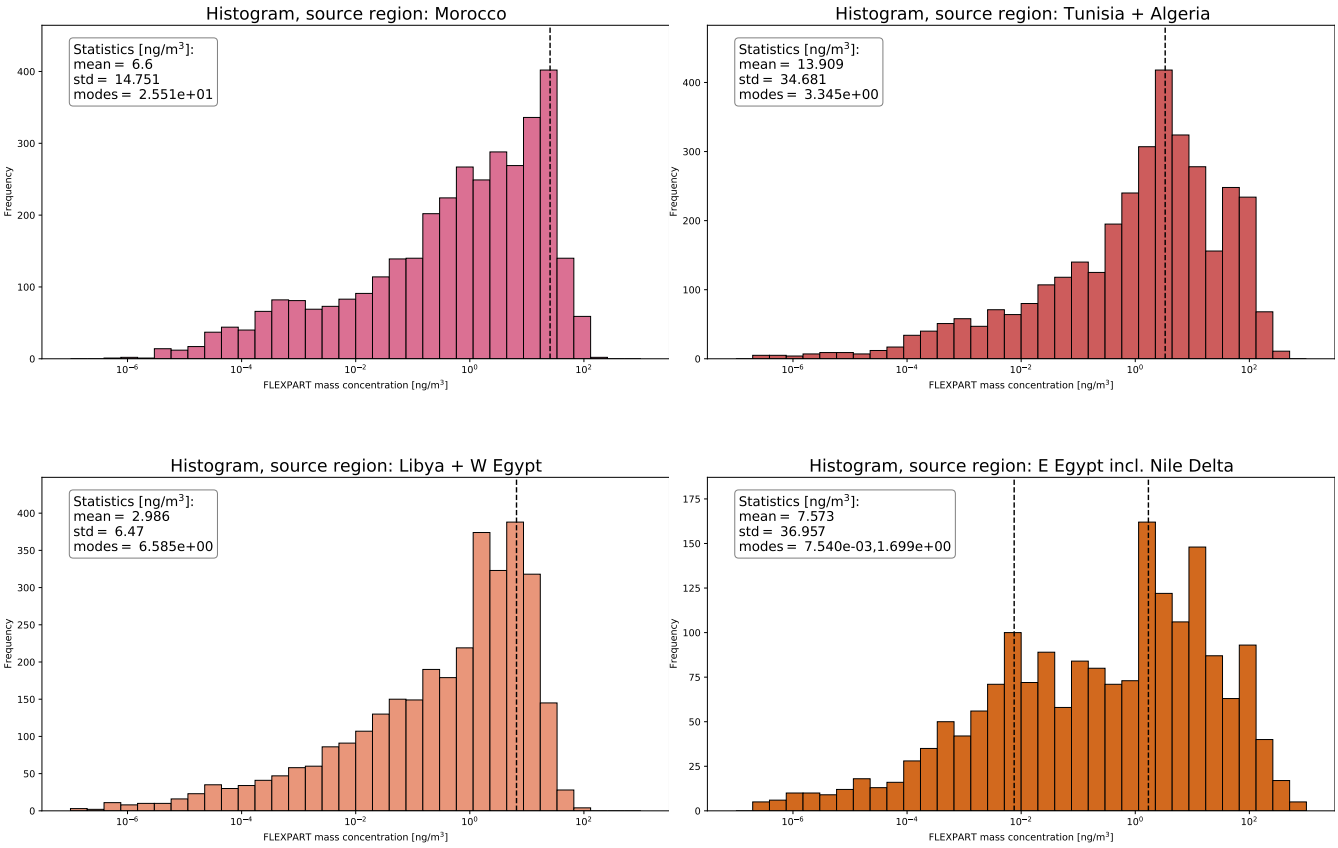

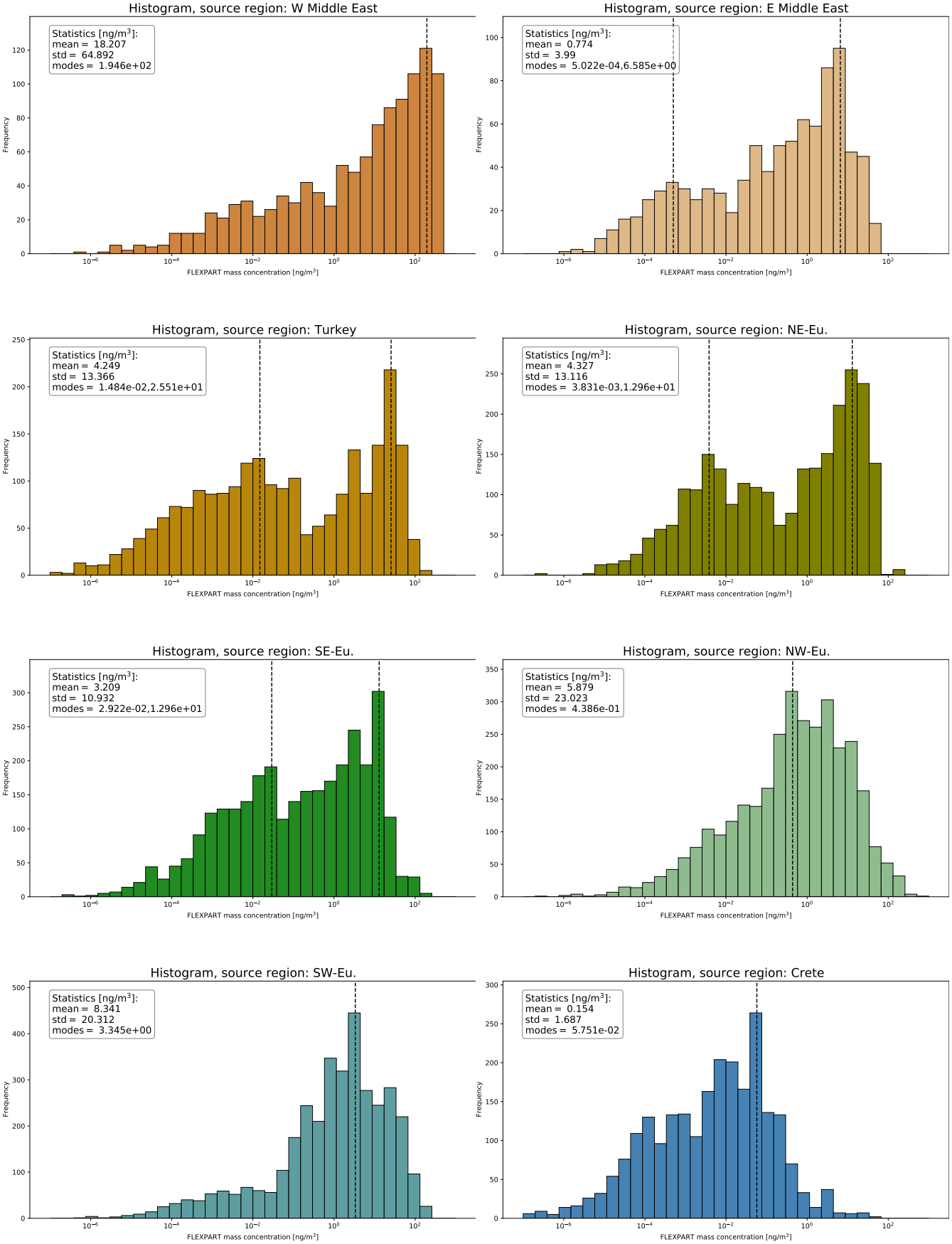
Histogram, source region: W Middle East
Statistics [ng/m³]:
mean = 18.207
std = 64.892
modes = 1.946e+02
Histogram, source region: E Middle East
Statistics [ng/m³]:
mean = 0.774
std = 3.99
modes = 5.022e-04,6.585e+00
Histogram, source region: Turkey
Statistics [ng/m³]:
mean = 4.249
std = 13.366
modes = 1.484e-02,2.551e+01
Histogram, source region: NE-Eu.
Statistics [ng/m³]:
mean = 4.327
std = 13.116
modes = 3.831e-03,1.296e+01
Histogram, source region: SE-Eu.
Statistics [ng/m³]:
mean = 3.209
std = 10.932
modes = 2.922e-02,1.296e+01
Histogram, source region: NW-Eu.
Statistics [ng/m³]:
mean = 5.879
std = 23.023
modes = 4.386e-01
Histogram, source region: SW-Eu.
Statistics [ng/m³]:
mean = 8.341
std = 20.312
modes = 3.345e+00
Histogram, source region: Crete
Statistics [ng/m³]:
mean = 0.154
std = 1.687
modes = 5.751e-02
Frequency
FLEXPART mass concentration [ng/m³]

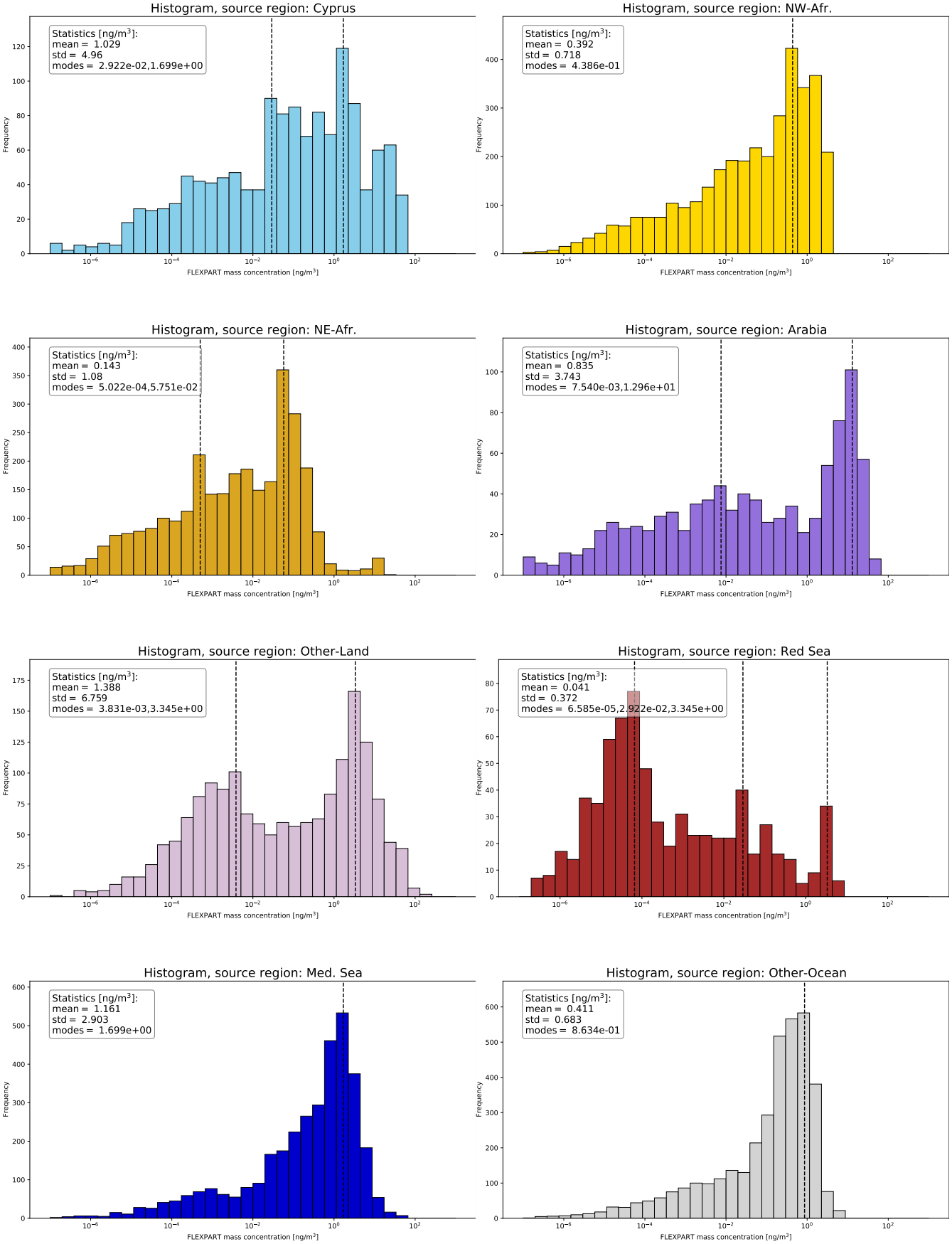
Histogram, source region: Cyprus
Statistics [ng/m³]:
mean = 1.029
std = 4.96
modes = 2.922e-02,1.699e+00
Histogram, source region: NW-Afr.
Statistics [ng/m³]:
mean = 0.392
std = 0.718
modes = 4.386e-01
Histogram, source region: NE-Afr.
Statistics [ng/m³]:
mean = 0.143
std = 1.08
modes = 5.022e-04,5.751e-02
Histogram, source region: Arabia
Statistics [ng/m³]:
mean = 0.835
std = 3.743
modes = 7.540e-03,1.296e+01
Histogram, source region: Other-Land
Statistics [ng/m³]:
mean = 1.388
std = 6.759
modes = 3.831e-03,3.345e+00
Histogram, source region: Red Sea
Statistics [ng/m³]:
mean = 0.041
std = 0.372
modes = 6.585e-05,2.922e-02,3.345e+00
Histogram, source region: Med. Sea
Statistics [ng/m³]:
mean = 1.161
std = 2.903
modes = 1.699e+00
Histogram, source region: Other-Ocean
Statistics [ng/m³]:
mean = 0.411
std = 0.683
modes = 8.634e-01
Frequency
FLEXPART mass concentration [ng/m³]